# Wireless Power Transmission Topology using Capacitively Coupled Open-Ended Helical Resonators

by

Fabiano Cezar Domingos

A thesis submitted in partial fulfillment of the requirements for the degree of

Master of Science

in

Electromagnetics and Microwaves

Department of Electrical and Computer Engineering

University of Alberta

# Abstract

Wireless power transfer (WPT) is an innovative technology seeking to revolutionize how electronic devices are employed by addressing restrictions caused by wired connections and limited battery autonomy. Although the fundamentals of WPT have been known for more than a century, the recent application in wireless charging of mobile phones has been the first widespread utilization of these systems. This fact supports further research efforts to foster the development of novel, robust, and efficient WPT methods.

This thesis investigates the design of resonant WPT systems using electromagnetic field coupling in the reactive near-field region.

The first part of this thesis comprises the study of inductive and capacitive WPT topologies based on circuit analysis. Three parameters are used to evaluate each configuration: power transmission capability, frequency of maximum power transfer, and robustness to increased distances between transmitter and receiver devices.

Then, the theory of open-ended helical resonators (OEHR) is presented, explaining how they can be utilized for efficient implementation of wireless power transmission systems. A novel WPT topology is proposed, consisting of capacitively coupled OEHRs. This new circuit is evaluated based on measurements, electromagnetic simulations, and equivalent circuits. Results show that the proposed system has enhanced misalignment tolerance.

Finally, the inefficiency of conventional rectifiers in WPT applications operating in MHz frequencies is addressed. The use of a Class E full-wave rectifier

with a capacitive power transfer system is presented, including a design procedure to calculate the required compensation circuits. The results show that this approach can lead to higher efficiencies than a regular full-bridge rectifier, for example, resulting in improved wireless power transfer capabilities.

# Preface

This thesis is an original work by Fabiano Cezar Domingos under the supervision of Dr. Pedram Mousavi. This project has been developed in collaboration with Susanna Vital de Campos de Freitas, who is another M. Sc. student under the supervision of Dr. Mousavi. The present work focuses on: analysis of wireless power transfer systems based on lumped circuit models, open-ended helical resonators, and rectifier circuits. The other's students work concentrates on: planar spiral resonators, design of unit-cell capacitive plates, and matching networks.

Section 3.2.1 of this thesis has been published as F. C. Domingos, S. V. de C. de Freitas, and P. Mousavi, "Overview of Single Conductor Power Transfer with Open-Ended Helical Resonators," in *18th International Symposium on Antenna Technology and Applied Electromagnetics (ANTEM)*, Waterloo, ON, Canada, Aug. 2018.

Section 3.2.2 of this thesis has been partially published as S. V. de C. de Freitas, F. C. Domingos, R. Mirzavand, and P. Mousavi, "Contactless Power Transfer Using Capacitive Resonant Single-Conductor Structure," in *2018 IEEE MTT-S Wireless Power Transfer Conference (WPTC)*, Montreal, QC, Canada, Jun. 2018. Susanna received Best Student Paper Award for this paper.

Additionally, Section 3.2 of this thesis is partially included in a patent application as S. V. de C. de Freitas, F. C. Domingos, R. Mirzavand, and P. Mousavi, "Systems and Methods for Wireless Power Transmission," PCT Patent Application, Dec. 2018.

Chapter 4 of this thesis has been published as F. C. Domingos, S. V. de C. de Freitas, and P. Mousavi, "Capacitive Power Transfer based on Compensa-

tion Circuit for Class E Resonant Full-Wave Rectifier," in *2018 IEEE MTT-S Wireless Power Transfer Conference (WPTC)*, Montreal, QC, Canada, Jun. 2018. The author of this thesis received Best Student Paper Award for this paper.

*To my family and to Susanna.*

*Decide in your heart of hearts what really excites and challenges you, and start moving your life in that direction.*
*Every decision you make, from what you eat to what you do with your time tonight, turns you into who you are tomorrow, and the day after that.*
*Look at who you want to be, and start sculpting yourself into that person.*
*You may not get exactly where you thought you'd be, but you will be doing things that suit you in a profession you believe in.*
*Don't let life randomly kick you into the adult you don't want to become.*

– Chris Hadfield.

# Acknowledgements

First, I would like thank my supervisor, Dr. Pedram Mousavi. His guidance and mentorship were essential for this project and for this program, especially since he always had a smile on his face.

My sincere thanks to all the members of the Intelligent Wireless Technologies laboratory, considering I learned a lot from them.

My love and gratitude to my parents, Valdemir and Sonia, and my brothers, Murilo and Andre, for all the support and dedication. I would not be who I am without them.

More importantly, I would like to express my love to my wife, Susanna. Her love and partnership are vital for me. Happiness is being with her.

# Contents

# List of Tables

# List of Figures

# List of Symbols

| | |
|---|---|
| $\alpha$, $\beta$, $\gamma$, and $\delta$ | Auxiliary variables |
| $\varepsilon_0$ | Permittivity of free space |
| $\lambda$ | Free space wavelength |
| $\mu_0$ | Permeability of free space |
| $\omega$ | Angular frequency |
| $\omega_0$ | Resonance angular frequency |
| $\omega_{max}$ | Angular frequency of $\|S_{21}\|_{max}$ |
| $a_{coil}$ | Radius of coils' wire |
| $a_{res}$ | Radius of resonators' wire |
| $C$ | Capacitance |
| $D$ | Largest dimension of the antenna |
| $Disp_{Tx,Rx}$ | Lateral displacement of Rx |
| $Dist_{res,coil}$ | Distance between resonator and coil |
| $Dist_{res,plate}$ | Distance between resonator and capacitive plate |
| $E$ | Electric field |
| $\mathbf{E}$ | Electric field vector |
| $f$ | Frequency |
| $f_0$ | Resonance frequency |
| $f_H$ | Upper resonance frequency |
| $f_L$ | Lower resonance frequency |
| $f_{max}$ | Frequency of $\|S_{21}\|_{max}$ |
| $Gap_{plate,plate}$ | Parallel plate gap |
| $H$ | Magnetic field |
| $\mathbf{H}$ | Magnetic field vector |
| $k$ | Magnetic coupling coefficient |
| $L$ | Inductance |
| $l_{plate}$ | Side length of square metallic plates |
| $M$ | Mutual inductance |
| $N_{res}$ | Resonators' number of turns |
| $p_{res}$ | Pitch between resonators' turns |
| $Q$ | Loaded quality factor |
| $Q_u$ | Unloaded quality factor |

| | |
|---|---|
| $R$ | Resistance |
| $r$ | Distance to EM source |
| $r_{coil}$ | Coils' radius |
| $r_{res}$ | Resonators' helix radius |
| $\mathbf{S}$ | Poynting vector |
| $S_{21}$ | Forward voltage gain (scattering parameter of a 2-port network) |
| $\|S_{21}\|_{max}$ | Maximum magnitude of $S_{21}$ |
| $t_{plate}$ | Thickness of metallic plates |
| $\frac{V_L}{V_S}$ | Ratio of load voltage by source voltage, or voltage transfer function |
| $X$ | Reactance |
| $Z$ | Impedance |

# List of Abbreviations

| | |
|---|---|
| ac | Alternating Current |
| AWG | American Wire Gauge |
| CPT | Capacitive Power Transfer |
| dc | Direct Current |
| EM | Electromagnetic |
| ESR | Equivalent Series Resistance |
| FEM | Finite Element Method |
| IPT | Inductive Power Transfer |
| OEHR | Open-Ended Helical Resonator |
| RF | Radiofrequency |
| Rx | Receiver |
| SCPT | Single Conductor Power Transfer |
| Tx | Transmitter |
| VNA | Vector Network Analyzer |
| WPT | Wireless Power Transfer |

# Chapter 1

# Introduction

The revolution started by wireless communication will not be completed while power is still transferred by wires. Although impactful, user freedom is not fully existent yet due to the fact that standard power delivery is performed by wires. The widespread usage of electronic devices in personal and industrial applications demonstrates the demand for novel, convenient, and efficient methods for electrical power delivery. It is an evident fact that conventional methods for power transfer do not suffice all purposes. For instance, the requirement for a connection to a wall outlet restricts the user's position and becomes more inconvenient with the growing number of devices utilized. Moreover, the current battery technologies still strive to increase autonomy and performance.

Wireless power transfer (WPT) is an innovative technology seeking to revolutionize how electronic devices are employed. Although the fundamentals of WPT have been known for more than a century, the recent application in wireless charging of mobile phones has been the first widespread utilization of these systems. According to the Wireless Power Consortium [1], over 300 million mobile phones with wireless charging capabilities were commercialized in the year of 2017, along with 75 million wireless charger units. It is expected that the market will expand to 1 billion mobile phones and 500 million chargers sold per year in 2020 [1]. These numbers demonstrate that there is a growing need in the consumer market for WPT, which supports further research efforts to address the existing technologies' limitations and foster development

of innovative, robust, and efficient WPT methods.

The overall purpose of the present thesis is to develop a technology capable of wirelessly transferring power to an electronic device, that is significantly misalignment resistant when compared to the regular WPT. This is achieved by combining capacitive and inductive power transfer methods, which will be further described in the following sections.

## 1.1 Background

The late 19th and early 20th centuries experienced a revolution caused by several groundbreaking inventions in the field of electrical engineering. In the 1880s, the battle of the currents ultimately determined the predominance of Nikola Tesla's alternating current electric power transmission system over Thomas Edison's direct current technology [2]. Guglielmo Marconi's radio transmission over the Atlantic Ocean in 1901 demonstrated the capabilities of wireless communication to replace wired telegraphy [3]. It was during this period that the quest for wireless power transmission also started.

Early experiments of Heinrich Hertz already demonstrated the mechanism of power transmission using radio waves [4]. Hertz utilized antennas to transmit power over long distances in the far-field zone, having several wavelengths of separation between devices, which often requires highly directive antennas to focus the power to a receiver [5]. Additionally, the path loss experienced by the propagating electromagnetic wave can dramatically decrease the overall efficiency. The public interest in WPT was motivated by Tesla and his experiments in wireless power delivery, which established the fundamental principles of using magnetic near-field coupling between coils for WPT in short and medium distances [5].

Unfortunately, there was no major research and development in WPT for the next decades after Tesla, especially since WPT could not surpass the simplicity of wired power transmission systems and due to focus of electrical engineering in the development of radar, radio, and wireless communication technologies. The 30 kW microwave power transmission over 1.6 km at NASA

JPL Goldstone Facility, in 1975, was a breakthrough in high power WPT [6], nonetheless, remaining as a research effort rather than application oriented.

During the past decade, the high power interest shifted towards low and medium power applications, resulting in the creation of wireless charging standards for electronics devices, such as Qi [7] and AirFuel [8]. In order to address the limitations on current technologies, the next generation of WPT requires efficient delivery methods that allow considerable misalignment between devices. Thus, the present study will focus on improving the misalignment of devices in the low and medium power range, while working in the AirFuel standard's frequency.

## 1.2 Motivation

The technological breakthroughs made possible due to WPT have been fostering an increased research activity, as well as the commercialization of numerous consumer products based on these concepts. From a research and development perspective, there are two principal fields of investigation in WPT.

The first approach comprises the underlying mechanisms of power transfer, particularly by seeking knowledge about the possible scientific methods to wirelessly transmit energy from a point to another in space. Additionaly, this field of inquiry analyses how to improve and optimize WPT mechanisms, pushing the limits of technology regarding distance, efficiency, device miniaturization, tolerance to misalignment, and safety.

The second approach includes the development of individual circuit modules required in a functional wireless power transmission system. This includes circuit design considering the specifics of a particular WPT mechanism, ensuring that the module has the appropriate characteristics for that power delivery mechanism. In summary, this approach seeks to increase the overall WPT system's efficiency by performing optimization of an individual circuit module, such as coils, rectifier, or matching circuits, for instance.

### 1.2.1 Wireless Power Transfer Mechanisms

The majority of research and development in wireless power transfer technologies focuses on the energy contained in the electromagnetic (EM) field. Alternative approaches utilize acoustic and ultrasonic coupling between piezoelectric transducers [9]. While this method has certain useful applications in the very low power range [10], due to the biocompatibility of ultrasonic fields and the ability to propagate within metals [9], [11], the scope of this technology is limited regarding higher power levels, which restricts the reach of possible commercial endeavours. On the other hand, EM-based WPT is a method of growing interest, being the enabling technology of several wireless charging products in the last decade, and having the possibility to be applied in the consumer electronics and electric vehicle markets. For these reasons, this thesis will focus on WPT related to electromagnetic field.

Figure 1.1 displays the most common types of WPT systems, with detailed descriptions of EM WPT following in the next section.

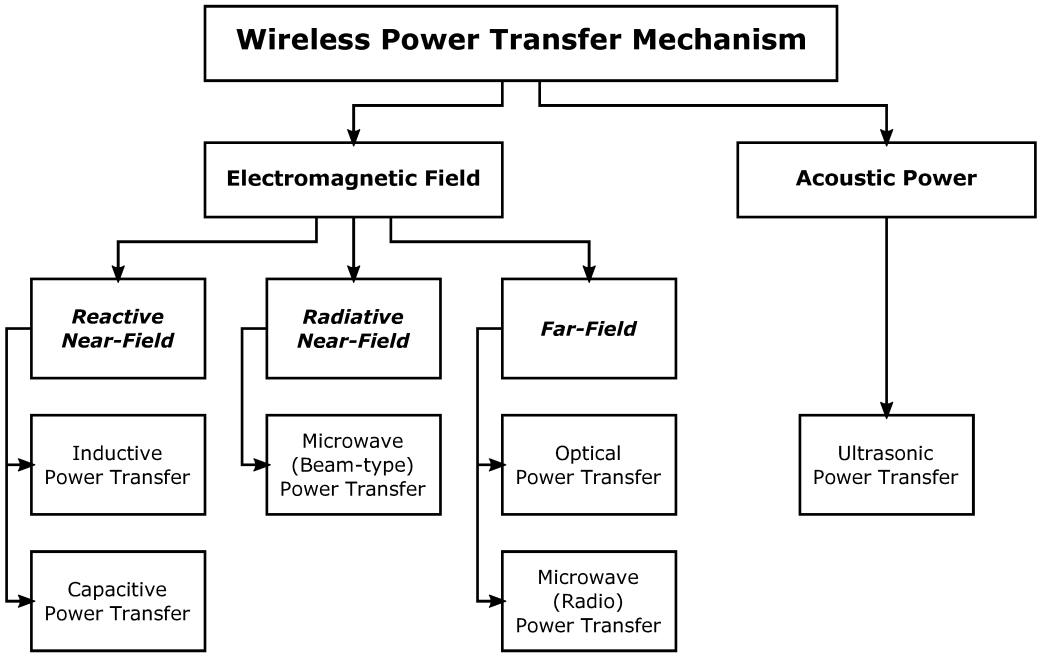


Figure 1.1: Classification of types of wireless power transfer (WPT) mechanisms.

#### 1.2.1.1 Electromagnetic Wireless Power Transfer

The distance between the source and the receiver of the electromagnetic field will determine the type of interaction that enables wireless power delivery. Consequently, WPT mechanisms are classified based on the electromagnetic field regions or zones, defined by Balanis [12] as the reactive near-field, radiative near-field (Fresnel), and far-field (Fraunhofer) regions. Although there is no abrupt change in the field configuration in the boundary between these zones [12], they represent the EM field's behaviour as the distance from the source increases and, therefore, influence the possible manners to deliver power wirelessly.

- **Reactive near-field:** The reactive near-field region surrounds the source of EM fields, which can be an antenna, coil, or any type of radiator. For most antennas, it comprises the region of space where $r < 0.62\sqrt{D^3/\lambda}$ [12], with $r$ being the distance to the source, $D$ being the largest dimension of the antenna, and $\lambda$ being the wavelength at the frequency of operation. In the case of electrically small antennas for which $D \ll \lambda$, the reactive near-field is limited by $r < \lambda/2\pi = 0.16\lambda$ [13]. This region is characterized by the predominance of reactive energy, which is stored and returned to the antenna [14]. No simple relationship exists between the electric field vector **E** and magnetic field vector **H**, and either **E** can dominate over **H** and vice-versa, which will depend on the specific characteristics of the EM source.

  Reactive near-field wireless power transfer traces back to the discovery of electromagnetic induction, having been largely explored by Tesla. Inductive power transfer (IPT) comprises the use of the magnetic field generated by a transmitting coil to induce voltage in a nearby receiving coil, which allows very short distance WPT (usually a few milimeters to centimeters, in the order of magnitude of the coil's diameter). Variations of IPT include the operation in resonant mode [5], [15] and the use of additional coils as repeaters [16], [17], which can increase efficiency and extend the maximum distance up to 5 times the coil's diameter.

Since the establishment of two major standards for IPT in the form of Qi (non-resonant IPT in kHz range with tightly coupled coils [7]) and Airfuel (resonant IPT in MHz range with loosely coupled coils [8]), this technology has been present in many low power consumer devices (up to 5 W) and has become popular in wireless charging for mobile phones.

A second technology of WPT applied in the reactive near-field region is capacitive power transfer (CPT). In this scenario, four separate metallic plates form two capacitors, which are used to couple energy to a load via electric field coupling. While CPT has received an increased attention by research groups in recent years, it still suffers from shorter range than IPT [18], [19]. Additionally, electric field exposure due to fringing fields needs to be considered at increased power levels [20].

- **Radiative near-field:** The radiative near-field (Fresnel) region comprises the volume defined by $0.62\sqrt{D^3/\lambda} \leq r < 2D^2/\lambda$ for large antennas [12], whereas it is bounded by $0.16\lambda \leq r < 5\lambda$ for small antennas [13]. In this region, the radiative fields are dominant and have an angular distribution dependent on the distance from the source [14].

  While the field patterns are not as well defined in this zone as in the far-field [12], it is possible to use beamforming techniques and antenna phased-arrays to focus the energy and steer the beam towards the receiver device [21]. Therefore, WPT methods in the radiative near-field region can be utilized in high power applications with efficiencies near 100 % [21], since path loss effects are not as pronounced as in the far-field. Additionally, appropriate design of the receiving array of rectennas (rectifying antennas) is required in increased power range [22], as well as shaping the beam pattern to optimize efficiency by providing similar power levels to each rectenna element [23].

- **Far-field:** In the far-field (Fraunhofer) region, defined for distances from the source such that $r \geq 2D^2/\lambda$ for most antennas [12] or $r \geq 5\lambda$ for small antennas [13], the radiated fields are predominant and the angu-

lar field distribution does not depend on the distance from the source [14]. Additionally, the **E** and **H** field vectors are well defined by their orthogonal relation, with the power flow (defined by the Poynting vector $\mathbf{S} = \mathbf{E} \times \mathbf{H}$) occurring in the radial direction, outward from the source [14].

Recently, the use of far-field wireless power transfer methods has shifted towards the omnidirectional ultra low power approach, such as in energy harvesting. In these scenarios, sensors and wireless nodes can function entirely based on RF energy, not requiring batteries to operate [24]. Consequently, the number of receivers deployed can be drastically increased due to the reduced required maintenance, which is particularly important for real-time monitoring applications [25] and smart sensors [24]. Additional research efforts in the far-field region include laser and optical power transfer [26].

### 1.2.2 Modules of WPT Systems

Figure 1.2 displays a block diagram for a general system of WPT, based on a particular type of wireless coupling mechanism. The transmitter device consists of an oscillator/amplifier, a matching network, and a transmitting element, while the receiver device comprises a receiving element, a matching network, and a rectifier.

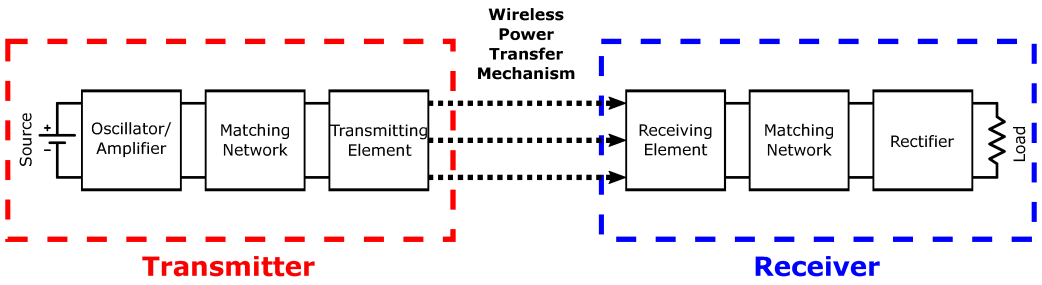


Figure 1.2: Block diagram of a general wireless power transfer system

The most important aspect of a wireless power transmission system is the power transfer mechanism, as presented in the previous section, since it will

enable the power emitted by the transmitter device to reach the receiver, without having direct electrical connection between them.

The description of the remaining blocks of Figure 1.2 are as follows:

- **Oscillator/Amplifier:** since every coupling mechanism of WPT requires high-frequency operation for efficient functioning, the oscillator is necessary to convert the dc energy from the power source to be applicable to the transmitting element. In case of medium and high power applications, the power provided by the oscillator may not be sufficient to drive the transmitting element and an amplifier may be needed.

- **Matching networks:** used to guarantee operation either at the maximum power transfer to the load or maximum efficiency points. For instance, they may be used to convert the amplifier's output and/or load impedances to a suitable value for the transmitting or receiving elements. In some cases, the matching network may just be used as a single reactive element to tune the system's resonance to a desired frequency.

- **Transmitting and receiving element:** dependent on the selected WPT coupling mechanism. For example, they can implemented as coils, electrodes, antennas, etc.

- **Rectifier:** while WPT is performed over ac regime, most of the loads require dc power to function, requiring a rectifier to perform the ac to dc power conversion. It is important that this rectifier is optimized to work at high-frequencies, especially since it should deliver as much as possible of the power that has reached the receiving element to the load.

## 1.3 Objectives

The current thesis investigates the design of resonant WPT systems working at the reactive near-field region and operating at 6.78 MHz, frequency of operation in the AirFuel charging standard.

The first part of this thesis will focus on providing a basic theoretical knowledge of near-field wireless power transfer mechanisms from a circuit analysis

perspective. Due to the increasing quantity of topologies existent in near-field WPT, it can be difficult to actually understand their advantages and disadvantages, unless they are evaluated using the exact same criteria. Consequently, four of the most important topologies are studied on this thesis, namely: two-coil non-resonant, two-coil resonant, and four-coil resonant inductive power transfer circuits, additional to the resonant capacitive power transfer topology. For these topologies, a consistent approach will be presented based on three parameters: the frequency of optimal power transfer ($f_{max}$ for non-resonant and $f_0$ for resonant configurations), the maximum forward voltage gain ($|S_{21}|_{max}$), and tolerance to changes in distances between transmitter and receiver.

Next, this thesis will further develop the previous analysis in near-field WPT systems by introducing the implementation of high quality factor resonating circuits with open-ended helical resonators (OEHR). Characterization methods for OEHR available in the literature will be discussed, with a novel wireless power transmission topology using capacitively coupled open-ended helical resonators being proposed. This innovative WPT system is implemented, being verified by measurements, finite element method (FEM) simulations, and by equivalent circuit analysis. In addition, considerations regarding electric and magnetic fields in this system will be discussed, along with safety considerations.

Finally, the last part of the thesis will address coherent WPT module design, considering a system-level approach for WPT. Particularly, it will address the inefficiency of conventional rectifiers in MHz frequencies required for wireless power transfer. A novel application of a class E full-wave rectifier in a capacitive power transfer system will be presented to seek an overall efficient WPT system in high frequencies. Additionally, design considerations for required compensation inductors are made based on this particular choice of rectifier and WPT mechanism.

## 1.4 Thesis Structure

This thesis is organized into five chapters, including the the introduction and conclusion chapters.

Chapter 2 contains a comparative analysis between common near-field WPT topologies. Analyzed topologies include: inductive coupling (two-coil configuration in non-resonant and resonant operation, and four-coil configuration in resonant operation) and resonant capacitive coupling.

Chapter 3 explores the use of open-ended helical resonators for WPT. A novel WPT system based on capacitively coupled OEHRs is proposed and studied based on circuit analysis, electromagnetic simulations, and measurements. Furthermore, the effects of distance, misalignment, and resonator-plate spacing in the WPT capabilities are examined.

Chapter 4 discusses the unsuitability of conventional rectifiers due to adverse effects caused by frequencies required for WPT. An application of a high efficiency Class E full-wave resonant rectifier is proposed to capacitive power transfer systems, with necessary equations for compensation inductors being derived.

Finally, the conclusion summarizes the accomplishments presented in this thesis and lists suggestions for future research in this topic.

# Chapter 2

# Near-field Wireless Power Transfer Systems

This chapter presents the theory of near-field wireless power transfer systems, including inductive power transfer (IPT) and capacitive power transfer (CPT). Equations to characterize different topologies are derived analytically from circuit models, particularly to emphasize the differences of the non-resonant and resonant circuits.

In order to analyze a wireless power transfer system, three parameters are important:

- **Power transmission capability:** due to simplicity and convenience of using vector network analyzers in the experimental measurements, WPT systems are usually characterized using scattering or S-parameters [27] instead of efficiency. In this thesis, power transmission capabilities are described by finding $|S_{21}|_{max}$, as power transfer efficiency is proportional to $|S_{21}|^2$ [28].

- **Frequency of maximum power transfer:** frequency in which $|S_{21}|_{max}$ occurs. Usually happens at a fixed resonance frequency $f_0$ for resonant topologies and at a variable frequency $f_{max}$ for non-resonant configurations.

- **Robustness to weaker coupling interaction:** necessary to understand the effect of increased distances between transmitter and receiver

devices. It depends on the magnetic coupling factor for IPT and coupling capacitances for CPT systems.

## 2.1 Inductive Coupling

Inductive power transfer (IPT) systems utilize magnetic field interaction between two inductances to allow contactless power delivery to a load. Due to their nature of operation, they are also denominated inductive coupling or magnetic coupling WPT systems.

Figure 2.1 illustrates the general mechanism of a wireless power transmission topology using inductive coupling between one pair of coils.

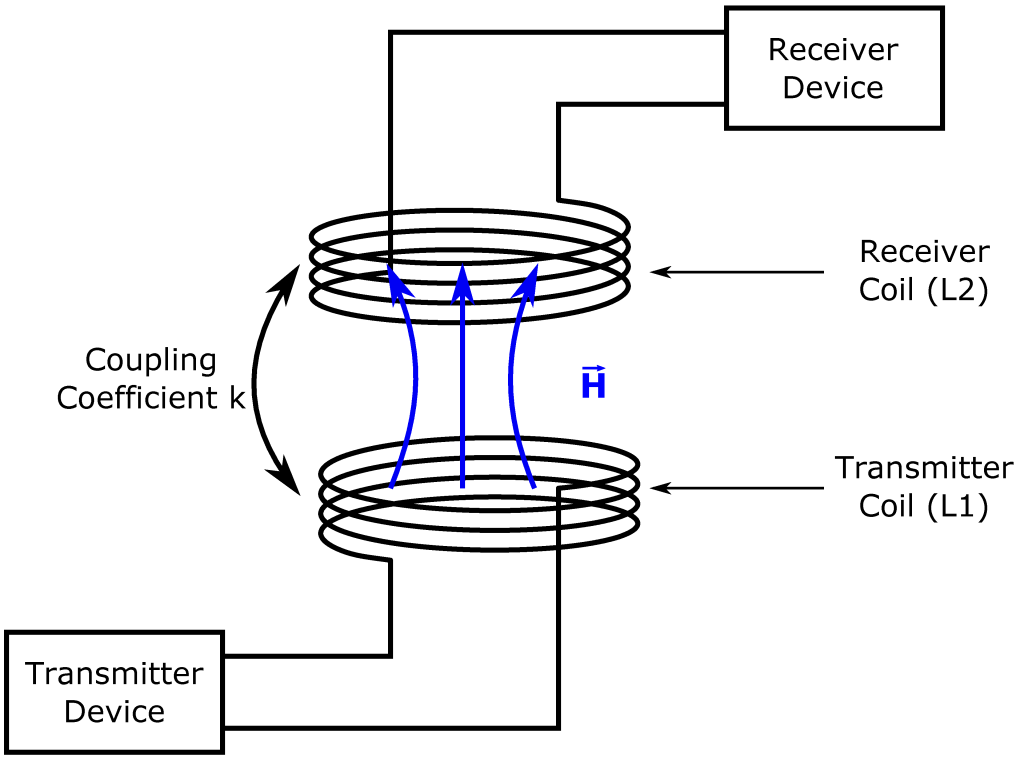


Figure 2.1: General inductive power transfer system

In order to characterize the performance of IPT systems, it is first necessary to define some variables. The circuit parameters that describe the behaviour of two mutually coupled inductors $L_1$ and $L_2$ are: the magnetic coupling coefficient $k$ and the mutual inductance $M$, which are defined as (2.1):

$$k = \frac{M}{\sqrt{L_1 L_2}} \tag{2.1}$$

The coupling factor $k$ decays rapidly as the distance increases between coils, being proportional to $1/distance^3$ [27].

### 2.1.1 Two-Coil Non-resonant Inductive Coupling

The simplest circuit of inductive power transfer is an air-core transformer, having its primary and secondary windings magnetically coupled and separated by a certain distance in free space.

Figure 2.2 represents the circuit diagram of a non-resonant inductive coupling WPT system. In this circuit, $V_S$ represents the voltage source with its internal resistance $R_S$, and $V_L$ is the voltage delivered to a load of value $R_L$. The inductors $L_1$ and $L_2$ are magnetically coupled according to the coefficient $k$, with the losses in each inductor being quantified by their respective equivalent series resistances (ESR) $R_1$ and $R_2$.

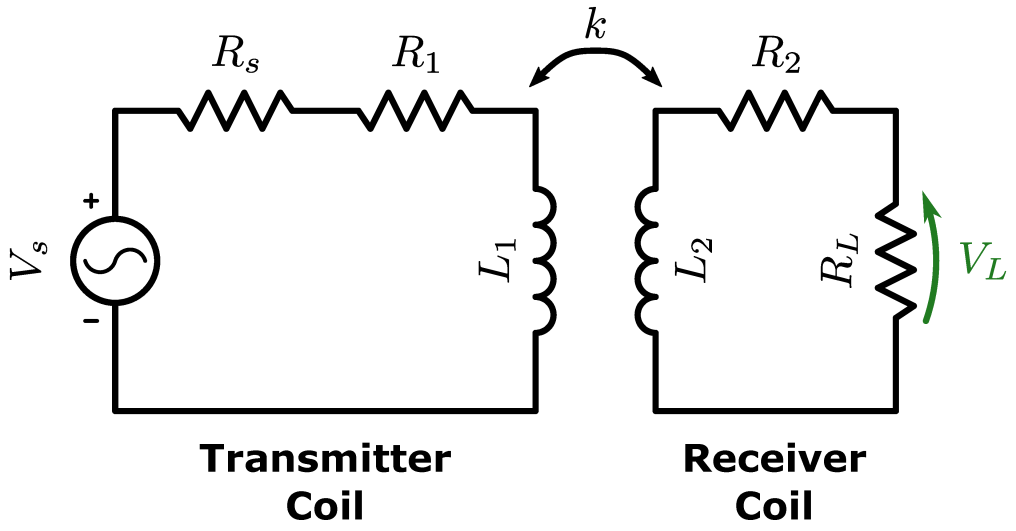


Figure 2.2: Circuit model for non-resonant inductive coupling

Once a circuit model for a WPT system has been established, the next step consists in finding a relation to evaluate the wireless power link's performance. Based on the circuit model of Figure 2.2 and considering two clockwise mesh currents $I_1$ and $I_2$, it is possible to derive the following set of linear equations:

$$\begin{bmatrix} R_S + R_1 + j\omega L_1 & j\omega M \\ j\omega M & R_2 + R_L + j\omega L_2 \end{bmatrix} \times \begin{bmatrix} I_1 \\ I_2 \end{bmatrix} = \begin{bmatrix} V_S \\ 0 \end{bmatrix} \tag{2.2}$$

By solving (2.2) and knowing that $V_L = I_2 R_L$, it is possible to obtain the voltage transfer function $V_L/V_S$:

$$\frac{V_L}{V_S} = \frac{-j\omega R_L k\sqrt{L_1 L_2}}{(R_S + R_1 + j\omega L_1)(R_L + R_2 + j\omega L_2) + \omega^2 k^2 L_1 L_2} \tag{2.3}$$

A voltage gain $V_L/V_S$ can be converted to an equivalent scattering parameter $S_{21}$ by using the following equation [27]:

$$S_{21} = 2\frac{V_L}{V_S}\sqrt{\frac{R_S}{R_L}} \tag{2.4}$$

Consequently, $S_{21}$ of a two-coil non-resonant inductive coupling circuit, following the circuit model of Figure 2.2, is found as:

$$S_{21} = \frac{-j2\omega k\sqrt{L_1 L_2}}{(R_S + R_1 + j\omega L_1)(R_L + R_2 + j\omega L_2) + \omega^2 k^2 L_1 L_2}\sqrt{R_S R_L} \tag{2.5}$$

Equation (2.5) characterizes the frequency response of the non-resonant IPT topology. In a WPT system, there are two fundamental parameters needed to understand the circuit's operation, namely the frequency of operation and power transfer capability. Due to the characteristics of this topology, there is not a single fixed frequency (such as a resonance frequency) that could be used for operation. Consequently, it is useful to find an equation that determines the frequency of operation $f_{max}$ (or $\omega_{max} = 2\pi f_{max}$) in which power transfer occurs most efficiently. Then, the power transfer behaviour at this frequency can be calculated.

In other words, we are interested to find $\omega_{max}$ that maximizes the magnitude of $S_{21}$, *i.e.* $|S_{21}|_{max}$. First, we find $|S_{21}|$ by taking the magnitude of (2.5):

$$|S_{21}| = \frac{\omega\alpha}{\sqrt{\beta^2 + \omega^2(2\beta\gamma + \delta^2) + \omega^4\gamma^2}} \tag{2.6}$$

where the auxiliary variables $\alpha$, $\beta$, $\gamma$, and $\delta$ are defined as:

$$\begin{cases} \alpha = 2k\sqrt{L_1 L_2}\sqrt{R_S R_L} \\ \beta = R_S R_L + R_S R_2 + R_1 R_L + R_1 R_2 \\ \gamma = L_1 L_2 (k^2 - 1) \\ \delta = L_1 (R_L + R_2) + L_2 (R_S + R_1) \end{cases} \tag{2.7}$$

When $\omega = \omega_{max}$, the derivative $\frac{d}{d\omega}|S_{21}|$ is zero, indicating a maximum point for $|S_{21}|$. Therefore:

$$\frac{d}{d\omega}|S_{21}| = \frac{\alpha(\beta^2 - \omega^4\gamma^2)}{(\beta^2 + \omega^2(2\beta\gamma + \delta^2) + \omega^4\gamma^2)^{3/2}} \tag{2.8}$$

$$\frac{d}{d\omega}|S_{21}| = 0 \implies \beta^2 - \omega_{max}^4\gamma^2 = 0 \tag{2.9}$$

For Equation (2.9), only one solution for $\omega_{max}$ is purely real and positive. As a result, the frequency that yields $|S_{21}|_{max}$ is:

$$\omega_{max} = \frac{\beta}{-\gamma} = \frac{R_S R_L + R_S R_2 + R_1 R_L + R_1 R_2}{L_1 L_2 (1 - k^2)} \tag{2.10}$$

Next, by evaluating equation (2.6) at the angular frequency $\omega_{max}$ given by (2.10), it is possible to find the maximum magnitude for $|S_{21}|$:

$$|S_{21}|_{max} = \frac{\alpha}{\delta} = \frac{2k\sqrt{L_1 L_2}\sqrt{R_S R_L}}{L_1 (R_L + R_2) + L_2 (R_S + R_1)} \tag{2.11}$$

These two equations are instrumental to understand the behaviour of the two-coil non-resonant IPT topology. Firstly, (2.10) describes that $\omega_{max}$ is highly variant according to the coupling factor $k$. Particularly, this can be seen by the fact that $\omega_{max}$ approaches infinity as $k$ tends to unity. Secondly, equation (2.11) is equally important, describing how $|S_{21}|_{max}$ changes according to system variations. $|S_{21}|_{max}$ is directly proportional to $k$, meaning that as soon as the magnetic coupling between transmitter and receiver coil is reduced, the power transfer capabilities will be degraded. In other words, the maximum efficiency is only attainable if there is 100 % magnetic flux coupling between transmitter and receiver coils, which is extremely unlikely in any practical WPT application.

To better illustrate the behaviour of the two-coil non-resonant IPT system, the deduced equations are evaluated and plotted based on the components from Table 2.1.

Table 2.1: Components used to evaluate the equations deduced for the two-coil non-resonant topology

| **Component** | **Value** |
|---|---|
| $R_S = R_L$ | 50 Ω |
| $L_1 = L_2$ | 10 $\mu$H |
| $R_1 = R_2$ | 2.13 Ω |

The first plot, Figure 2.3, displays the frequency behaviour of $|S_{21}|$ for selected values of the coupling factor $k$, according to equation (2.6). Note how the peak $|S_{21}|$ sharply reduces as $k$ decreases, which also causes the peak's frequency to shift to lower values. The 3-D plot of Figure 2.4 shows a more detailed curve for $|S_{21}|$ versus a continuous interval of $k$ from 0 to 1.

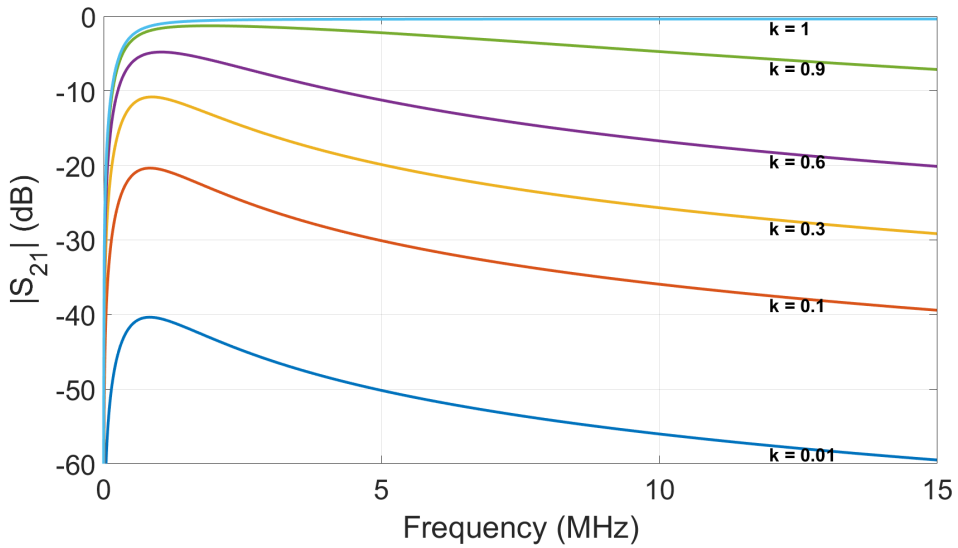


Figure 2.3: $|S_{21}|$ for two-coil non-resonant inductive coupling

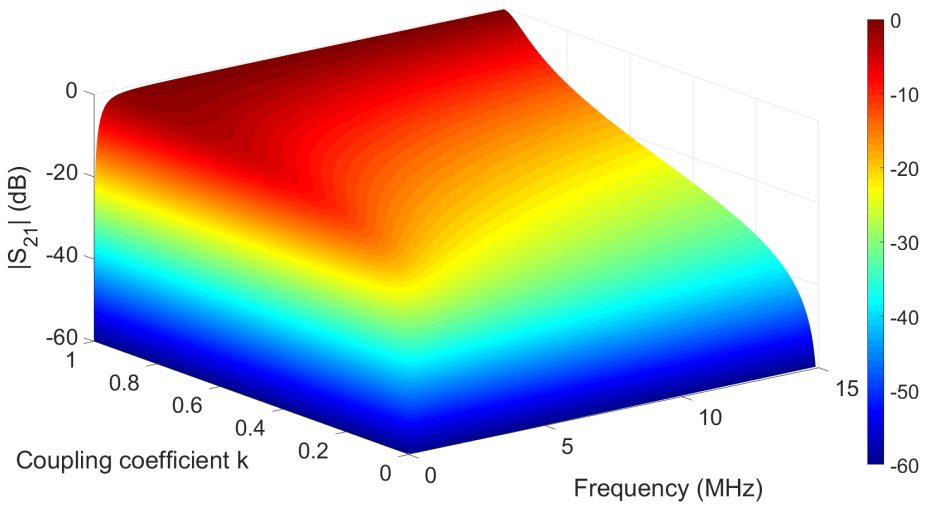


Figure 2.4: 3-D plot of $|S_{21}|$ for two-coil non-resonant inductive coupling

Next, Figure 2.5 illustrates the relationship between $|S_{21}|_{max}$ and $k$. Efficient power transfer only occurs given that $k$ is closer to unity.

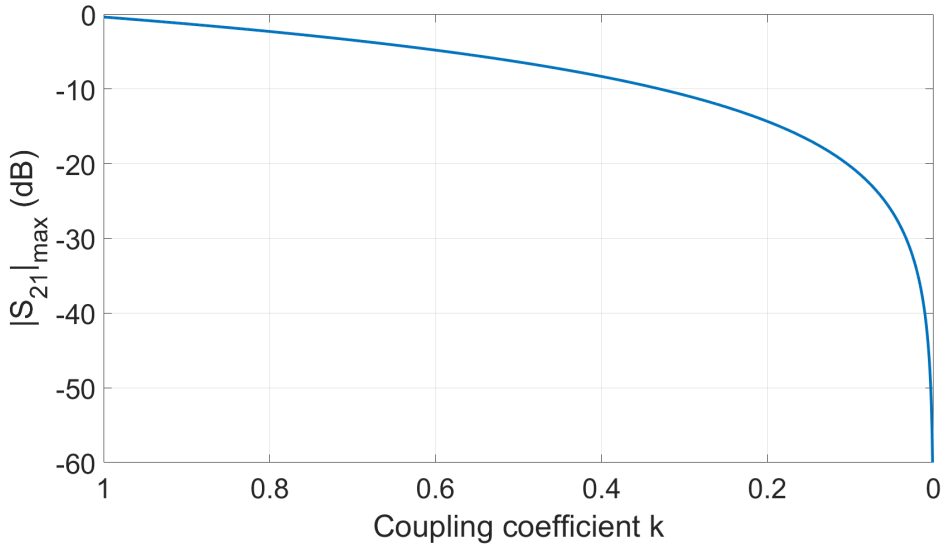


Figure 2.5: $|S_{21}|_{max}$ as a function of $k$ for two-coil non-resonant inductive coupling

Finally, Figure 2.6 complements the previous plot, showing that $f_{max}$ is also very dependent on the value of $k$. $f_{max}$ increases dramatically as $k$ tends to one.

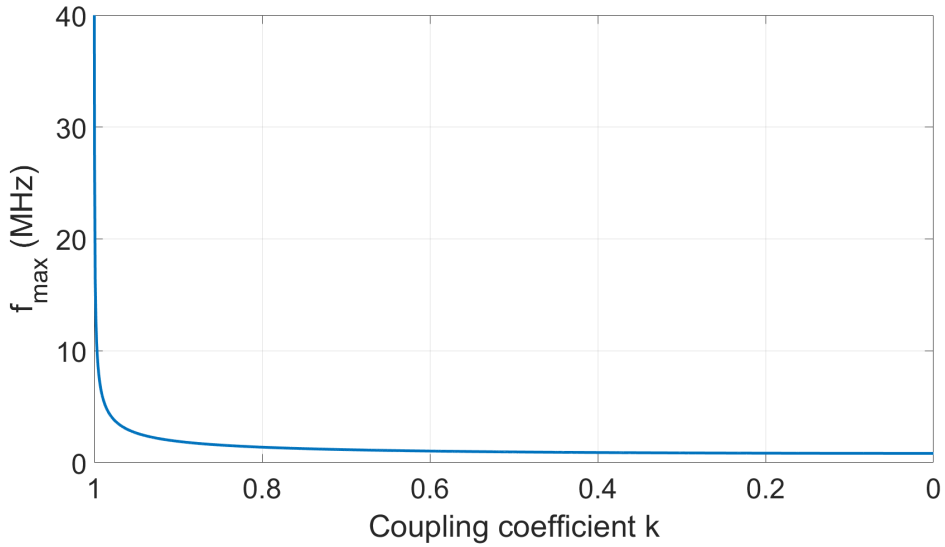


Figure 2.6: $f_{max} = \omega_{max}/2\pi$ as a function of $k$ for two-coil non-resonant inductive coupling

From a practical standpoint, this topology is limited due to the high dependence of the relation between efficiency, frequency, and coupling coefficient. Consequently, minimal changes in position or orientation between devices will cause a change in the frequency of optimal operation, as well as a decrease efficiency to a point that may prevent power transfer. Due to these reasons, even though the two-coil non-resonant configuration may be limited, it can serve some restricted applications. For example, it can be applicable when devices are constrained to a well-known position and distance, guaranteeing that the coupling coefficient will be previously known and the WPT system can be designed for that particular configuration.

### 2.1.2 Resonant Inductive Coupling

Considering the severe limitations of the non-resonant inductive technology, alternative topologies are explored in WPT. Based on the theory of resonance for different fields of engineering and physics, it is notable that objects operating in a resonant condition tend to exchange energy much more efficiently than their non-resonant counterparts [29]. The use of resonant circuits is a standard practice in WPT established by Tesla [5], which applied resonance principles to allow range extension and efficient power transfer. For the case

of IPT, resonant inductive coupling utilizes capacitors to resonate with the self-inductance of the coils, allowing operation at the resonant frequency with more efficiency than the non-resonant topology.

#### 2.1.2.1 Two-Coil Resonant Inductive Coupling

The two-coil resonant inductive coupling circuit is similar to the non-resonant circuit presented in Section 2.1.1 and in Figure 2.2, however with the addition of two series capacitors to cause resonance at the frequency of interest $f_0$ or angular frequency $\omega_0 = 2\pi f_0$. Figure 2.7 displays this new circuit topology.

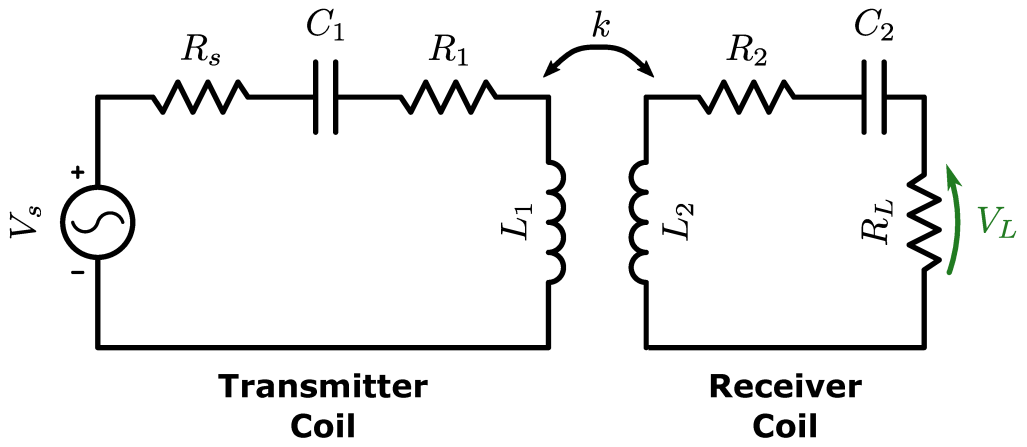


Figure 2.7: Circuit model for two-coil resonant inductive coupling.

The series capacitors $C_1$ and $C_2$ are chosen such that they cancel the reactances introduced by the self-inductances $L_1$ and $L_2$, according to (2.12). Additionally, they ensure that both the transmitter and receiver coils will resonate at the same frequency $f_0$. Usually, the coils are constructed first to accommodate for design constraints such as limited space and weight, as well as WPT distance requirements. Then, the capacitors are calculated for the chosen coils based on the following equation:

$$f_0 = \frac{1}{2\pi\sqrt{L_1 C_1}} = \frac{1}{2\pi\sqrt{L_2 C_2}} \tag{2.12}$$

This compensation topology is denominated series-series [30], due to the addition of two series capacitors, being one of the most commonly applied in

practice [30]–[32]. While other configurations exist for two-coil resonant IPT, including parallel and series-parallel combinations of compensation capacitors, these will be not further investigated in this thesis, as they are generally applied to accommodate extreme (low or high) values of source and load impedances, including high power supply protection [30].

Following a similar procedure to the non-resonant configuration, the set of linear equations (2.13) is used to characterize this new topology:

$$\begin{bmatrix} R_S + R_1 + j\omega L_1 - \frac{j}{\omega C_1} & j\omega M \\ j\omega M & R_2 + R_L + j\omega L_2 - \frac{j}{\omega C_2} \end{bmatrix} \times \begin{bmatrix} I_1 \\ I_2 \end{bmatrix} = \begin{bmatrix} V_S \\ 0 \end{bmatrix} \quad (2.13)$$

By solving these equations, the voltage transfer function $V_L/V_S$ is obtained as (2.14). Although the equation for the voltage transfer function is similar to the non-resonant case, the frequency response will be altered due to the resonant behaviour introduced by the capacitive reactances of $C_1$ and $C_2$.

$$\frac{V_L}{V_S} = \frac{-j\omega R_L k\sqrt{L_1 L_2}}{(R_S + R_1 + j\omega L_1 - \frac{j}{\omega C_1})(R_2 + R_L + j\omega L_2 - \frac{j}{\omega C_2}) + \omega^2 k^2 L_1 L_2} \quad (2.14)$$

By converting $V_L/V_S$ into $S_{21}$ using (2.4), it is possible to obtain:

$$S_{21} = \frac{-j2\omega k\sqrt{L_1 L_2}}{(R_S + R_1 + j\omega L_1 - \frac{j}{\omega C_1})(R_2 + R_L + j\omega L_2 - \frac{j}{\omega C_2}) + \omega^2 k^2 L_1 L_2} \sqrt{R_S R_L} \quad (2.15)$$

At the resonance frequency $\omega = \omega_0$, the reactances of $L_1$ and $L_2$ are respectively cancelled by $C_1$ and $C_2$, *i.e.* $j\omega L_1 - \frac{j}{\omega C_1} = 0$ and $j\omega L_2 - \frac{j}{\omega C_2} = 0$. In this condition, the denominator of (2.15) becomes purely real, which greatly simplifies the equation for $S_{21}$ at $\omega_0$:

$$S_{21}|_{\omega=\omega_0} = \frac{-j2\omega_0 k\sqrt{L_1 L_2}}{(R_S + R_1)(R_2 + R_L) + \omega_0^2 k^2 L_1 L_2} \sqrt{R_S R_L} \quad (2.16)$$

Whenever possible, it is generally common to evaluate the resonating circuits based on the quality factor of the $RLC$ resonating circuit, rather than the specific value of inductance or resistance. The unloaded quality factor for the resonating Tx and Rx coils is given by:

$$Q_{u1} = \frac{\omega_0 L_1}{R_1}, Q_{u2} = \frac{\omega_0 L_2}{R_2} \tag{2.17}$$

Nevertheless, in this particular circuit, as shown in the schematic of Figure 2.7, the coils are in series with the source resistance $R_S$ and load resistance $R_L$. Consequently, these series resistances have a loading effect on the resonators and, as result, it is necessary to consider the loaded quality factors $Q$ instead of considering the unloaded quality factors $Q_u$. Thus, $Q_1$ and $Q_2$ are defined as:

$$Q_1 = \frac{\omega_0 L_1}{R_S + R_1}, Q_2 = \frac{\omega_0 L_2}{R_L + R_2} \tag{2.18}$$

Therefore, considering the quality factors defined in (2.18), the S-parameter $S_{21}$ at resonance is:

$$S_{21}|_{\omega=\omega_0} = \frac{-2jk\sqrt{Q_1 Q_2}}{1 + k^2 Q_1 Q_2} \sqrt{\frac{R_S R_L}{(R_S + R_1)(R_L + R_2)}} \tag{2.19}$$

From (2.19), we are interested to find the value of the coupling coefficient $k = k_{crit}$ that maximizes $|S_{21}|$ at the frequency of resonance. First, it is needed to find the derivative of $|S_{21}|_{\omega=\omega_0}$ with respect to $k$:

$$\frac{d}{dk}(|S_{21}|_{\omega=\omega_0}) = 2\frac{\sqrt{Q_1 Q_2}(1 - k^2 Q_1 Q_2)}{1 + k^2 {Q_1 Q_2}^2} \sqrt{\frac{R_S R_L}{(R_S + R_1)(R_L + R_2)}} \tag{2.20}$$

At the value $k = k_{crit}$ that maximizes $|S_{21}|$ at $\omega_0$, then $\frac{d}{dk}\big(|S_{21}|_{\omega=\omega_0}\big) = 0$. Therefore, we can find $k_{crit}$:

$$k_{crit} = \frac{1}{\sqrt{Q_1 Q_2}} = \frac{1}{\omega_0} \sqrt{\frac{(R_S + R_1)(R_L + R_2)}{L_1 L_2}} \tag{2.21}$$

For $k < k_{crit}$, the system is said to be undercoupled, whereas for $k = k_{crit}$ it is critically coupled, and for $k > k_{crit}$ the circuits are overcoupled. Finally, by substituting (2.21) back into (2.19), we find:

$$|S_{21}|_{max} = \sqrt{\frac{R_S R_L}{(R_S + R_1)(R_L + R_2)}} \tag{2.22}$$

Unlike the non-resonant configuration, which relied on high $k$ for good $|S_{21}|$, the resonant topology's $|S_{21}|_{max}$ occurs at $k_{crit}$, which is usually considerably smaller than unity when the quality factors are large. Ultimately, this means that the resonant topology can be operated at longer distances than the non-resonant circuit, without compromising in power transfer efficiency.

While this analysis is similar to [32], Equation (2.22) is more complete than the equation presented in [32], which assumes identical transmitter and receiver modules, as well as same load and source resistances.

Table 2.2 lists the parameters used to evaluate the two-coil resonant circuit. In order to compare it with the non-resonant counterpart, the same parameters are used to evaluate this new topology, except for the addition of capacitors $C_1$ and $C_2$.

Table 2.2: Components used to evaluate the equations deduced for the two-coil resonant topology

| **Component** | **Value** |
|---|---|
| $R_S = R_L$ | 50 Ω |
| $L_1 = L_2$ | 10 $\mu$H |
| $R_1 = R_2$ | 2.13 Ω |
| $C_1 = C_2$ | 55.1 pF |
| $Q_{u1} = Q_{u2}$ | 200 |
| $Q_1 = Q_2$ | 8.172 |
| $f_0$ | 6.78 MHz |

For this example circuit, the deduced equations (2.21) and (2.22) result in $k_{crit} = 0.122$ and $|S_{21}|_{max} = 0.959 =$ -0.362 dB.

Figures 2.8 and 2.9 display $|S_{21}|$ versus coupling coefficient $k$. As it is possible to perceive from the performance of this topology, the peak of transmission is maintained at the resonant frequency $f_0$ for low $k$ values (undercoupling), until it reaches the critical coupling point of $k_{crit}$ and the corresponding $|S_{21}|_{max}$ is achieved. At this point, the system presents the best power transmission at the designed resonance frequency. If the coupling coefficient is increased above $k_{crit}$, the transmission has two distinct peaks at frequencies different than $f_0$: a

lower frequency $f_L$ and an upper frequency $f_H$. As the coupling factor continues to increase, the overcoupling makes the two resonances to become further spread apart. This important phenomenon is characteristic of resonant IPT systems, being known as frequency splitting [27].

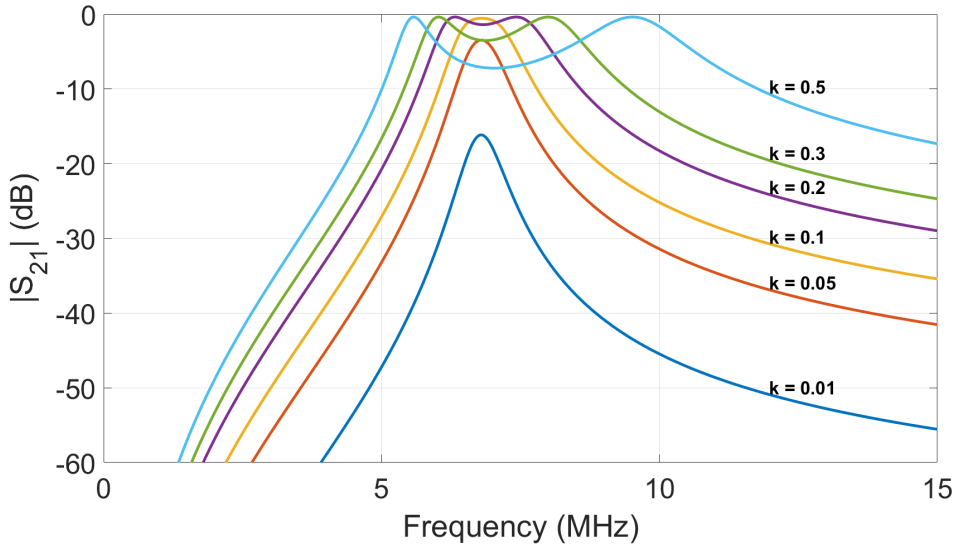


Figure 2.8: $|S_{21}|$ for two-coil resonant inductive coupling

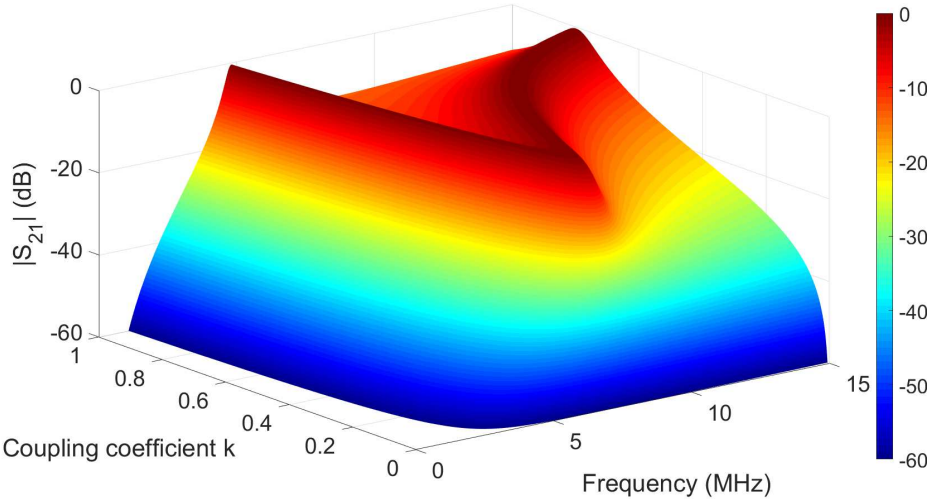


Figure 2.9: 3-D plot of $|S_{21}|$ for two-coil resonant inductive coupling

The plot for $|S_{21}|$ at the resonance frequency 6.78 MHz is shown in Figure 2.10. The transmission slowly increases as $k$ is reduced, until the peak of $|S_{21}|$ occurs at $k_{crit} = 0.122$, then the curve rapidly decays.

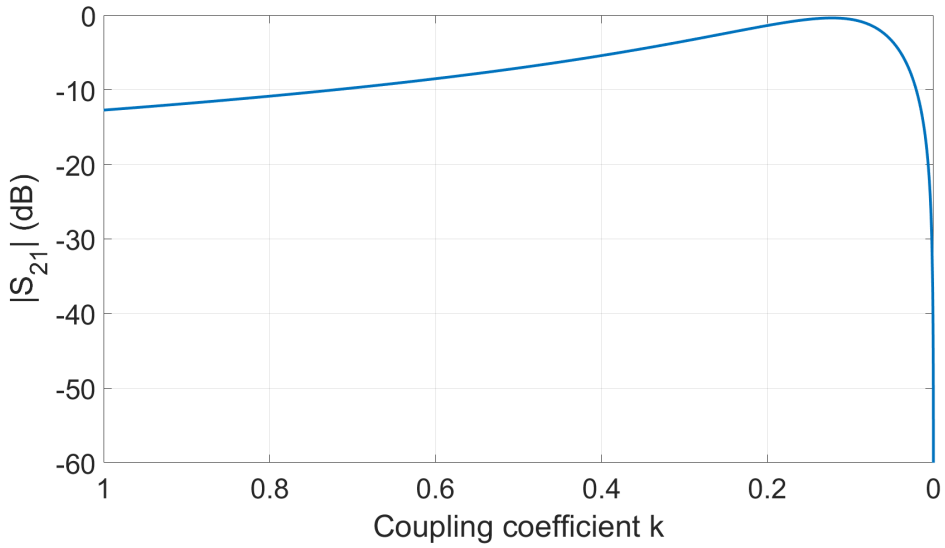


Figure 2.10: $|S_{21}|$ at $f_0 = 6.78$ MHz for two-coil resonant inductive coupling.

Considering practical applications, the ideal point of operation is at critical coupling due to maximum transmission at $f_0$, but implementation requires a fixed transmitter-receiver configuration in space to not alter the coupling coefficient. If the system is designed to operate at undercoupled regime, the frequency is fixed as $f_0$, but $|S_{21}|$ decays fast. Furthermore, the operation in the overcoupled regime means constant power transmission capabilities over a wide range of coupling factors, however demanding a dynamic frequency tracking to function at $f_L$ or $f_H$, or a dynamic circuit tuning to shift the frequency to $f_0$.

#### 2.1.2.2 Four-Coil Resonant Inductive Coupling

Figure 2.11 represents the circuit diagram of a four-coil resonant inductive coupling WPT system. Instead of two resonant circuits realizing directly magnetic coupling from the source to the load, this topology presents a total of four resonant coils, being two on the transmitter side and two on the receiver side.

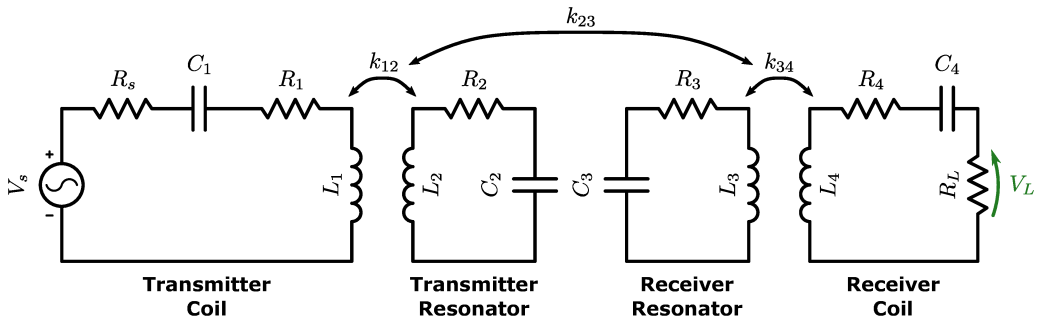


Figure 2.11: Circuit model for four-coil resonant inductive coupling

On the transmitter side, the source is connected to a coil composed of a capacitor $C_1$ and an inductor $L_1$, which is then coupled via $k_{12}$ to the resonator composed of $L_2$ and $C_2$. The power transmission between Tx and Rx occurs only via $k_{23}$, which couples to a similar pair of resonator then coil, coupled via $k_{34}$, ultimately transferring power to the load. $R_1$, $R_2$, $R_3$, and $R_4$ are the respective self-resistances of each inductor. While the coils tend to be constructed with few turns or often as a single wire loop, the resonators are built with numerous turns with the intention of having large inductances and maximizing their quality factor.

The magnetic cross coupling factors ($k_{13}$, $k_{14}$, and $k_{24}$) are ignored to simplify the circuit analysis. According to [27], these coupling factors are usually very small or negligible, resulting in minor differences in the final outcomes.

All four coils are tuned to resonate at the same frequency $f_0$, such that:

$$f_0 = \frac{1}{2\pi\sqrt{L_1C_1}} = \frac{1}{2\pi\sqrt{L_2C_2}} = \frac{1}{2\pi\sqrt{L_3C_3}} = \frac{1}{2\pi\sqrt{L_4C_4}} \tag{2.23}$$

Based on the circuit diagram, it is possible to obtain a set of four equations to describe the circuit:

$$\begin{bmatrix} Z_1 & j\omega M_{12} & 0 & 0 \\ j\omega M_{12} & Z_2 & j\omega M_{23} & 0 \\ 0 & j\omega M_{23} & Z_3 & j\omega M_{34} \\ 0 & 0 & j\omega M_{34} & Z_4 \end{bmatrix} \times \begin{bmatrix} I_1 \\ I_2 \\ I_3 \\ I_4 \end{bmatrix} = \begin{bmatrix} V_S \\ 0 \\ 0 \\ 0 \end{bmatrix} \tag{2.24}$$

where impedances $Z_1$, $Z_2$, $Z_3$, $Z_4$ are defined as:

$$\begin{cases} Z_1 = R_S + R_1 + j\omega L_1 - \dfrac{j}{\omega C_1} \\ Z_2 = R_2 + j\omega L_2 - \dfrac{j}{\omega C_2} \\ Z_3 = R_3 + j\omega L_3 - \dfrac{j}{\omega C_3} \\ Z_4 = R_4 + R_L + j\omega L_4 - \dfrac{j}{\omega C_4} \end{cases} \tag{2.25}$$

The voltage ratio $\frac{V_L}{V_S}$ is obtained by solving (2.24) and (2.25):

$$\frac{V_L}{V_S} = \frac{j\omega^3 k_{12}k_{23}k_{34}L_2L_3\sqrt{L_1L_4}R_L}{Z_1Z_2Z_3Z_4 + \omega^4 k_{12}^2k_{34}^2L_1L_2L_3L_4 + \omega^2\left(k_{12}^2L_1L_2Z_3Z_4 + k_{23}^2L_2L_3Z_1Z_4 + k_{34}^2L_3L_4Z_1Z_2\right)} \tag{2.26}$$

Then, converting to $S_{21}$:

$$S_{21} = \frac{2j\omega^3 k_{12}k_{23}k_{34}L_2L_3\sqrt{L_1L_4}\sqrt{R_SR_L}}{Z_1Z_2Z_3Z_4 + \omega^4 k_{12}^2k_{34}^2L_1L_2L_3L_4 + \omega^2\left(k_{12}^2L_1L_2Z_3Z_4 + k_{23}^2L_2L_3Z_1Z_4 + k_{34}^2L_3L_4Z_1Z_2\right)} \tag{2.27}$$

Considering the unloaded and loaded quality factors:

$$Q_{u1} = \frac{\omega_0 L_1}{R_1}, Q_{u2} = \frac{\omega_0 L_2}{R_2}, Q_{u3} = \frac{\omega_0 L_3}{R_3}, Q_{u4} = \frac{\omega_0 L_4}{R_4} \tag{2.28}$$

$$Q_1 = \frac{\omega_0 L_1}{R_S + R_1}, Q_2 = Q_{u2} = \frac{\omega_0 L_2}{R_2}, Q_3 = Q_{u2} = \frac{\omega_0 L_3}{R_3}, Q_4 = \frac{\omega_0 L_4}{R_L + R_4} \tag{2.29}$$

At $\omega = \omega_0$, each coil is in resonance and impedances $Z_1$ to $Z_4$ become purely real. Therefore, $|S_{21}|$ is simplified to:

$$\begin{aligned} S_{21}|_{\omega=\omega_0} =& \frac{2jk_{12}k_{23}k_{34}Q_2Q_3\sqrt{Q_1Q_4}}{1 + k_{12}^2Q_1Q_2 + k_{23}^2Q_2Q_3 + k_{34}^2Q_3Q_4 + k_{12}^2k_{34}^2Q_1Q_2Q_3Q_4} \\ & \times \sqrt{\frac{R_SR_L}{(R_S + R_1)(R_L + R_2)}} \end{aligned} \tag{2.30}$$

Since coil-resonator couplings ($k_{12}$ and $k_{34}$) are usually fixed, and only $k_{23}$ is changed when the transmitter-receiver distance increases, one is interested to find $k_{23} = k_{23crit}$ that maximizes $|S_{21}|$, *i.e.* $\frac{d}{dk_{23}}\left(S_{21}|_{\omega=\omega_0}\right) = 0$. Therefore, it is possible to obtain:

$$k_{23crit} = \sqrt{\frac{(1 + k_{12}^2 Q_1 Q_2)(1 + k_{34}^2 Q_3 Q_4)}{Q_2 Q_3}} \tag{2.31}$$

Substituting (2.31) into (2.30) yields:

$$|S_{21}|_{max} = \frac{k_{12} k_{34} \sqrt{Q_1 Q_2 Q_3 Q_4}}{\sqrt{(1 + k_{12}^2 Q_1 Q_2)(1 + k_{34}^2 Q_3 Q_4)}} \sqrt{\frac{R_S R_L}{(R_S + R_1)(R_L + R_4)}} \tag{2.32}$$

The equations deduced above are more complete than normally presented in literature [27], [32], due to the consideration of all elements in the circuit without approximations that may not be valid for all cases. For example, reference [32] assumes that transmitter and receiver coils are identical, *i.e.* $Q_1 = Q_4$, $Q_2 = Q_3$, and $R_1 = R_4$, as well as assuming that the source resistance $R_S$ is equal to the load resistance $R_L$. While realistic for some applications, such as measuring symmetrical coils in 50 Ω ports of a VNA, it is not practical to assume that this will always be the case, especially due to the widespread expansion of WPT systems that require loads other than 50 Ω, as well as the existence of several amplifiers that present a very low output impedance. Additionally, the complex design of a coil in IPT requires exact level of attention regarding losses, which may not allow simplifications such as presented in [27], which disregards the coils' resistance and losses. Fortunately, the deduced equations in this thesis can be checked by applying the simplifications proposed in the literature.

Table 2.3 lists the circuit parameters used in the subsequent plots, as means to demonstrate the behaviour of the four-coil IPT system. Resonators have the same characteristics of the two-coil cases previously analyzed. Coils have one-tenth of the resonators' inductance, but same unloaded quality factor.

Table 2.3: Components used to evaluate the equations deduced for the four-coil resonant topology

| **Component** | **Value** |
|---|---|
| $R_S = R_L$ | 50 Ω |
| $L_1 = L_4$ | 1 $\mu$H |
| $L_2 = L_3$ | 10 $\mu$H |
| $R_1 = R_4$ | 0.213 Ω |
| $R_2 = R_3$ | 2.13 Ω |
| $C_1 = C_4$ | 551 pF |
| $C_2 = C_3$ | 55.1 pF |
| $k_{12} = k_{34}$ | 0.2 |
| $Q_{u1} = Q_{u2} = Q_{u3} = Q_{u4}$ | 200 |
| $Q_1 = Q_4$ | 0.848 |
| $Q_2 = Q_3$ | 200 |
| $f_0$ | 6.78 MHz |

For this example circuit, $k_{23crit} = 0.039$ and $|S_{21}|_{max} = 0.868$ = -1.231 dB.

Figures 2.12 and 2.13 show $|S_{21}|$ versus coupling coefficient $k_{23}$. For this analysis, $k_{12}$ and $k_{34}$ are kept constant, while only $k_{23}$ is varied. From these plots, it is possible to identify the same frequency splitting phenomenon as the two-coil case, but the four-coil circuit presents sharper resonant peaks than the two-coil topology, due to no loading effect on resonators. An in-depth comparison between the two-coil and four-coil resonant topologies is presented in the next section.

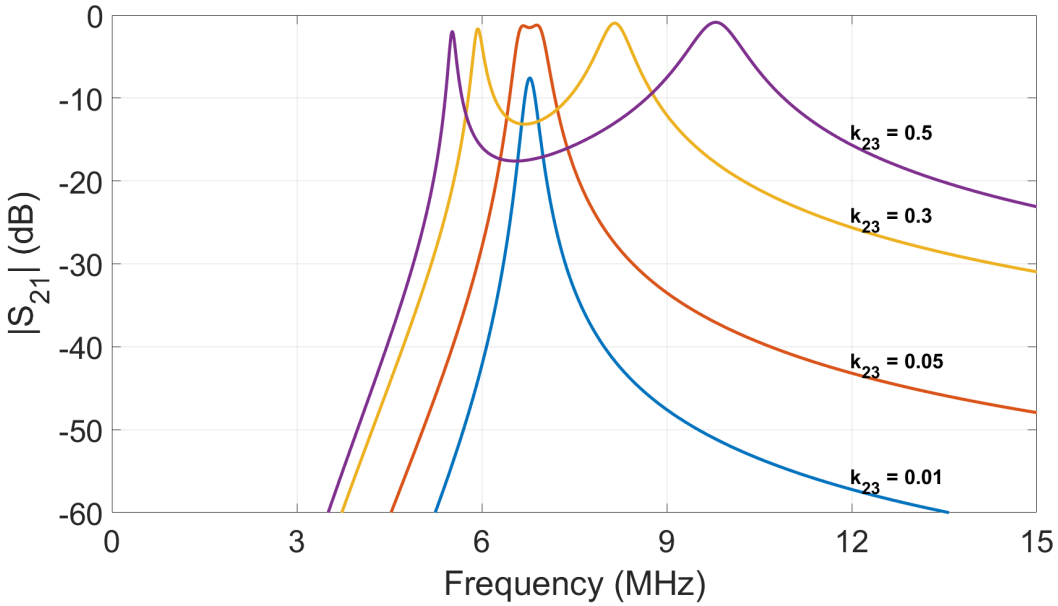


Figure 2.12: $|S_{21}|$ for four-coil resonant inductive coupling

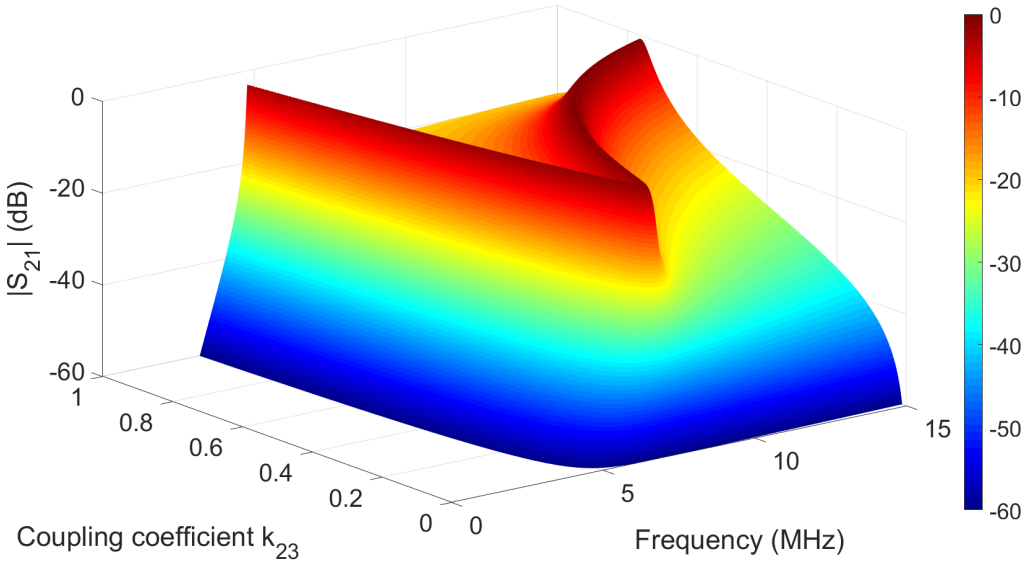


Figure 2.13: 3-D plot of $|S_{21}|$ for four-coil resonant inductive coupling

The plot for $|S_{21}|$ at the resonance frequency 6.78 MHz is shown in Figure 2.14. The peak of $|S_{21}|$ = -1.231 dB occurs at $k_{23crit}$ = 0.039, indicating a slight decrease in transmission, but an extremely small critical coupling factor. Therefore, resonators can be much more spaced apart and still operate at the peak of transmission. This fact suggests that range extension can be considered one of the main advantages of this topology over the previous IPT circuits presented.

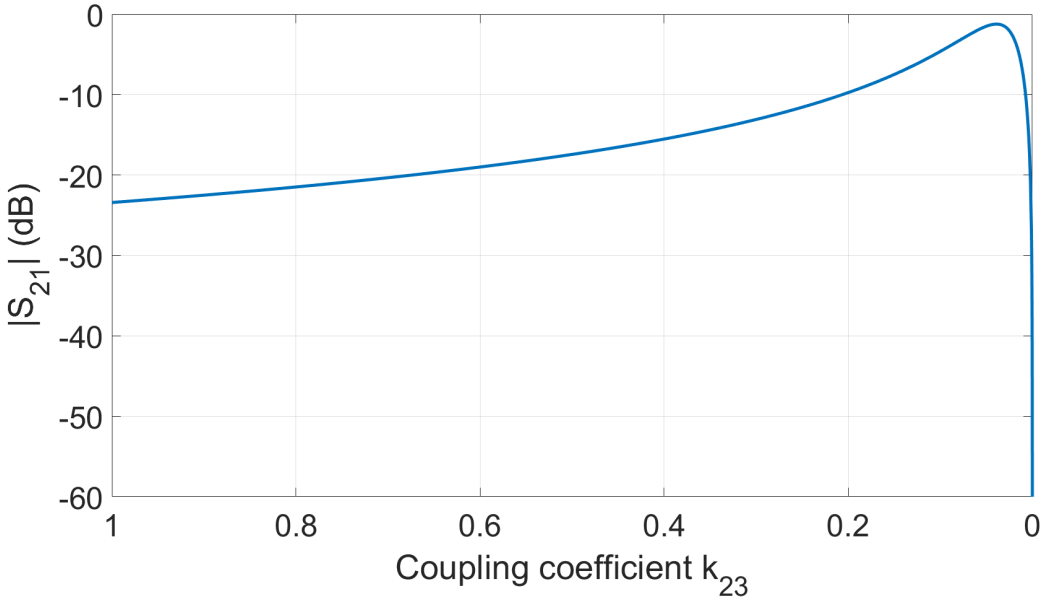


Figure 2.14: $|S_{21}|$ at $f_0 = 6.78$ MHz for four-coil resonant inductive coupling

#### 2.1.2.3 Comparison between Two and Four-Coil Resonant IPT Topologies

The four-coil topology can be thought as an extension of the two-coil case. In the original two-coil circuit, the transmitter resonator is directly connected to the source, whereas the receiver resonator drives the load. Rather than connecting the resonators to source and load resistances, which ultimately causes a loading effect and reduces the resonators' loaded quality factor, the four-topology has an additional coil to couple the source and first resonator, as well as another coil between second resonator to load. Therefore, it is important to understand the conditions for one topology to be more effective than the other.

The first comparison regards how well the power is transferred. Maximum $S_{21}$ for the two-coil topology found in equation (2.22) is limited only by losses in the resonators, *i.e.* $|S_{21}|_{max,two-coil}$ tends to 1 as $R_1 \ll R_S$ and $R_2 \ll R_L$. However, maximum $S_{21}$ for the four-coil topology deduced in (2.32) is more complex, being composed of a multiplication of two terms. The first term is always less than one and depends on the Q factor of the coils and resonators ($Q_1$, $Q_2$, $Q_3$, and $Q_4$), as well as the coil-resonator coupling factors ($k_{12}$ and $k_{34}$). The second term in the multiplication is similar to $|S_{21}|_{max,two-coil}$, but depends on the usually smaller coil resistances ($R_1$ and $R_4$ in the four-coil topology), rather than the more elevated resonator resistances ($R_1$ and $R_2$ in the two-coil topology).

Thus, $|S_{21}|_{max,four-coil}$ will be lower than $|S_{21}|_{max,two-coil}$, unless $k_{12}^2 Q_1 Q_2 \gg 1$ and $k_{34}^2 Q_3 Q_4 \gg 1$. In this particular case, $|S_{21}|_{max,four-coil} \approx |S_{21}|_{max,two-coil}$. If $R_{1,four-coil} = R_{4,four-coil}$ are lower than $R_{1,two-coil} = R_{4,two-coil}$, it is possible that $|S_{21}|_{max,four-coil}$ is slightly larger than $|S_{21}|_{max,two-coil}$.

This analysis suggests that in order to maximize $S_{21}$, it is necessary to have a large quality factor in coils and resonators, as well as maximizing coil-resonator coupling ($k_{12}$ and $k_{34}$).

Figure 2.15 shows the comparison between two-coil and four-coil resonator topologies regarding $|S_{21}|_{max}$ as a function of unloaded Q factor of coils and resonators. This plot considers the same circuit parameters listed in Table 2.2 and Table 2.3. In general, all cases benefit from high quality factors, confirming that Q maximization leads to increased power transfer efficiency. Additionally, the two-coil topology is superior regarding $|S_{21}|_{max}$ in almost all cases, except when the coil-resonator coupling ($k_{12} = k_{34}$) is almost close to 1, then the four-coil topology presents better transmission characteristics.

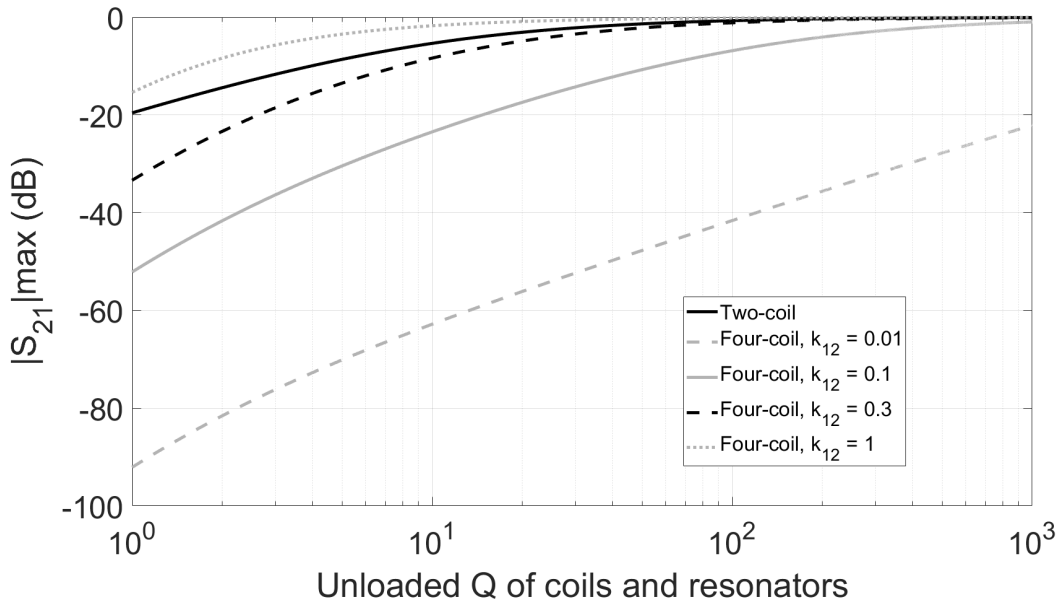


Figure 2.15: $|S_{21}|_{max}$ as a function of unloaded quality factor of coils and resonators for two-coil and four-coil resonant IPT topologies

The second comparison between topologies concerns the distance between transmitter and receiver, represented by the resonator-resonator coupling factor ($k$ for two-coil and $k_{23}$ for four-coil topology). In order to extend the distance capabilites of resonant IPT, it is necessary to decrease the critical coupling coefficient $k_{crit}$ or $k_{23crit}$. This means that a lower magnetic flux coupling is required between resonators to reach the maximum $|S_{21}|$ for the IPT topology, which ultimately represents more distance allowed between devices. In this analysis, we want to know if the two-coil topology with two resonators can have its range extended by placing two additional coils and transforming it into a four-coil topology.

The four-coil critical coupling coefficient $k_{23crit}$ found in (2.31) has to be lower than the two-coil equivalent $k_{crit}$ found in (2.21). Thus, we are interested in finding the coil-resonator coupling $k_{12}$ and $k_{34}$ such that:

$$k_{23crit,four-coil} < k_{crit,two-coil} \tag{2.33}$$

for the same set of resonators in the two topologies.

For the following deduction, a few assumptions are made to simplify the

analysis. The system is assumed to be symmetric, such that transmitter and receiver are equal, as well as $k_{12}$ is equal to $k_{34}$. Also, it is important to note that the Tx and Rx resonators are under different loading conditions on each topology. In the two-coil topology, the resonators are loaded either by the source or load resistances, whereas they are unloaded in the four-coil case, but with the coils being loaded instead. The subscripts are used to clarify if a given quality factor is from a certain topology.

Therefore, it is necessary to meet $k_{12} < k_{12,threshold}$ to increase IPT range, where the threshold value for this coupling factor is defined as:

$$k_{12,threshold} = \sqrt{\frac{Q_{2,four-coil} - Q_{1,two-coil}}{Q_{1,four-coil}Q_{2,four-coil}Q_{1,two-coil}}} \tag{2.34}$$

Contrary to first analysis of this chapter, where a higher coil-resonator coupling was sought to maximize power transfer, the equation (2.34) suggests that this coupling has to be reduced to lead to a range extension between devices. Furthermore, there is an essential trade-off between power transfer efficiency and distance in four-coil IPT, suggesting that $k_{12}$ and $k_{34}$ are important design parameters in this type of circuit.

Figure 2.16 shows the comparison between two-coil and four-coil resonator topologies regarding $k_{crit}$ as a function of unloaded Q factor of coils and resonators. Considering the same circuit parameters listed in Table 2.2 and Table 2.3, $k_{12,threshold} = 0.372$. Therefore, the four-coil topology has a lower critical coupling point whenever $k_{12} < k_{12,threshold}$, which can be seen in the plot. Consequently, even though the $k_{12}$ decrease leads to small reduction in power transfer capabilities, it can result in significant WPT range increase.

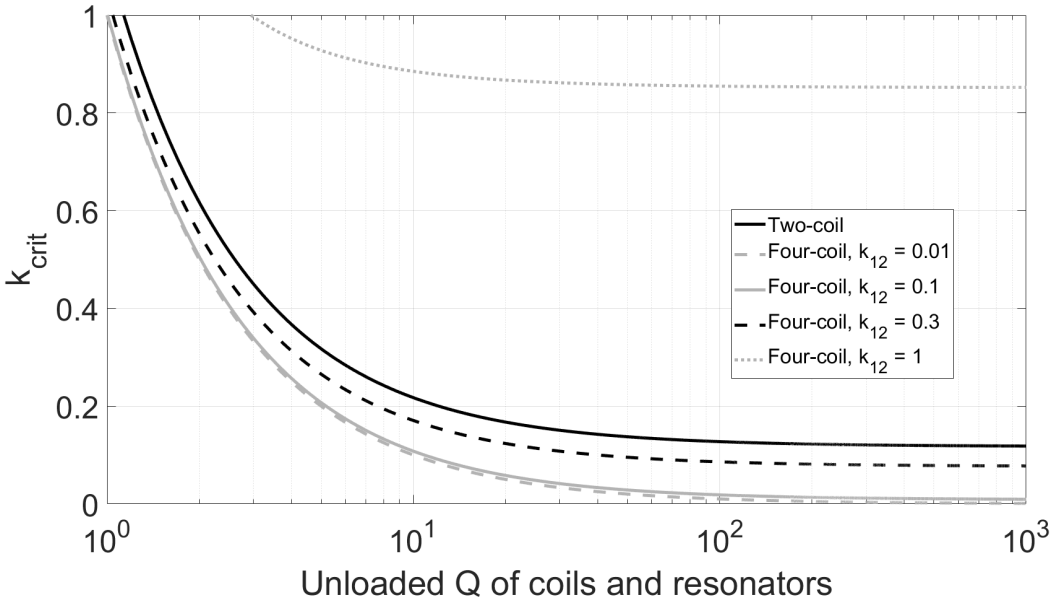


Figure 2.16: $k_{crit}$ as a function of unloaded quality factor of coils and resonators for two-coil and four-coil resonant IPT topologies

## 2.2 Capacitive Coupling

In capacitive power transfer (CPT) systems, electric field coupling allows contactless power delivery from a transmitter to a receiver device via metallic plates [18], [19], [33]. For this reason, they are also denominated as capacitive coupling or electric field coupling WPT systems.

Figure 2.17 illustrates the general mechanism of a wireless power transmission topology using capacitive coupling between two transmitter plates and two receiver plates. Consequently, wireless power delivery is provided by two coupling capacitors, denominated forward capacitor ($C_f$) and return capacitor ($C_r$). Cross-coupling between plates are usually not considered, unless the coupling capacitances are extremely small [34].

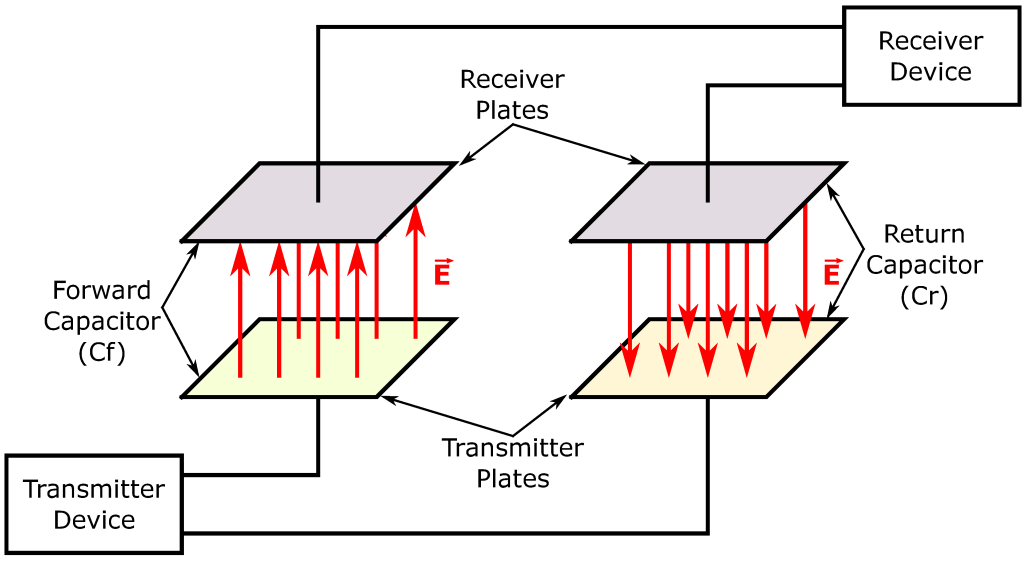


Figure 2.17: General capacitive power transfer system

### 2.2.1 Resonant Capacitive Coupling

Unlike inductive coupling, capacitive coupling is generally only used in resonant operation. In non-resonant mode, CPT requires unusually large coupling capacitors to be applicable [35].

Figure 2.18 represents the circuit diagram of a resonant capacitive power transfer system. The contactless power transfer via electric field is represented in the circuit model by the coupling capacitors $C_f$ (forward capacitor) and $C_r$ (return capacitor). To operate in resonance, two compensation inductors $L_1$ and $L_2$ are inserted in series, along with their respective resistive losses represented by $R_1$ and $R_2$.

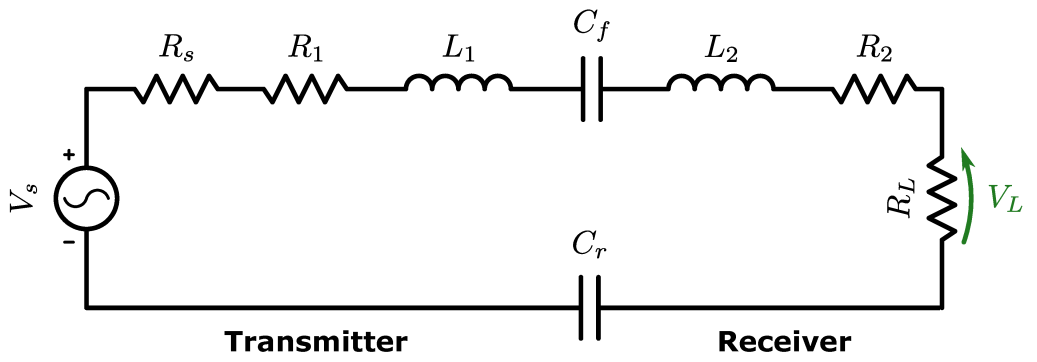


Figure 2.18: Circuit model for capacitive coupling

A common limiting factor for CPT is related to the capacitors involved. Normally, the dielectric is air, the plates' area is limited by the application, and the gap between plates may be considerable (in the order of a few centimeters). For these reasons, the coupling capacitances are commonly very small, usually in the range of hundreds of picofarads, leading to elevated reactances required to be cancelled by the compensation inductors. Consequently, the losses in the inductors will be elevated, becoming the ultimate limiting factor in designing a CPT system.

The circuit analysis leads to:

$$V_S = (R_S + R_1 + R_L + R_2 + j\omega L_1 + j\omega L_2 - \frac{j}{\omega C_f} - \frac{j}{\omega C_r})I_1 \tag{2.35}$$

The voltage transfer ratio can then be found as:

$$\frac{V_L}{V_S} = \frac{R_L}{R_S + R_1 + R_L + R_2 + j\omega(L_1 + L_2) - \frac{j}{\omega C_f} - \frac{j}{\omega C_r}} \tag{2.36}$$

By converting to $S_{21}$ and finding its magnitude, one can obtain:

$$S_{21} = \frac{2\sqrt{R_S R_L}}{R_S + R_1 + R_L + R_2 + j\omega(L_1 + L_2) - \frac{jC_f C_r}{\omega C_f C_r}} \tag{2.37}$$

$$|S_{21}| = \frac{2\sqrt{R_S R_L}}{\sqrt{(R_S + R_1 + R_L + R_2)^2 + \left(\omega(L_1 + L_2) - \frac{C_f C_r}{\omega C_f C_r}\right)^2}} \tag{2.38}$$

At resonant frequency, $j\omega_0(L_1 + L_2) - \frac{jC_fC_r}{\omega_0 C_f C_r} = 0$. Therefore:

$$f_0 = \frac{1}{2\pi}\sqrt{\frac{C_f + C_r}{C_f C_r(L_1 + L_2)}} \tag{2.39}$$

By assuming that the circuit is in the resonant condition, $S_{21}$ is greatly simplified. Additionally,

$$|S_{21}|_{\omega=\omega_0} = |S_{21}|_{max} = \frac{2\sqrt{R_S R_L}}{R_S + R_1 + R_L + R_2} \tag{2.40}$$

From the circuit diagram, it can be seen that transmitter and receiver form a single series resonator. The unloaded and loaded quality factors are respectively defined as:

$$Q_u = \frac{\omega_0(L_1 + L_2)}{R_1 + R_2} = \frac{C_f + C_r}{\omega_0 C_f C_r(R_1 + R_2)} \tag{2.41}$$

$$Q = \frac{\omega_0(L_1 + L_2)}{R_1 + R_2 + R_S + R_L} = \frac{C_f + C_r}{\omega_0 C_f C_r(R_1 + R_2 + R_S + R_L)} \tag{2.42}$$

Table 2.4 lists the components used to evaluate the capacitive resonant topology. The unloaded factor and resonance frequency are the same applied to evaluate the IPT circuits previously.

Table 2.4: Components used to evaluate the equations deduced for the capacitive topology

| **Component** | **Value** |
|---|---|
| $R_S = R_L$ | 50 Ω |
| $C_f = C_r$ | 1000 pF |
| $L_1 = L_2$ | 551 nH |
| $R_1 = R_2$ | 0.117 Ω |
| $Q_u$ | 200 |
| $Q$ | 0.4684 |
| $f_0$ | 6.78 MHz |

Figures 2.19 and 2.20 display the variation of $|S_{21}|$ according to coupling capacitors $C_f = C_r$.

Since both transmitter and receiver devices work collectively as one resonator, all the circuit resistances, as well as the source and load resistances, load the same resonator. Therefore, the curves are much broader than the sharp peaks of IPT. While the nominal coupling capacitors are 1000 pF, this topology presents impressive transmission characteristics even for frequencies and capacitances significantly different. However, CPT for large distances is not feasible, since smaller coupling capacitors ($<$ 100pF, meaning increased distances) require larger inductors, which may limit $|S_{21}|_{max}$ due to $R_1$ and $R_2$.

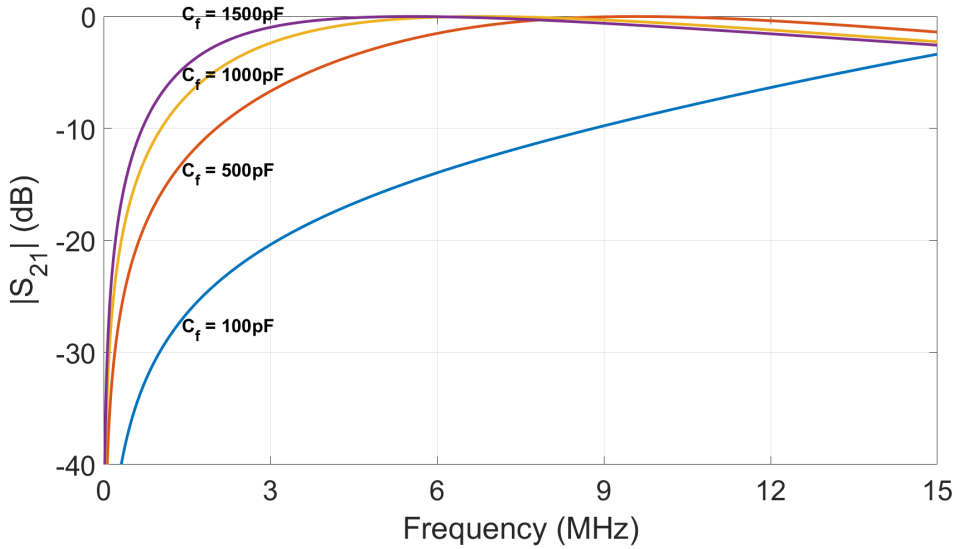


Figure 2.19: $|S_{21}|$ for capacitive coupling and selected values of $C_f = C_r$

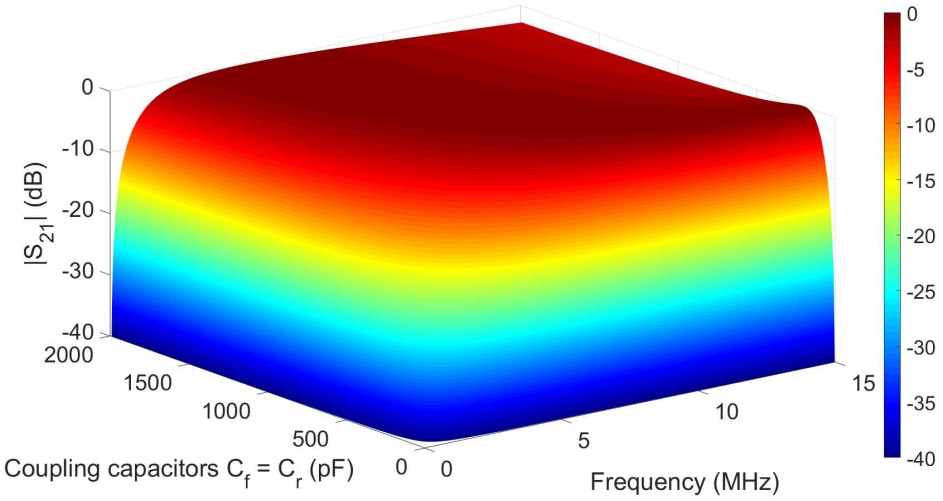


Figure 2.20: 3-D plot of $|S_{21}|$ for capacitive coupling

The curve for $|S_{21}|$ at the $f_0 = 6.78$ MHz is shown in Figure 2.21. The peak of transmission occurs at the nominal value of coupling capacitor for which the compensation inductors were designed. Higher values of capacitance do not impact $|S_{21}|$ considerably. For lower capacitances than 1000 pF, $|S_{21}|$ starts to drop, but at a more moderate rate than the sharp slopes of inductive topologies in the undercoupled region.

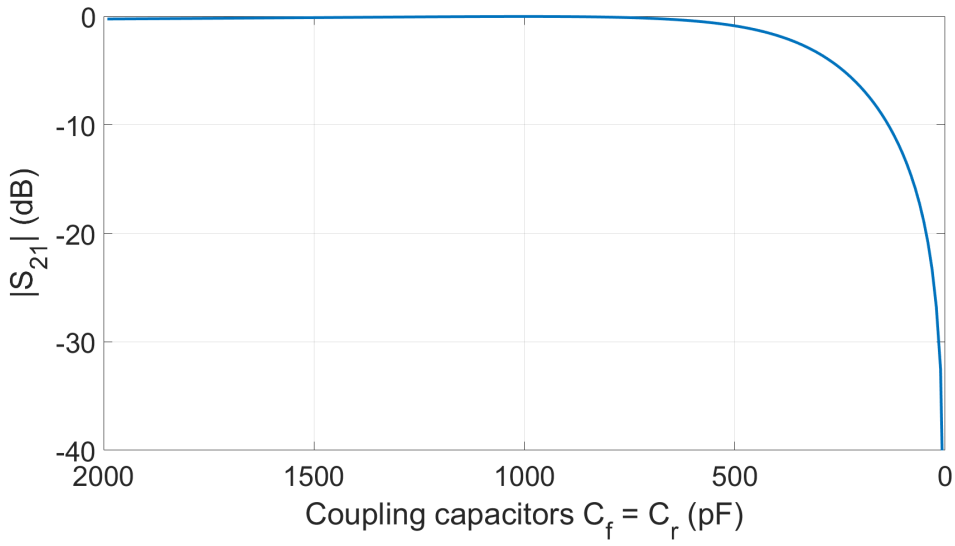


Figure 2.21: $|S_{21}|$ at $f_0 = 6.78$ MHz for capacitive coupling

Therefore, it can be concluded that CPT has a shorter range than IPT

for operation at the optimal point. However, CPT is more robust to changes in distance, particularly since the coupling capacitances decay proportionally to $1/distance$, versus the drop of $k$ as $1/distance^3$ in IPT. Additionally, misalignment tolerance is drastically improved, as IPT requires direct line-of-sight, whereas CPT benefits from the electric field coupling existing as long as the devices are not fully shielded [35].

## 2.3 Chapter Summary

This chapter demonstrated the characteristics of common near-field WPT systems deduced based on circuit analysis.

First, inductive coupling topologies were studied. It was found that non-resonant configuration requires values of magnetic coupling coefficient $k$ close to unity in order to operate efficiently, having the disadvantage of not presenting a fixed frequency of operation. In contrast, resonant inductive coupling has a peak of transmission for $k_{crit}$, which is usually much smaller than unity, meaning that the optimal point of operation occurs at increased distances from the transmitter. Additionally, while usually two-coil resonant IPT has a slightly better efficiency, the four-coil topology can greatly extend the distance range for WPT.

Next, capacitive power transfer was analyzed. While it works mostly on short distances, CPT has the advantage of being more tolerant to moderate changes in the coupling capacitances, resulting in more robustness to misalignment compared to IPT.

Finally, the theoretical understanding of IPT and CPT presented in this chapter will be useful for the subsequent chapters of this thesis, where inductive and capacitive coupling stages will be applied in the derivation of novel WPT systems.

# Chapter 3

# Wireless Power Transfer using Capacitively Coupled Open-Ended Helical Resonators

While Chapter 2 described WPT topologies mainly based on circuit models, this chapter introduces the analysis based on the construction of the resonant circuits. Resonators are important elements required in WPT, and maximizing their quality factors have a positive impact regarding optimal power transfer capabilities.

This chapter focuses on the utilization, properties, and advantages of open-ended helical resonators for near-field wireless power transfer applications. Additionally, a new topology using this type of resonator is proposed and verified by electromagnetic simulations, circuit analysis of an equivalent model, and measurements.

## 3.1 Open-Ended Helical Resonators

The journal publication [29] authored by an MIT research group in 2007 had two important contributions to the field of WPT, as depicted in Figure 3.1. Firstly, it was the original proposal of a four-coil IPT system and, as presented in Chapter 2, it can greatly extend the distance range if designed correctly. Secondly, it introduced a novel type of resonator for WPT applications, denominated open-ended helical resonator (OEHR). As the name suggests, this circuit is composed of a wire forming a helical coil, with both ends being open

and unconnected. There are no electrical connections to other components; the OEHR is only excited via magnetic coupling.

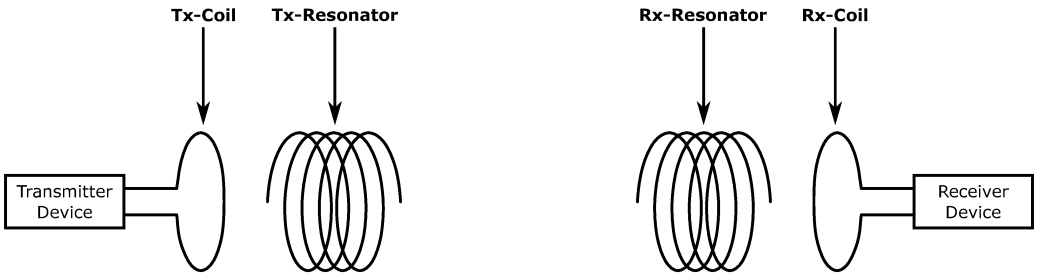


Figure 3.1: Four-coil IPT system with open-ended helical resonators

Contrary to conventional coil resonators, which require a lumped passive element to cancel reactances and lead to resonant behaviour, open-ended helical resonators are self-resonant. This means that the OEHR is used in the frequency in which the helix's distributed self-capacitance resonates with its inductance. This approach is generally applied in MHz frequencies, in which it is easier to achieve self-resonance behaviour.

The advantages of using OEHR in WPT are especially due to its extremely high quality factors, which can reach values up to 900 [29]. Since the resonator is self-resonant, the quality factor is the highest attainable for that particular helix. In other words, if the helix would be used as a regular coil, it would require a lumped capacitor that might have a non-negligible ESR, ultimately causing Q factor reduction when compared to the OEHR self-resonant case. While high Q capacitors for MHz applications are available on the market [36], they can be very costly for capacitance values required in these circumstances. Additionally, it is beneficial to have a self-resonant circuit rather than using lumped capacitors in some WPT applications, since they may suffer damages from voltage or current amplification provided by the resonator [31].

Furthermore, when the OEHR is applied as a resonator in the four-coil IPT topology, the loading effect from source and load resistances is minimized. Consequently, as presented on Sections 2.1.2.2 and 2.1.2.3, a higher quality factor for the resonators signifies an improved $|S_{21}|_{max}$ and an increased WPT

distance, meaning that the OEHR's advantages can improve the overall IPT functioning.

While it is beneficial from the quality factor aspect, not requiring a discrete capacitor in an OEHR means that the electric field is not confined within a lumped component, but permeates all the surroundings of the helical resonator. This may lead to safety issues regarding electric field strength close to the resonators [37].

### 3.1.1 Modelling Approaches for Open-Ended Helical Resonators

One important disadvantage of using open-ended resonators, either in helical shape or in spiral format, is the difficulty to model the complex behaviour of the resonator solely based on its geometry, especially due to the distributed self-capacitances. For instance, it is not uncommon to perform resonator tuning in an iterative process by manually altering its number of turns until the desired resonance frequency has been reached in measurements [27]. For these reasons, it is necessary to understand the different approaches available in literature to analyze these type of circuits.

As largely applied in microwave engineering, the natural candidate to model open-ended resonators is to use distributed circuit analysis in experimental, numerical, and theoretical approaches. Miranda and Pichorim [38], [39] have experimentally shown that helical resonators will have current and voltage distributions depending on the impedances applied to its ends, similar to a distributed transmission line. A high impedance termination causes a maximum voltage and zero current boundary, while a low impedance termination leads to low voltage and maximum current boundary. Breitkreutz and Henke [40] derived a numerical method to calculate the resonance frequency of self-resonant open-ended coils based on the distributed inductances and capacitances between infinitesimal coil segments. Although it is accurate for an individual OEHR, their method is limited by not allowing all possible load terminations for OEHR and by not considering eletric field coupling effects between multiple resonators in WPT. While some theoretical derivations exist

and treat helical coils as one-wire transmission lines, they either rely on infinite coils with boundary conditions not relevant to WPT [41], [42], or depend on assumptions of coils with a large height to diameter ratio to be accurate [39], [43], which is not the case for the compact dimension requirements for WPT applications.

While useful to analyze the behaviour of an individual resonator, distributed circuit analysis becomes very complicated when dealing with mutual inductances [44] and interactions between multiple resonators required in WPT topologies. Several research efforts have shown that lumped models are applied satisfactorily to describe WPT systems [15], [27], [29], [37], [39], even when the resonators present distributed transmission line effects. According to [27], open-ended spiral resonators can be modelled as a discrete $LC$ circuit since it functions by providing energy storage very similarly to a resonant tank with a lumped capacitor and inductor. Kurs *et al* [29] have shown that a numerically equivalent inductance and capacitance can be derived for OEHRs by assuming its current and voltage distribution.

Therefore, even though OEHRs are distributed circuits with behaviour only completely explained by microwave theory and transmission line models, lumped approximations are more useful in WPT, due to simplicity to interpret the interaction between resonators, while still leading to sufficiently accurate results.

## 3.2 WPT Systems using OEHRs

This Section presents a brief introduction to innovative WPT methods existent in the literature that apply OEHRs. Next, the novel capacitively coupled OEHR WPT system is proposed.

### 3.2.1 Review of Existing WPT Methods with OEHRs

Conventional inductive power transfer is only one of many WPT configurations made possible due to the characteristics of open-ended helical resonators. The single conductor power transfer (SCPT) method [45]–[47] takes advantage of

OEHR being regarded as a single-wire transmission line that does not require a ground plane or a second conducting path to support a standing wave. In other words, it uses the open-ended resonator as part of the single current path in order to deliver power without the necessity of two wires, usually through a single metallic structure. This type of system is also denominated using the terms single-contact [37] or ground-eliminated power transfer [48]. In the single conductor approach, the goal is to utilize existing metallic structures as part of the current route in order to extend the possible distance between Tx and Rx, while often applying one or more intermediate stages by means of IPT or CPT. Consequently, SCPT allows innovative power delivery characteristics, such as power transmission without direct line-of-sight and freedom of placement by permitting connection of receivers at any point along the metallic structure. Usually, the metallic structure has to be considerably smaller than $\lambda/4$ to not affect the system's resonant behaviour.

In order to provide a more complete understanding of SCPT, a brief comparison between existing SCPT topologies is necessary [47]. Figure 3.2 depicts common configurations of SCPT systems using OEHR.

The first configuration (Figure 3.2a) [48] comprises a transmitter device, such as a voltage source, having one terminal grounded and the other connected to a Tx-resonator by means of an arbitrary metallic structure. The receiver device is magnetically coupled with the open-ended resonator via the Rx-coil. The metallic structure can be considered part of the resonator, allowing current flow through both when the system operates in resonance. In this topology, there is an increased loading effect, effectively reducing the resonator's quality factor caused by the direct series connection of source, as well as to the metallic structure's additional impedance.

The second topology (Figure 3.2b) [37] employs an individual resonator placed on top of a metallic structure in the form of a capacitive Tx-plate. The standing wave is excited in the OEHR by means of the distributed parasitic capacitance in relation to the Tx-plate. Additionally, the receiver device is directly connected in parallel with a portion of the resonator. This topology provides enhanced freedom of placement, since the resonator-receiver assembly

can be put virtually anywhere on top of the Tx-plate. The resonator's loaded quality factor reduction is even more prominent, due to both of source and load being directly connected to the resonator.

The third topology (Figure 3.2c) [45], [46] fragments the resonator into two parts, with the metallic structure in the middle. Tx-resonator is magnetically coupled to Tx-coil, while Rx-resonator is coupled to Rx-coil, being similar to a four-coil by not causing additional loading effects on the resonators. There is no significant inductive coupling between Tx and Rx, all the power is transmitted via the metallic structure. Actually, Tx-resonator, Rx-resonator, and the metallic structure resonate collectively as a single resonator. A current can be passed through the metallic structure without the need of a second wire, leading to applications using existing conductive shelves or tables in powering distributed sensors, for example.

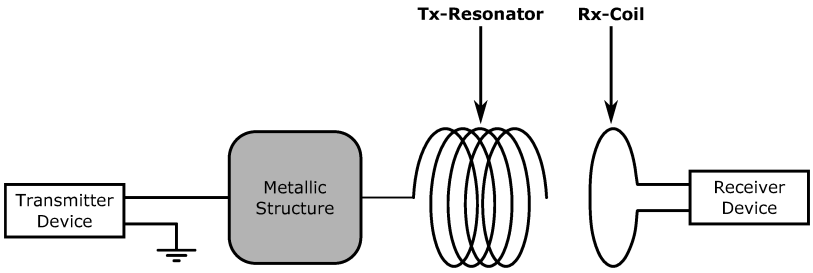


(a)

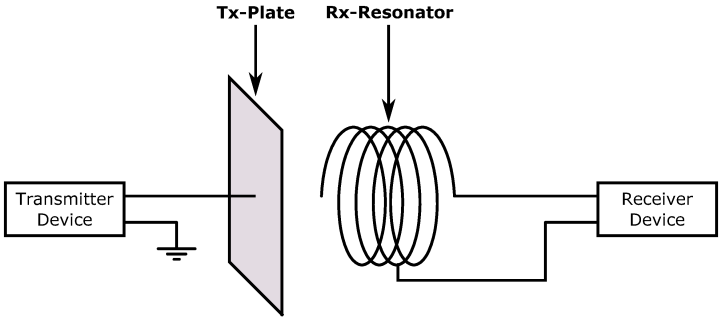


(b)

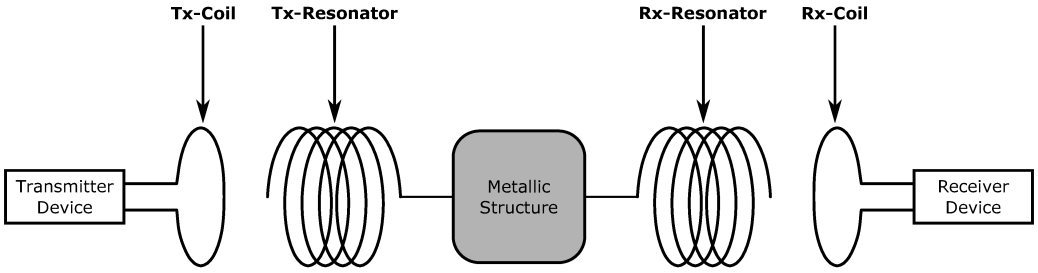


(c)

Figure 3.2: Topologies of power transfer using OEHR: (a) direct feeding, (b) capacitive feeding with direct load connection, and (c) coil-fed resonators.

### 3.2.2 Capacitively Coupled OEHR WPT System

Given the previous description of the advantages of open-ended helical resonators, one objetive of this thesis is to explore innovative uses of OEHRs in wireless power transmission, seeking to combine the best properties of inductive and capacitive coupling systems, but also addressing the common issues of both technologies. For this reason, a new WPT method using capacitively coupled open-ended helical resonators is proposed.

While some initial experimental outcomes for a similar system with square-shaped coils are found in [49], this thesis focuses on a WPT topology constructed with helix-shaped resonators, analyzing it based on a theoretical background to derive a circuit model with lumped elements. Additionally, further understanding is provided by electromagnetic simulations and experimental verifications.

Figure 3.3 displays the system configuration for the proposed WPT system. This topology features a transmitter device connected to a Tx-coil, which is magnetically coupled to a Tx-resonator. This OEHR has one end connected to a Tx-plate, seeking to provide electric field coupling to an Rx-plate, which is also connected to a resonator. The receiver device is symmetric and analogous to the transmitter. Therefore, this system combines inductive coupling between coils and resonators, capacitive coupling between plates, and single conductor properties as a return current path is absent due to the use of OEHRs.

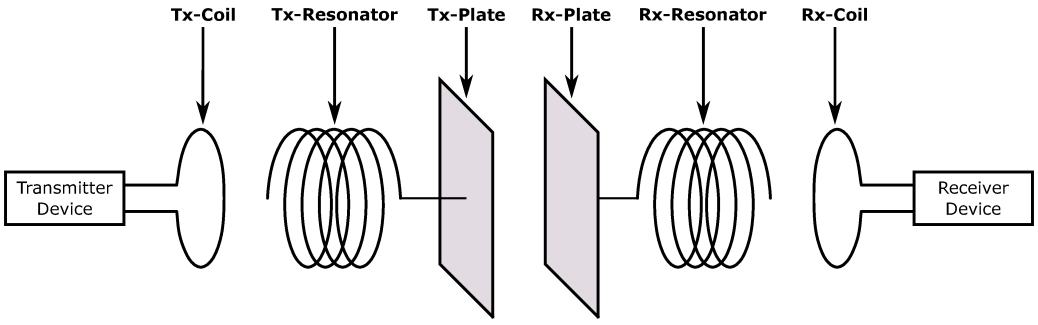


Figure 3.3: WPT system using capacitively coupled open-ended helical resonators

In regular applications, such as conventional IPT, resonators are only coupled using magnetic fields. Therefore, each end of the open-ended resonator has an open-boundary condition, having zero current and maximum voltage at the open-ends. In the proposed system, however, one end is treated normally since its open, but the other end is attached to a plate which couples to another plate in the receiver resonator. This means that the forward capacitor ($C_f$) formed by the capacitive plates generates a low impedance current path between resonators. As a result, the overall combination of Tx-resonator, Tx-plate, Rx-plate, and Rx-resonator can be viewed as a single resonating structure. Therefore, power transfer will occur when a combined resonance of this structure is achieved, particularly by considering the current path being closed by a parasitic return capacitance ($C_r$) between Tx-resonator and Rx-resonator.

The novelties and advantages of this approach compared to conventional WPT configurations are summarized as follows:

1. **Alignment:** instead of two pairs of coupling plates as in regular CPT, only one pair of plates exists. Therefore, optimal transmission requires the alignment of one transmitting element with one receiving element, as in IPT. However, it benefits from the resistance to misalignment provided by CPT, but not requiring strict positioning caused by IPT's low tolerance of lateral changes in distance, which is usually the case for wireless phone chargers.

   Consequently, this novel approach can be used to improve freedom of positioning in wireless charging to portable electronic devices. For instance, the transmitter module can be installed in countertops or tables, where receiver can be part of an electronic device to be charged.

2. **Resonator construction:** WPT properties are usually restricted by losses on the resonators. By using open-ended helical resonators, which are known to have one of the highest quality factors for electrical resonators constructed with wires [29], the capabilities of the wireless power transmission topology can be significantly improved.

3. **Resonator feeding:** instead of coupling energy by direct connection to the resonators [50], coil feeding techniques to the OEHR are applied, similarly to a four-coil IPT system. Thus, this approach diminishes loading effect on resonators, maximizing their Q factors.

4. **Voltage:** regular capacitive power transfer usually benefit from high voltages operation, presenting lower losses. Since an OEHR acts as a voltage step-up transformer [50], this arrangement can be helpful in the plate to plate coupling.

### 3.2.3 Lumped Element Equivalent Circuit Model

In electrical engineering, equivalent circuit models are a common method that can provide a simple procedure to understand a complex electric system. Based on the discussion in Section 3.1.1, a lumped element can be used to derive an equivalent circuit model for the proposed WPT system.

Figure 3.4 displays the circuit model for the single conductor WPT system with open-ended helical resonators. $L_2$ and $L_3$ represent the inductances of each these elements, along with their respective ESRs $R_2$ and $R_3$. The coils $L_1$ and $L_2$ are used to perform magnetic coupling to resonators via $k_{12}$ and $k_{34}$. The capacitance $C_f$ corresponds to the parallel plate capacitance responsible for the coupling between transmitter and receiver, while $C_r$ is the parasitic capacitance that closes the resonators' current loop.

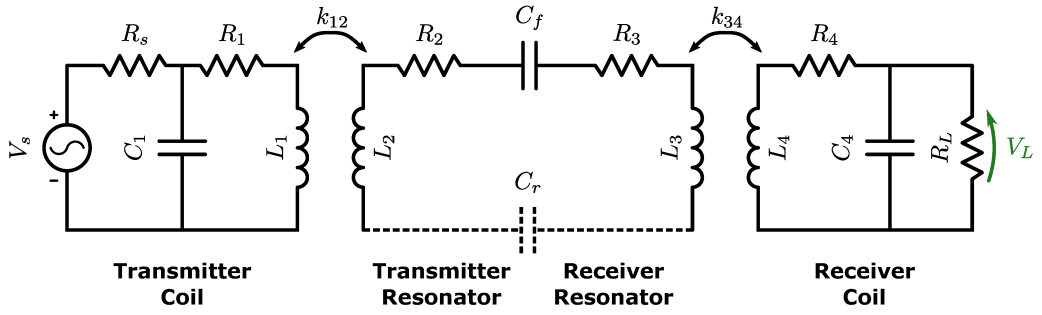


Figure 3.4: Circuit model for capacitively coupled OEHR WPT topology

Unlike circuit models presented in Chapter 2 that were configured with series compensation capacitors, this circuit employs capacitors $C_1$ and $C_4$ to

form parallel resonances with the respective coils. From a lumped circuit perspective, the differences are minimal. However, it is an important aspect when considering the distributed transmission line effects of the resonators.

The coils are positioned near the open ends of the OEHR. As discussed in [38], these are high-voltage and zero current nodes that result in high impedance points in the helix. Therefore, it was experimentally found that the low impedance provided by the coil's series resonance is not suitable to drive the high impedance imposed by the resonator at the feeding points. For this reason, parallel compensation capacitors are required in the coils for higher efficiency in this circuit.

Following the procedure of Chapter 2, the circuit model is used to evaluate WPT topology. While Equation (3.1) describes $\frac{V_L}{V_S}$, Equations (3.2) and (3.3) are used to find the system's $S_{21}$.

$$\frac{V_L}{V_S} = \frac{-\omega^2 X_{C_1} X_{C_4} k_{12} k_{34} \sqrt{L_1 L_2 L_3 L_4} R_L}{(R_S + X_{C_1})(R_L + X_{C_4})(Z_1 Z_2 Z_3 + \omega^2 Z_1 k_{34}^2 L_3 L_4 + \omega^2 Z_3 k_{12}^2 L_1 L_2)} \tag{3.1}$$

$$S_{21} = \frac{-2\omega^2 X_{C_1} X_{C_4} k_{12} k_{34} \sqrt{L_1 L_2 L_3 L_4} \sqrt{R_S R_L}}{(R_S + X_{C_1})(R_L + X_{C_4})(Z_1 Z_2 Z_3 + \omega^2 Z_1 k_{34}^2 L_3 L_4 + \omega^2 Z_3 k_{12}^2 L_1 L_2)} \tag{3.2}$$

$$\begin{cases} Z_1 = R_1 + j\omega L_1 + X_{C_1} - \dfrac{X_{C_1}^2}{R_S + X_{C_1}} \\ Z_2 = R_2 + R_3 + j\omega L_2 + j\omega L_3 - \dfrac{j}{\omega C_f} - \dfrac{j}{\omega C_r} \\ Z_3 = R_4 + j\omega L_4 + \dfrac{X_{C_4} R_L}{X_{C_4} + R_L} \\ X_{C_1} = -\dfrac{j}{\omega C_1} \\ X_{C_4} = -\dfrac{j}{\omega C_4} \end{cases} \tag{3.3}$$

In Section 3.5, the derived equations will be used to compare the circuit model with measurement and simulation results.

## 3.3 Measurement and Simulation Setup

Figure 3.5 displays the experimental setup used to evaluate the proposed wireless power transfer system. Transmitter and receiver are symmetric.

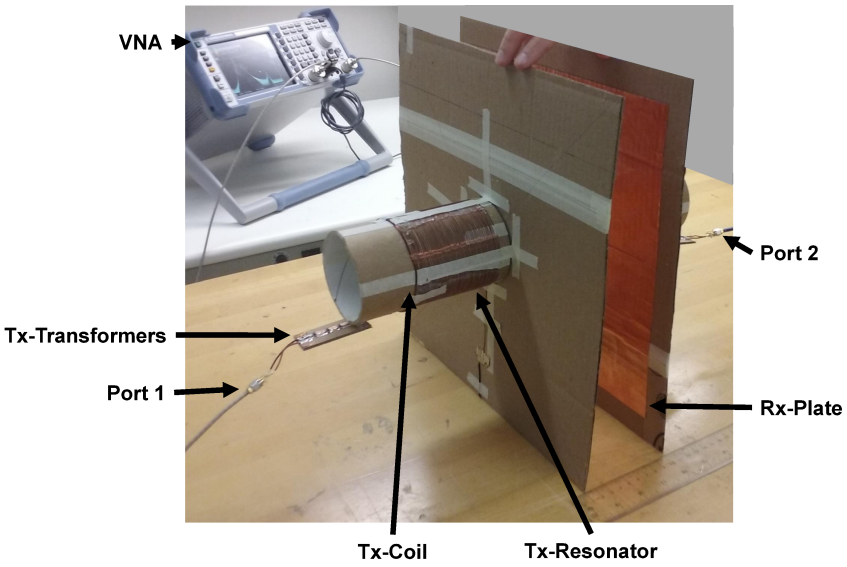


(a)

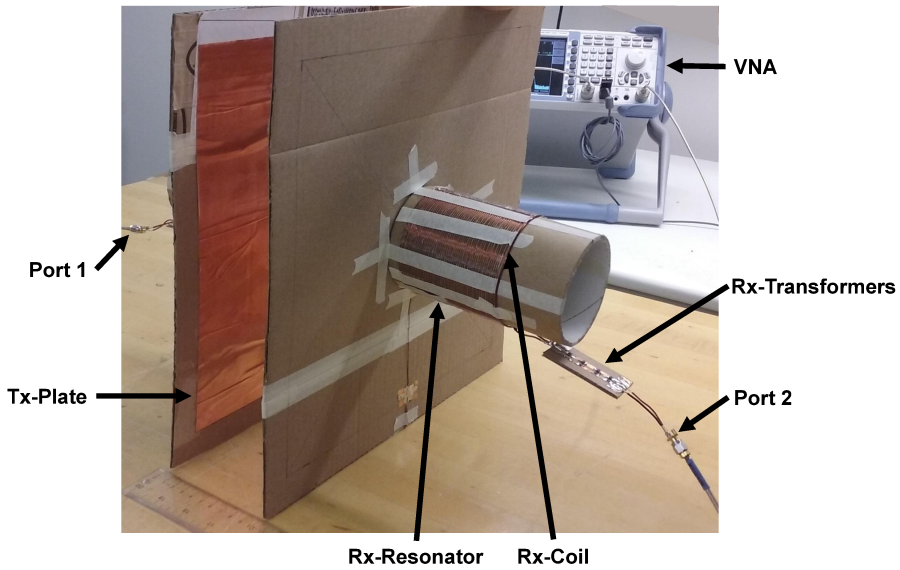


(b)

Figure 3.5: Experimental setup: (a) transmitter, and (b) receiver.

Experimental verification is done by measuring 2-port scattering parameters with a Rohde and Schwarz ZVL13 VNA, calibrated using a SOLT (short-open-load-thru) method. Simulations are made using finite element method

with Ansys HFSS 2018 electromagnetic simulator.

The analyzed structure can be very computationally intensive for finite element simulations, particularly due to its three-dimensional geometry and numerous circular turns using a wire with round cross section, which can lead to a complex and time-consuming FEM meshing and solving process. For these reasons, each turn was modelled with an octagonal shape using a conductor with square cross section. These simplifications were made in order to greatly simplify the simulation and the number of mesh elements required to represent the system, without significantly altering the system's characteristics.

Figure 3.6 displays the simulation setup, indicating the most important dimensions of the system. Note the use of octagonal coils using wires with square cross sections. Table 3.1 describes dimensions and parameters used both in experimental and measurement setup. All conductors (wires and plates) are made of copper.

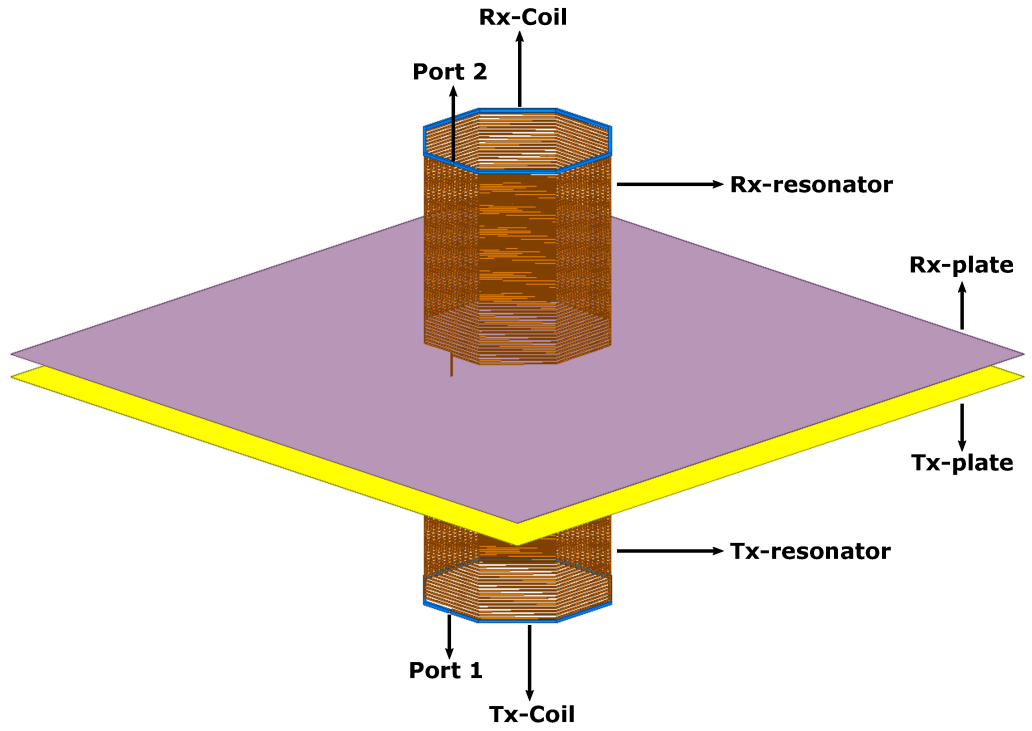


(a)

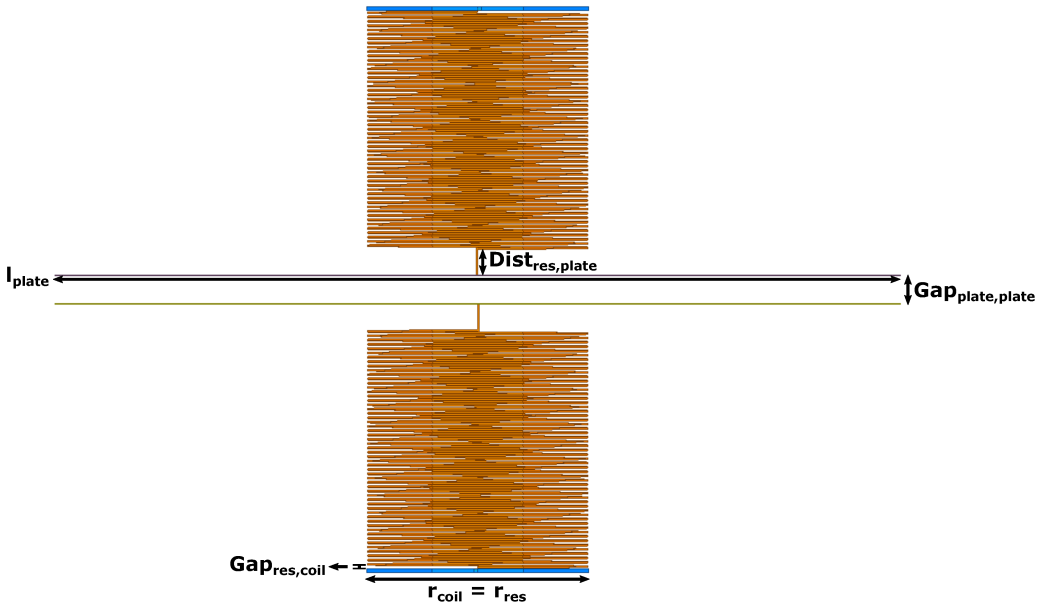


(b)

Figure 3.6: Images of simulation setup: (a) isometric view and (b) front view

Table 3.1: Dimensions for experimental and simulation setup

| Parameter | Description | Value |
|---|---|---|
| $N_{res}$ | Resonators' number of turns | 55 |
| $r_{res}$ | Resonators' helix radius | 42 mm |
| $a_{res}$ | Radius of resonators' wire | 0.51 mm (24 AWG) |
| $p_{res}$ | Pitch between resonators' turns | 1.51 mm |
| $r_{coil}$ | Coils' radius | 42 mm |
| $a_{coil}$ | Radius of coils' wire | 1.29 mm (16 AWG) |
| $l_{plate}$ | Side length of square metallic plates | 30 cm |
| $t_{plate}$ | Thickness of metallic plates | 90 $\mu$m |
| $Gap_{plate,plate}$ | Parallel plate gap | 10 mm |
| $Dist_{res,plate}$ | Distance between resonator and plate | 10 mm |
| $Dist_{res,coil}$ | Distance between resonator and coil | 1 mm |
| $Disp_{Tx,Rx}$ | Lateral displacement of Rx | 0 cm |

### 3.3.1 Transformers in Measurement Setup

As seen in Figure 3.5, transformers are included in the measurement setup between the port 1 and Tx-Coil, as well as between port 2 and Rx-Coil. This section explains the reasons for their inclusion during the measurement process.

Open-ended coils operate as ground eliminated structures [48]. The open ends have zero-current boundary conditions, resulting in maximum voltage points. Consequently, their electric field distribution surrounds the resonator, which may lead to slight performance degradation in inductive coupling systems, particularly by unwanted coupling with VNA equipment and cables during measurements [51].

However, in the proposed system the electric field is the main coupling mechanism, with the forward capacitance being higher than the return capacitance. In this case, the current path via electric field coupling through the common ground of the VNA's coaxial cables offers much lower impedance than the intended return coupling path. As a result, it was experimentally verified that VNA measurements usually showed better transmission characteristics,

having a spurious resonance profile and not matching the simulations.

This is similar to measurements with electrically small antennas, such as monopoles. Since their ground planes are small, any coaxial cable attached to it may have currents induced in the outer conductor, functioning as an extension of the ground area and significantly affecting the measurements in a way that does not represent the actual antenna [52]–[54].

In this thesis, transformers are added to each port in the measurement setup to supress current in the VNA's coaxial cables as proposed by [53], [54]. Four cascaded 1:1 RF transformers added to each port were required to sufficiently reduce these effects and to provide a good match between simulation and measurements. The influence of the added transformers (MABAES0060 made by Macom) are removed via 2-port network de-embedding process. It is important to emphasize that this procedure is only necessary due to the common ground of both VNA ports and it is not the usual case for an actual WPT application, in which the device being charged has no common electrical ground with the transmitter.

## 3.4 Theoretical Calculation of Circuit Model's Parameters

In order to evaluate the lumped circuit model derived in Section 3.2.3, it is necessary to derive the values for the passive elements from the dimensions considered in Table 3.1.

The inductance of the coil follows the formula of inductance for a circular ring [55]:

$$L_1 = L_4 = \mu_0 r_{coil} ln\left(\frac{16 r_{coil}}{a_{coil}} - 2\right) \tag{3.4}$$

where $\mu_0 = 4\pi \times 10^{-7}$ H/m is the permeability of free space.

The inductance of the helical resonator can be found by the formula of inductance for solenoids [56], with all dimensions in inches:

$$L_2 = L_3 = \frac{r_{res}^2 N_{res}^2 p_{res}^2}{9 r_{res} + 10 N_{res} p_{res}} \mu H \tag{3.5}$$

In order to find the values for coil-resonator magnetic coupling coefficients, it is necessary to calculate the mutual inductance between the coil loop and each individual turn of the resonator. The mutual coupling between two coaxial wire loops, the first loop consisting of the coil and the second loop being a single turn of the resonator, separated by a distance $d$ is [28]:

$$M = \frac{2\mu_0 r_{coil} r_{res}}{m}\left[\left(1 - \frac{m^2}{2}\right)K(m) - E(m)\right] \tag{3.6}$$

where $m = \sqrt{\frac{4\mu_0 r_{coil} r_{res}}{(r_{coil}+r_{res})^2+d^2}}$, and $K(m)$ and $E(m)$ are the elliptic integrals of the first and second kind, respectively [28]. By considering each turn of the resonator as an independent loop, the magnetic coupling coefficients $k_{12} = k_{34}$ are equal to $M_{total}/\sqrt{L_{coil}L_{res}}$, where $M_{total}$ is the sum of mutual inductances between the coil loop and each turn of the resonator found using (3.6). Therefore:

$$M_{total} = \sum_{i=1}^{N_{res}} M_{coil,i_{th}resonatorturn} \tag{3.7}$$

Even though the method of finding the magnetic coupling factor described above is accurate for lumped coils, it is not completely valid for helical resonators because of their non-uniform current distribution [44]. For this reason, the actual $M_{total}$ is smaller in order to account for the transmission line effects in the coil [44] and a correction factor of 0.5 was applied to the value found using Equation (3.7), which ultimately resulted in good agreement with measurements and EM simulations.

The lumped capacitors $C_1$ and $C_4$ are designed to resonate with $L_1$ and $L_4$ at $f_0$. Consequently:

$$C_1 = C_4 = \frac{1}{\omega_0^2 L_1} = \frac{1}{\omega_0^2 L_4} \tag{3.8}$$

The parallel plate capacitance $C_f$, including edge effects due to fringing fields, can be calculated as [57]:

$$C_f = \left[1 + 2.343\left(\frac{Gap_{plate,plate}}{l_{plate}}\right)^{0.891}\right]\frac{\varepsilon_0 l_{plate}^2}{Gap_{plate,plate}} \tag{3.9}$$

where $\varepsilon_0 = 8.85 \times 10^{-12}$ F/m is the permittivity of free space.

At resonance, the imaginary part of $Z_2$ in Equations (3.2) and (3.3) is cancelled, since the reactive inductance of the resonators compensates the capacitive reactance, such that $j\omega_0 L_2 + j\omega_0 L_3 - \frac{j}{\omega_0 C_f} - \frac{j}{\omega_0 C_r} = 0$. Since all the other parameters can be derived analytically, the remaining parameter $C_r$ can be found by:

$$C_r = \frac{C_f}{\omega_0^2 C_f (L_2 + L_3) - 1} \tag{3.10}$$

Using equations (3.4) to (3.10), the equivalent lumped components can be calculated from the dimensions of Table 3.1. Table 3.2 displays the obtained values. $R_1$ to $R_4$ are obtained from standard equations of high-frequency resistance calculation, taking into account skin depth [58] and proximity effects [59].

Table 3.2: Components calculated for lumped equivalent circuit model

| **Component** | **Value** |
|---|---|
| $L_1 = L_4$ | 329.961 nH |
| $C_1 = C_4$ | 1680 pF |
| $L_2 = L_3$ | 173.836 $\mu$H |
| $C_f$ | 88.662 pF |
| $C_r$ | 1.614 pF |
| $R_1 = R_4$ | 45.123 m$\Omega$ |
| $R_2 = R_3$ | 9.444 $\Omega$ |
| $R_S = R_L$ | 50 $\Omega$ |
| $k_{12} = k_{34}$ | 0.133 |
| $f_0$ | 6.78 MHz |

## 3.5 Results

Following the dimensions and parameters listed in Table 3.1, the system's S-parameters are measured using a VNA. Electromagnetic simulations are performed under the same conditions to verify the measurements. Additionally,

the theoretically predicted $S_{21}$ that is calculated from the lumped circuit model is also shown for comparison purposes, considering the values presented in Table 3.2. Figure 3.7 displays the measured, simulated, and calculated results.

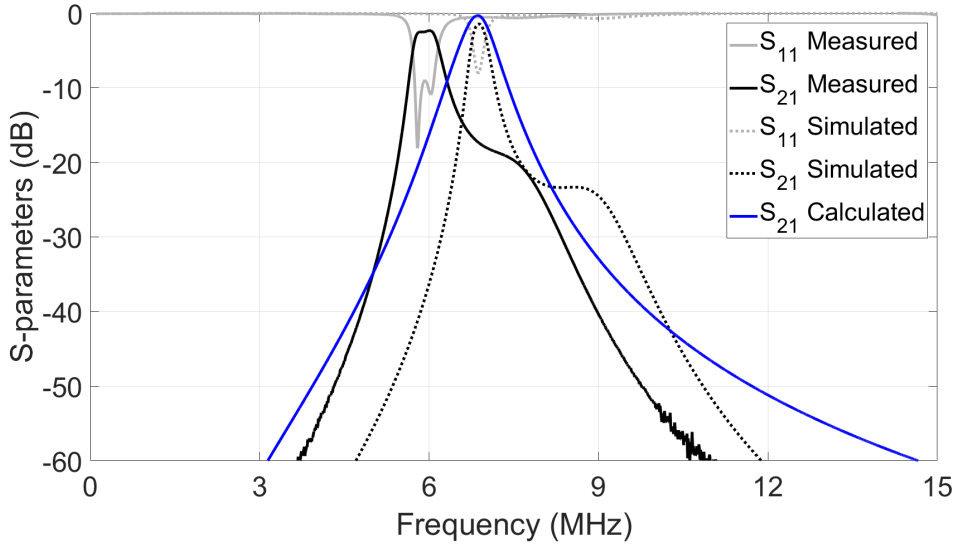


Figure 3.7: Measured, simulated, and calculated S-parameters for the proposed system with parameters listed in Table 3.1

For the simulations, peak transmission $|S_{21}|$ = -1.42 dB occurs at 6.88 MHz, with a corresponding $|S_{11}|$ = -8.013 dB. For the measurements, a first peak transmission $|S_{21}|$ = -2.61 dB occurs at 5.80 MHz and a second peak $|S_{21}|$ = -2.32 dB at 6.01 MHz, with $|S_{11}|$ = -18.1 dB and $|S_{11}|$ = -10.93 dB respectively. For the calculations based on the lumped model, the peak of $|S_{21}|$ happens at 6.86 MHz with a value of -0.2877 dB.

In general, there is good agreement between all the data. The measurement scenario presents some small discrepancies, showing a slightly lower peak than the other results, shifted towards lower frequencies. On the other hand, the lumped model had a higher peak than simulation and measurements. This can be explained because of approximations and assumptions made in the establishment of the circuit model. For example, factors not considered are: the conduction losses in capacitive plates, the eddy current losses caused by magnetic fields from coils/resonators reaching the plates, and the limited quality factors of lumped capacitors.

In order to understand the system's behaviour, parametric analysis are

done by altering one parameter at each time, while maintaining the remaining parameters listed in Table 3.1 constant. These results are shown in the subsequent Sections.

Finally, some reasons for discrepancies between measurement and simulation results are listed in Section 3.5.4.

### 3.5.1 Distance

The first parametric analysis comprises the variation from parallel plate gap ($Gap_{plate,plate}$), as shown in Figure 3.8, to understand how the power is affected by this distance. Measurements were taken from gaps starting at 1 cm up to 20 cm, with 1 cm steps.

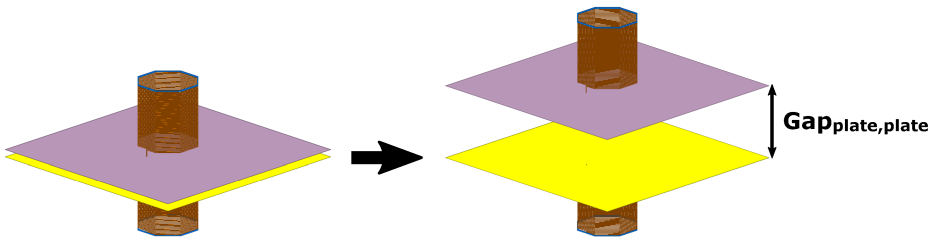


Figure 3.8: Increasing distance ($Gap_{plate,plate}$) between transmitter and receiver devices

Figures 3.9, 3.10, and 3.11 display simulated and measured $|S_{21}|$ for increasing distances between transmitter and receiver.

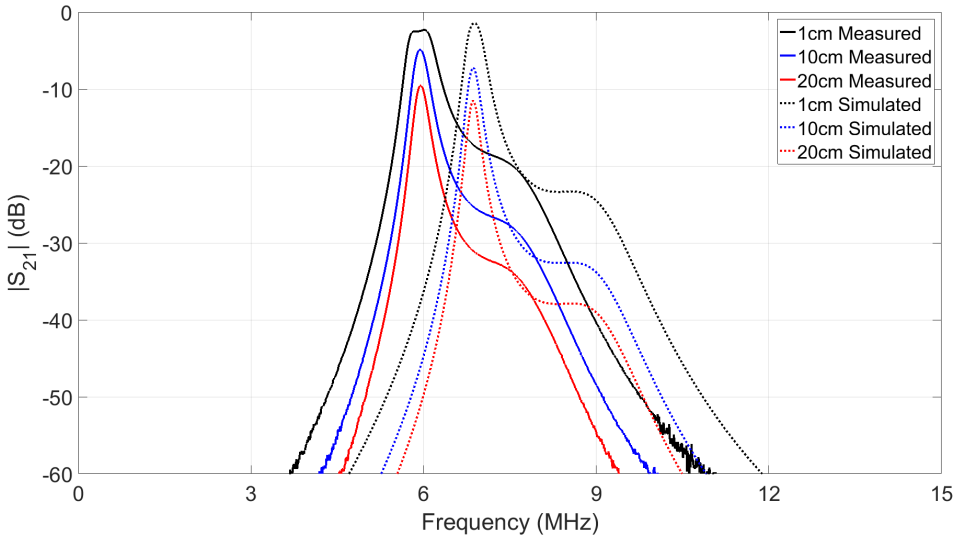


Figure 3.9: 2-D plot of $|S_{21}|$ for selected distances for proposed system

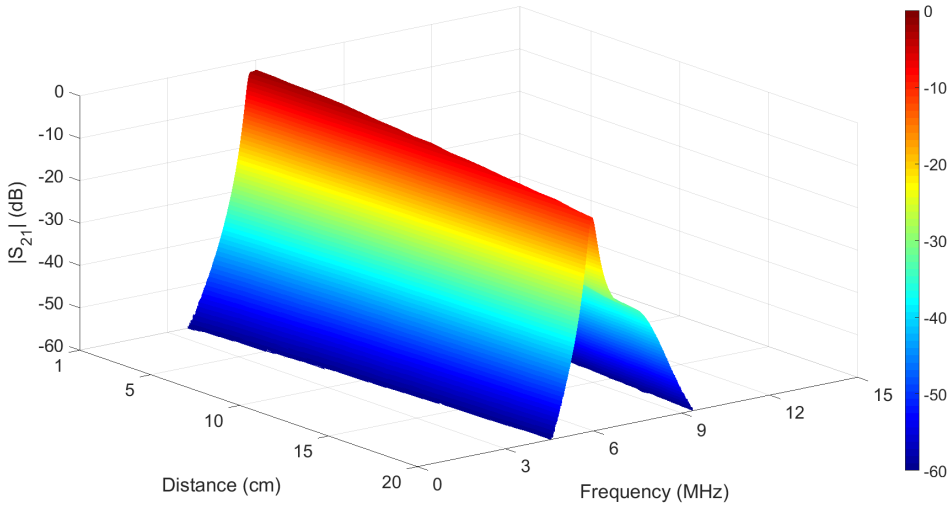


Figure 3.10: 3-D plot of measured $|S_{21}|$ as a function of distance for proposed system

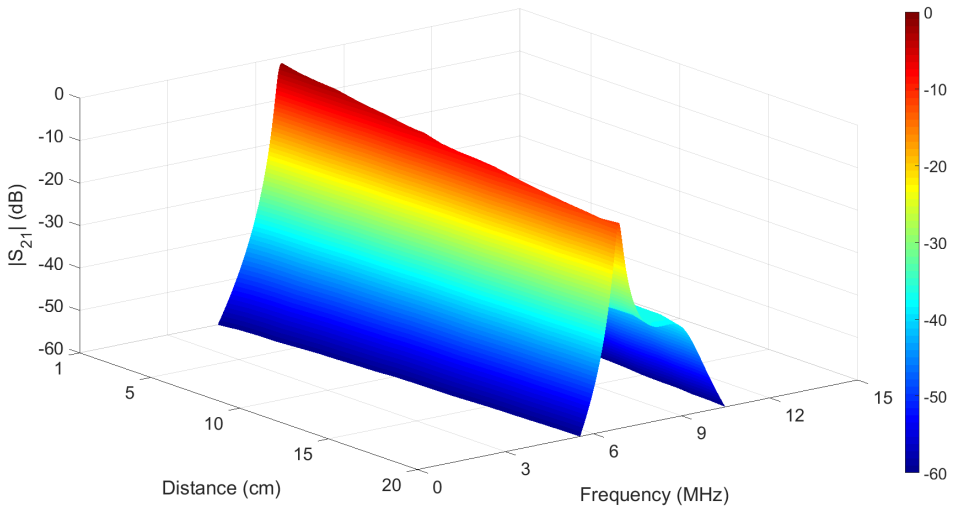


Figure 3.11: 3-D plot of simulated $|S_{21}|$ as a function of distance for proposed system

Figures 3.12 and 3.13 display the changes of $|S_{21}|_{max}$ and $f_{max}$ as the distance increases.

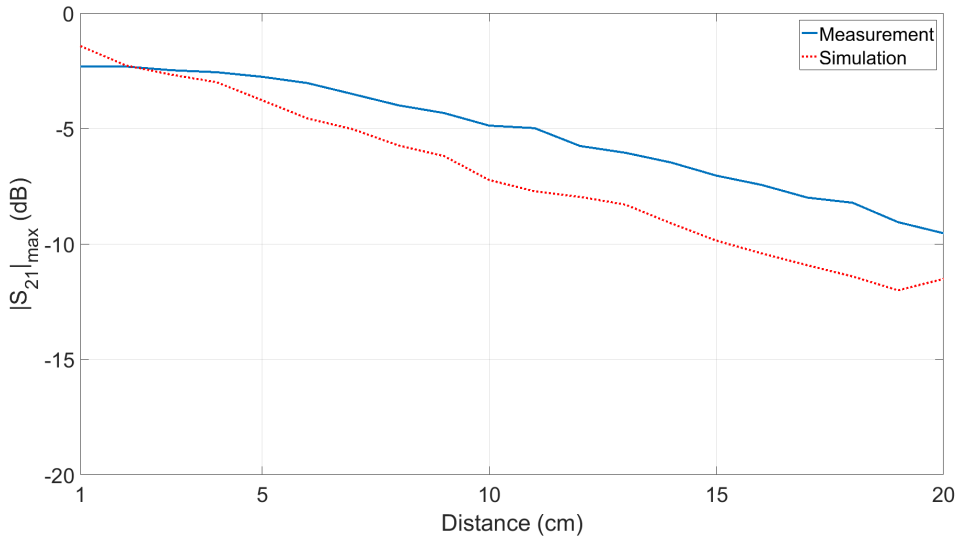


Figure 3.12: $|S_{21}|_{max}$ as a function of distance for proposed system

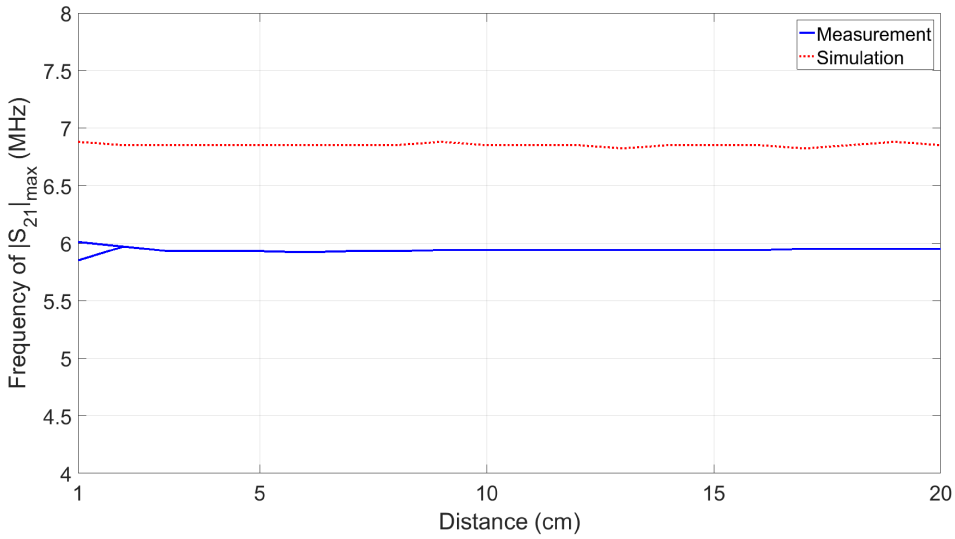


Figure 3.13: $f_{max}$ as a function of distance for proposed system

Despite a small frequency splitting in measurements for distances of 1 cm and 2 cm, the power transfer frequency is independent of distance. Additionally, the decay of power transmission with distance is very small, more similar to the behaviour of CPT rather than the sharp decrease of IPT below the critical coupling point.

### 3.5.2 Lateral Misalignment

Next, it is necessary to analyze the impact when lateral misalignment is introduced by increasing $Disp_{Tx,Rx}$, as shown in Figure 3.14, while keeping the original $Gap_{plate,plate}$ of 1 cm. The lateral displacement $Disp_{Tx,Rx}$ between transmitter and receiver is varied between 0 cm (perfect alignment) and 30 cm (no overlap between Tx and Rx), with 2 cm intervals.

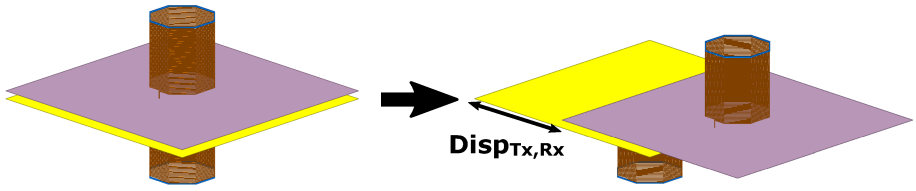


Figure 3.14: Increasing lateral displacement ($Disp_{Tx,Rx}$) between transmitter and receiver devices

The simulated and measured $|S_{21}|$ for increasing lateral misalignment between transmitter and receiver are shown in Figures 3.15, 3.16, and 3.17.

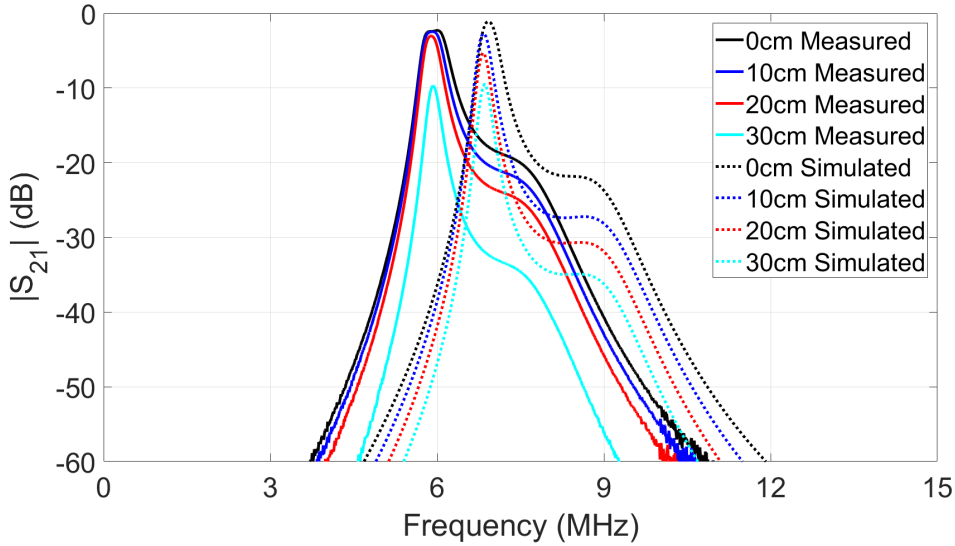


Figure 3.15: 2-D plot of $|S_{21}|$ for selected lateral misalignments for proposed system

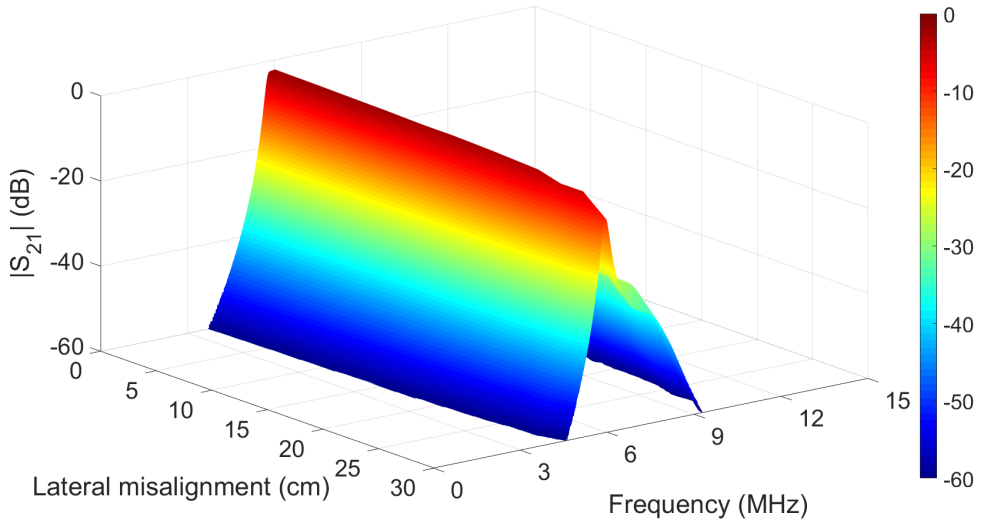


Figure 3.16: 3-D plot of measured $|S_{21}|$ as a function of lateral misalignment for proposed system

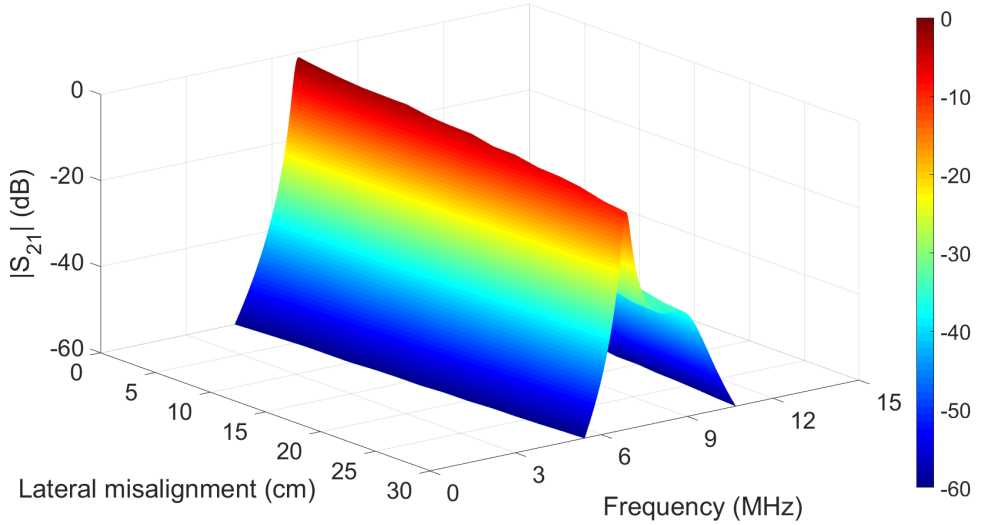


Figure 3.17: 3-D plot of simulated $|S_{21}|$ as a function of lateral misalignment for proposed system

Figures 3.18 and 3.19 exhibit the impact of misalignment on $|S_{21}|_{max}$ and $f_{max}$.

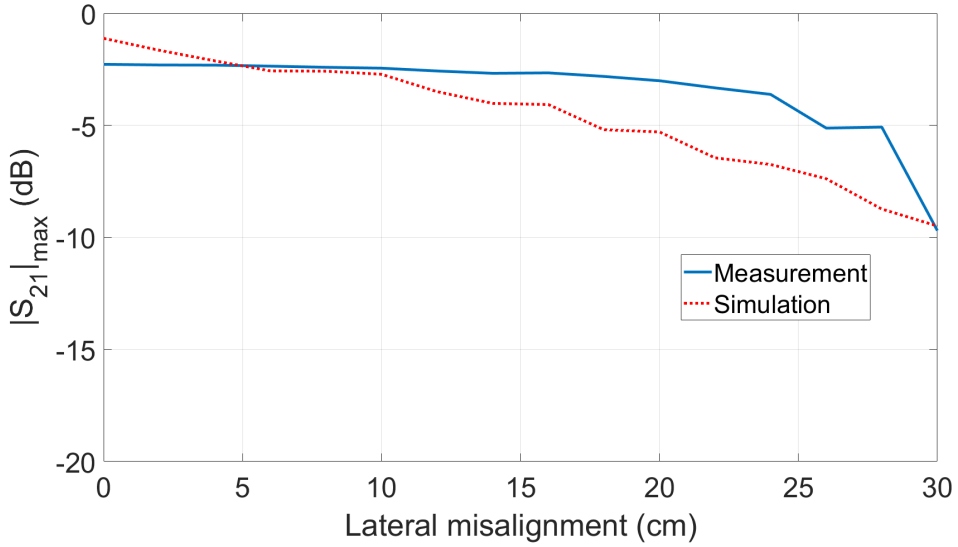


Figure 3.18: $|S_{21}|_{max}$ as a function of lateral misalignment for proposed system

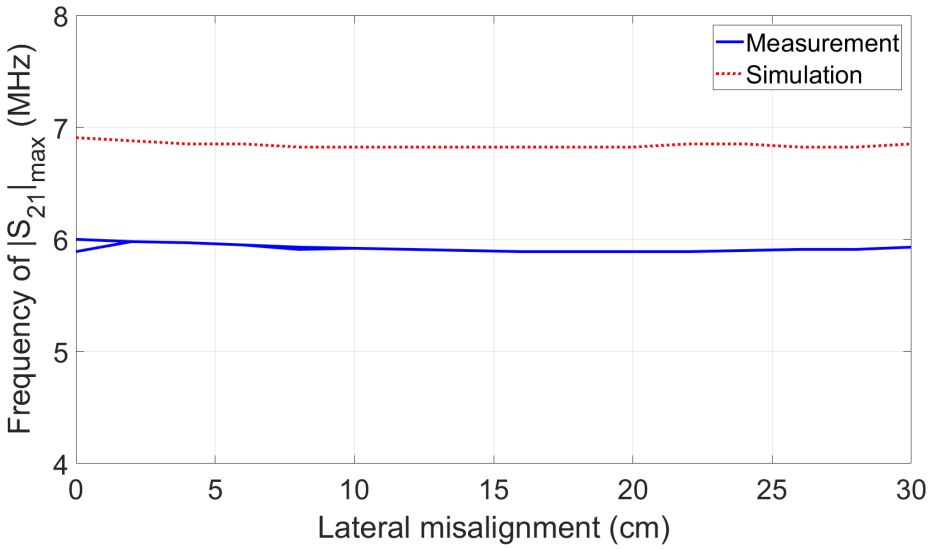


Figure 3.19: $f_{max}$ as a function of lateral misalignment for proposed system

The changes in the alignment show that the resonance frequency is not altered, confirming the robustness of the system regarding this parameter. The highest transmission occurs for perfect alignment, but the impact of misalignment on $|S_{21}|_{max}$ was more pronounced in the simulations than measurements.

Nevertheless, this topology can be considered with good misalignment tolerance due to the minimized transmission degradation for small to moderate lateral offsets.

### 3.5.3 Resonator-Plate Spacing

Finally, this section studies the effect of altering the spacing between resonator and plate ($Dist_{res,plate}$), as depicted in Figure 3.20. Comparisons are made for $Dist_{res,plate}$ values of 1 cm, 2 cm, and 3 cm.

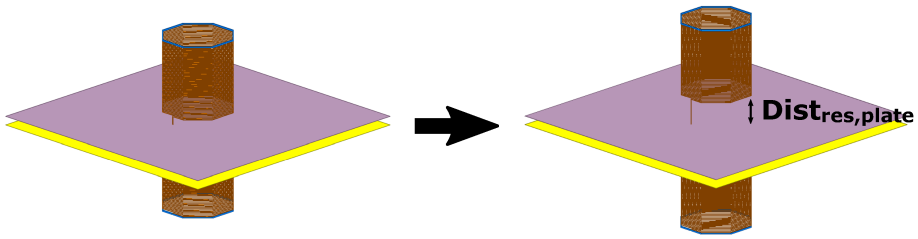


Figure 3.20: Increasing distance ($Dist_{res,plate}$) between resonators and plates

Figure 3.21 shows the simulation and experimental results for varying the resonator-plate spacing.

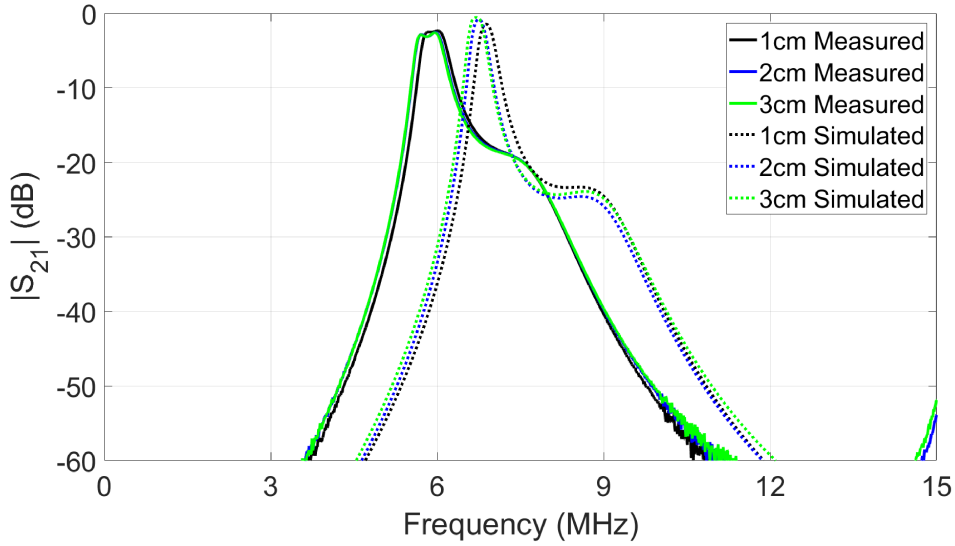


Figure 3.21: 2-D plot of $|S_{21}|$ for selected resonator-plate distances for proposed system

The results show that there are changes when $Dist_{res,plate}$ is varied, implying that eddy current losses due to proximity of resonator and plates exist,

but they are minor and not impactful.

### 3.5.4 Discrepancies between Measurement and Simulation

Several reasons can be listed to explain the minimal discrepancies observed between measurement and simulation results:

- **Tolerance of lumped capacitors:** high quality AVX RF/Microwave capacitors were employed, which have high quality factor in MHz frequencies, but present tolerances of $\pm 10$ % in capacitance related to their nominal value.
- **Fabrication:** hand wound coils result in fabrication differences, especially in possibly uneven pitch between turns.
- **Measurement setup:** while it was tried to minimize these effects, the interaction of OEHRs with close metallic and dielectric structures can have some effect in resonance, causing frequency shift.
- **Simplifications in simulations:** caused by use of octagonal coils with square cross section conductors in the electromagnetic simulations. Simplifications can be justified as this thesis analyzes over 40 different configuration of parametric sweeps, besides the iterative optimization necessary in the overall system design process. Using a dedicated simulation server takes an average of 3 to 4 hours to simulate each variation. Therefore, a simulated structure more similar to the real system could multiply the mesh complexity by a considerable amount, easily leading to additional hundreds of hours in simulations.

It is important to emphasize that it was not the objective of this thesis to provide 100 % accuracy between simulation and measurement results, but to provide a supporting argument to verify that the measurements have similar characteristics with the simulations. Nevertheless, reasonable matching results were found.

## 3.6 Electric and Magnetic Fields in the Proposed System

The electromagnetic simulations provide insightful information about the system with the plots of electric and magnetic field vectors, as presented in Figure 3.22.

The direction of **E** between the plates confirms that it provides the forward coupling path, while the return capacitance in the opposite direction is provided by the **E** coupling between Rx-resonator to Tx-resonator. Some electric field coupling exists between resonators and plates, but it does not contribute directly to the power transfer, but mostly to losses and small frequency shifts. Because of this, this additional capacitance was not considered in the circuit model to simplify the analysis.

**H** is responsible for coupling between coil and resonator. As seen from the image, direct magnetic coupling from transmitter and receiver is almost non-existent.

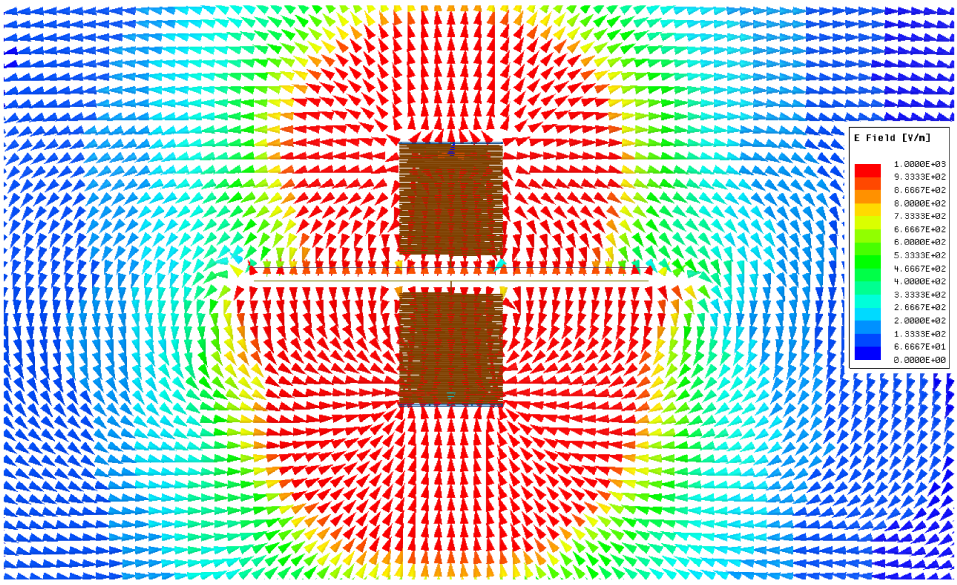


(a)

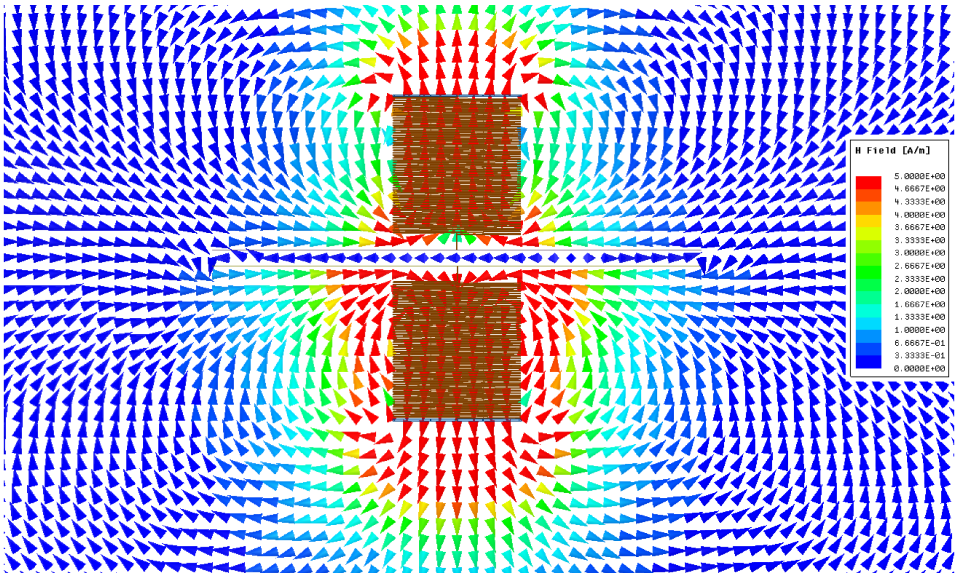


(b)

Figure 3.22: Electromagnetic field simulation: (a) electric field vector and (b) magnetic field vector.

### 3.6.1 Field Strength and Safety

According to the Limits of Human Exposure to Radiofrequency Electromagnetic Energy [60] established by Health Canada, the maximum exposure limits for uncontrolled environments are 83 V/m for electric field and 90 A/m for magnetic field strength for frequencies below 10 MHz. While Figure 3.22 focused on showing the vector direction to provide an understanding of the system, the field magnitude suggests that the electric field strength can exceed safety limits in some regions of space. On the other hand, magnetic field strength lies well below the regulated maximum values.

To clarify, Figure 3.23 displays the electric field magnitude for 1 W input power, considering safety limits. It shows that electric field strength is exceeded in the red area.

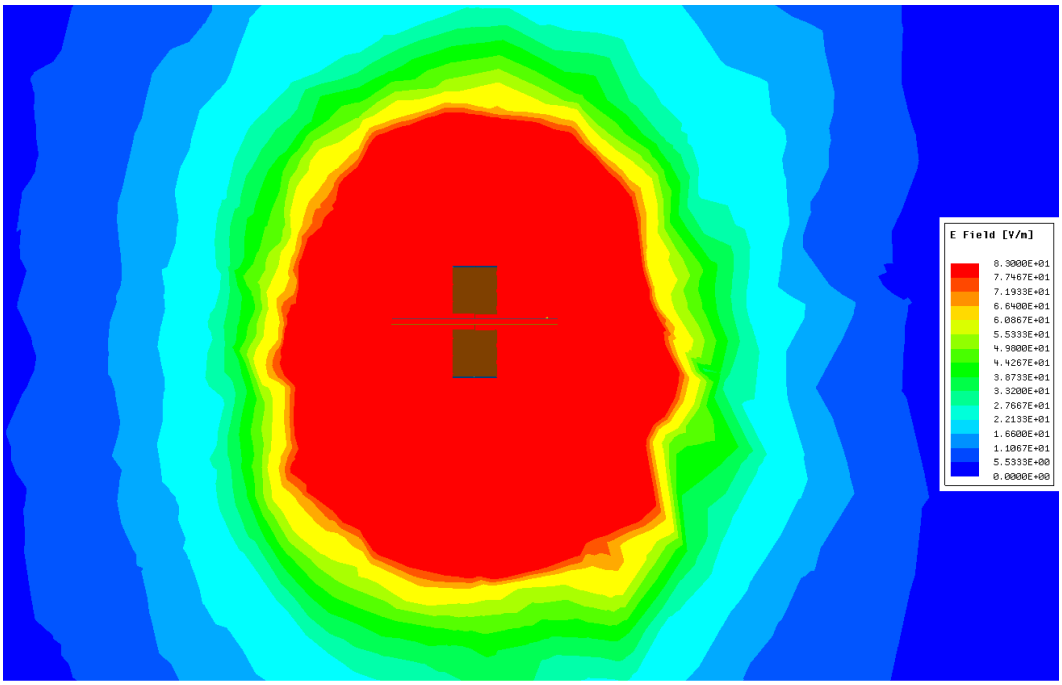


Figure 3.23: Electric field for an 1 W input power and considering Health Canada's safety limits. Areas in red exceed the standard

These results indicate that the current system is more suitable for lower power applications, in the range of hundreds of mW. For increased power levels, further research is needed to provide electric field reduction or mitigation by shielding techniques in order to follow regulations.

## 3.7 Chapter Summary

This chapter focused on the theory and WPT applications of open-ended helical resonators.

First, distributed and lumped modelling approaches were discussed for OEHRs. Distributed circuit analysis is more accurate and more useful to understand an individual resonator, whereas in lumped models it is easier to account for the interaction between the multiple circuits used in WPT.

After a brief description of existing WPT methods using OEHRs, a novel wireless power transmission topology using capacitively coupled open-ended helical resonators is proposed. This system is constructed and verified by measurements, electromagnetic simulations, and equivalent lumped circuit analy-

sis. Some minimal discrepancies between experimental and simulated results were seen, but the overall trends show high efficiency, independence of optimal working frequency regarding changes in configuration, and good tolerance to distance and misalignment. Considerations about measurement procedures, simplification of simulation setup, and electromagnetic field analysis were also made.

Therefore, the proposed WPT topology can be considered an improved alternative to conventional IPT and CPT systems, especially considering its robustness to lateral offsets, while only requiring the alignment of one transmitting element with one receiving element for optimal transmission.

# Chapter 4

# Capacitive Power Transfer System with Inductively Compensated Class E Resonant Full-Wave Rectifier

As described in the introduction chapter, rectifiers are important modules in the overall WPT system. Since the electromagnetic power has already reached the receiver via wireless power transfer, it must be efficiently converted to dc.

This chapter presents a brief introduction to rectifiers in WPT applications and the problems faced when operating in the MHz range. Next, a capacitive power transfer system operating in 6.78 MHz is proposed for the highly efficient Class E full-wave rectifier topology, including a procedure for designing the required compensation circuits.

## 4.1 Rectifiers in Wireless Power Transfer

Generally, most wireless power transfer mechanisms benefit from high frequency operation, whereas the remaining circuit modules may have their performance reduced in higher frequencies. This is the case for the ac-dc converters, as conventional rectifiers designed for lower frequencies may not be practical when the WPT operating frequency increases to the MHz band.

As presented in the previous chapters of this thesis, wireless power transfer has various mechanisms and topologies, each one having its advantages and

drawbacks depending on the application. After the selection of a WPT topology, the design and implementation of coupling elements are complex steps, usually requiring careful considerations and iterative approaches to optimize efficiency and minimize losses in these circuits. However, WPT systems are composed of multiple modules. For instance, a careful and competent coil or antenna implementation may constitute an extremely inefficient WPT system if an inappropriate rectifier topology is chosen.

When designing high-frequency rectifiers, it is necessary to consider the parasitic elements included in the diode's linear model [61], as shown in Figure 4.1. The complete model contains four voltage-independent components (package inductance ($L_p$), beam lead capacitance ($C_b$), package capacitance ($C_p$), and contact resistance ($R_S$)) and two voltage-dependent components (junction resistance ($R_J$) and junction capacitance ($C_J$)) [62]. In MHz rectifier design, a simplified model containing the diode's resistance $R_D$ and a parallel capacitance $C_D$ is generally sufficient [63]. The diode's parasitic elements are usually neglected in lower frequencies, but cause increased adverse effects on rectifiers' behaviour in higher frequencies.

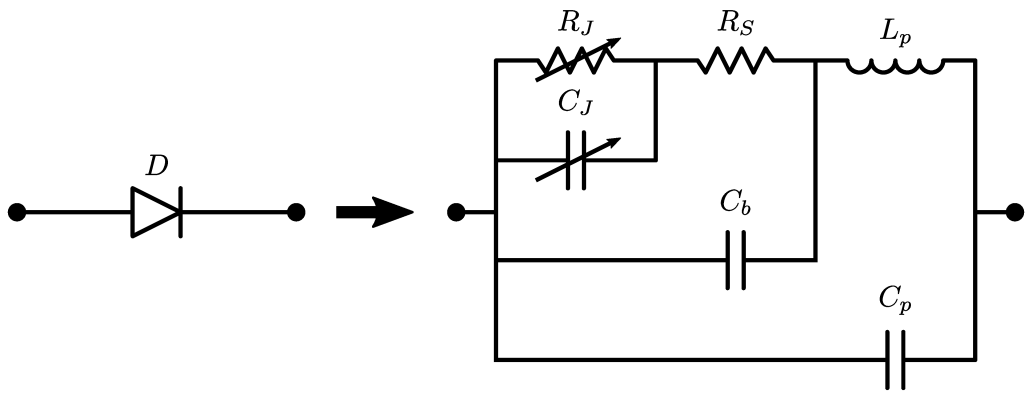


(a)

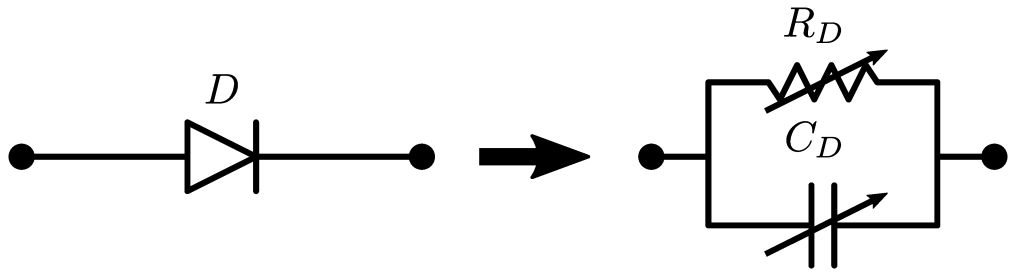


(b)

Figure 4.1: Diode's high-frequency models: (a) complete model, and (b) simplified model

To exemplify, the full-bridge rectifier (depicted in Figure 4.2) is a very popular rectifier topology in WPT. It can be found in applications in frequencies up to hundreds of kHz [18], [20], [64]. However, it presents important problems that prevents its use in MHz frequencies, mainly severe efficiency degradation [64] and inability to analytically predict its input impedance [63].

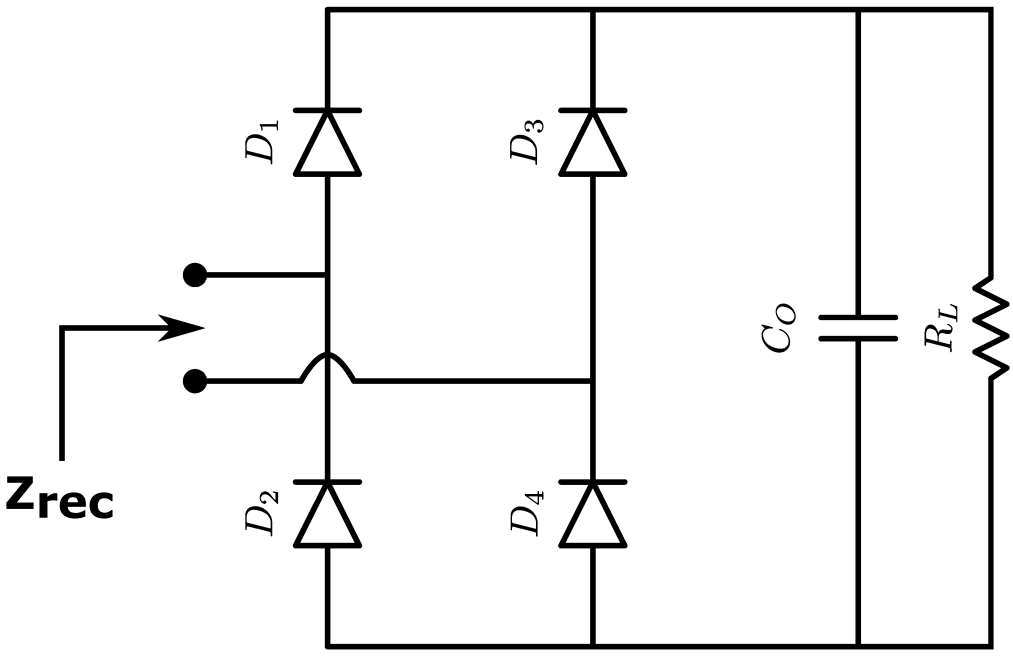


Figure 4.2: Circuit model of full-bridge rectifier

In a low frequency application, in the positive voltage semi-cycle, diodes $D_1$ and $D_4$ are forward biased and conducting, whereas $D_2$ and $D_3$ are reverse bi-

ased and open-circuited, and vice-versa in the negative semi-cycle. Therefore, the input impedance $Z_{rec}$ can be considered purely resistive [65].

Nevertheless, when considering high frequency effects, the diode cannot be considered a perfect open-circuit in reverse bias mode. The diode's parasitic capacitance will provide a current path when the diode is reverse biased, which becomes more prominent as frequencies increase in the MHz range. Consequently, the previous analysis for the full-bridge is not entirely valid anymore, resulting in an input impedance which will have a substantial reactive element, as well as causing an efficiency decrease. This negative effect is often neglected due to the difficulty to mitigate it [63] and some applications of full-bridge rectifier are still made even when its operation is no longer optimal.

### 4.1.1 Class E Rectifiers

In order to diminish the negative effect of diode's parasitic elements, resonant rectifier topologies can be applied, such as the Class E half-wave [66] and full-wave rectifiers [67]. Figure 4.3 displays the circuit diagram for these rectifiers.

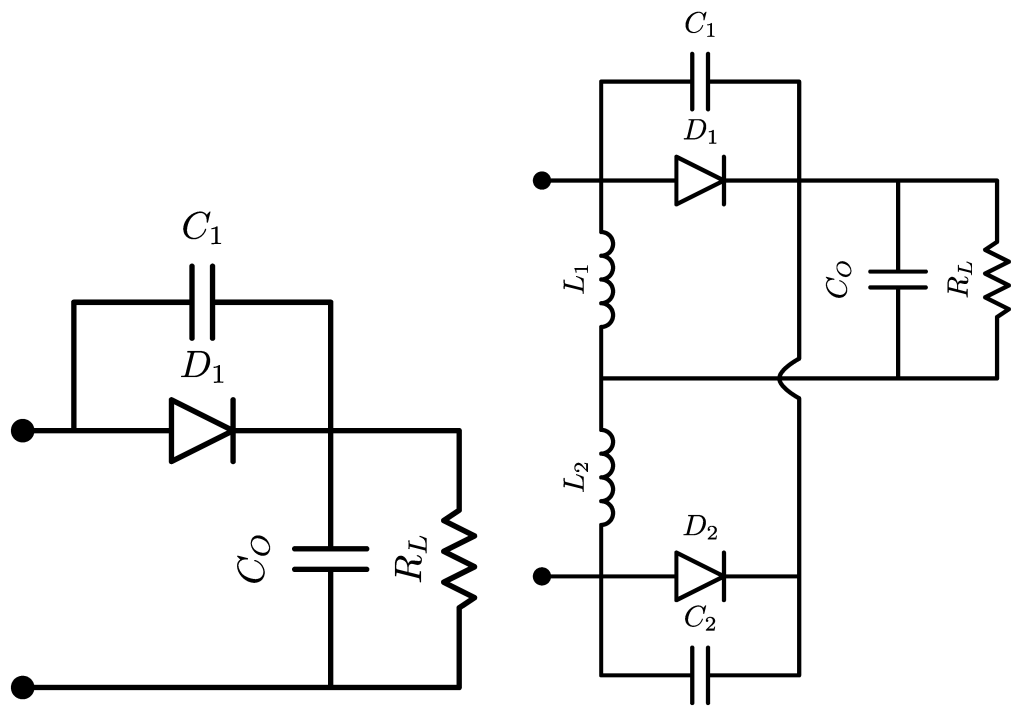


(a) (b)

Figure 4.3: (a) Class E half-wave rectifier and (b) Class E full-wave rectifier circuit diagrams

The half-wave topology is composed of a diode $D_1$ in parallel with a capacitor $C_1$, as well as a filter capacitor $C_O$ in parallel with the load $R_L$. In comparison with its half-wave counterpart, the full-wave requires an additional diode $D_2$ with a parallel capacitor $C_2$, and two filter inductors $L_1$ and $L_2$. These topologies use lumped capacitors in parallel with each diode, which are added to the existent diode's parasitic capacitance. Therefore, the circuit design procedure already includes the effects of the parasitic capacitance and are not adversely affect by it, unlike the full-bridge rectifier explained previously.

As a consequence of its design approach, these types of rectifiers can be very efficient, even in MHz operation [66], [67]. The Class E full-wave rectifier's symmetric circuit provides lower harmonic contents, decreased component stress and losses, as well as reduced output voltage ripple, allowing more efficient application in MHz frequencies [63], [67]. Due to its advantages, it can be considered a good alternative to conventional rectifier in wireless power

transfer, having been implemented in two-coil resonant IPT [63]. Moreover, the input impedance of these rectifiers can be theoretically derived [63], [67], facilitating the design of other modules in WPT systems.

In order to gain more understanding of the Class E full-wave rectifier, it is necessary to provide a brief analysis of its operation. This topology has 4 differents stages during a full cycle, as shown in Figure 4.4. The following description of its behaviour is summarized from [63], [67]. As the inductors $L_1$ and $L_2$ are identical and are ideally large enough to filter all high-frequency components, each of them carries half of the dc output current $I_O$. Assuming that $i_{rec}$ is the sinusoidal input current, in the first stage of conduction, $D_1$ has a current $i_{D_1} = I_O/2 + i_{rec}$ and a current $i_{C_2} = I_O/2 - i_{rec}$ flows through $C_2$. Therefore, the output current $i_{D_1} + i_{C_2} = I_O$ is purely dc due to circuit symmetry. The other conduction modes are analogous, except that either $D_2$ and $C_1$ are conducting, or both capacitors are conducting simultaneously. The values of the capacitors $C_1$ and $C_2$ are the most important design parameters, since they shape the voltage waveforms on the diodes and dictate when they are turned on.

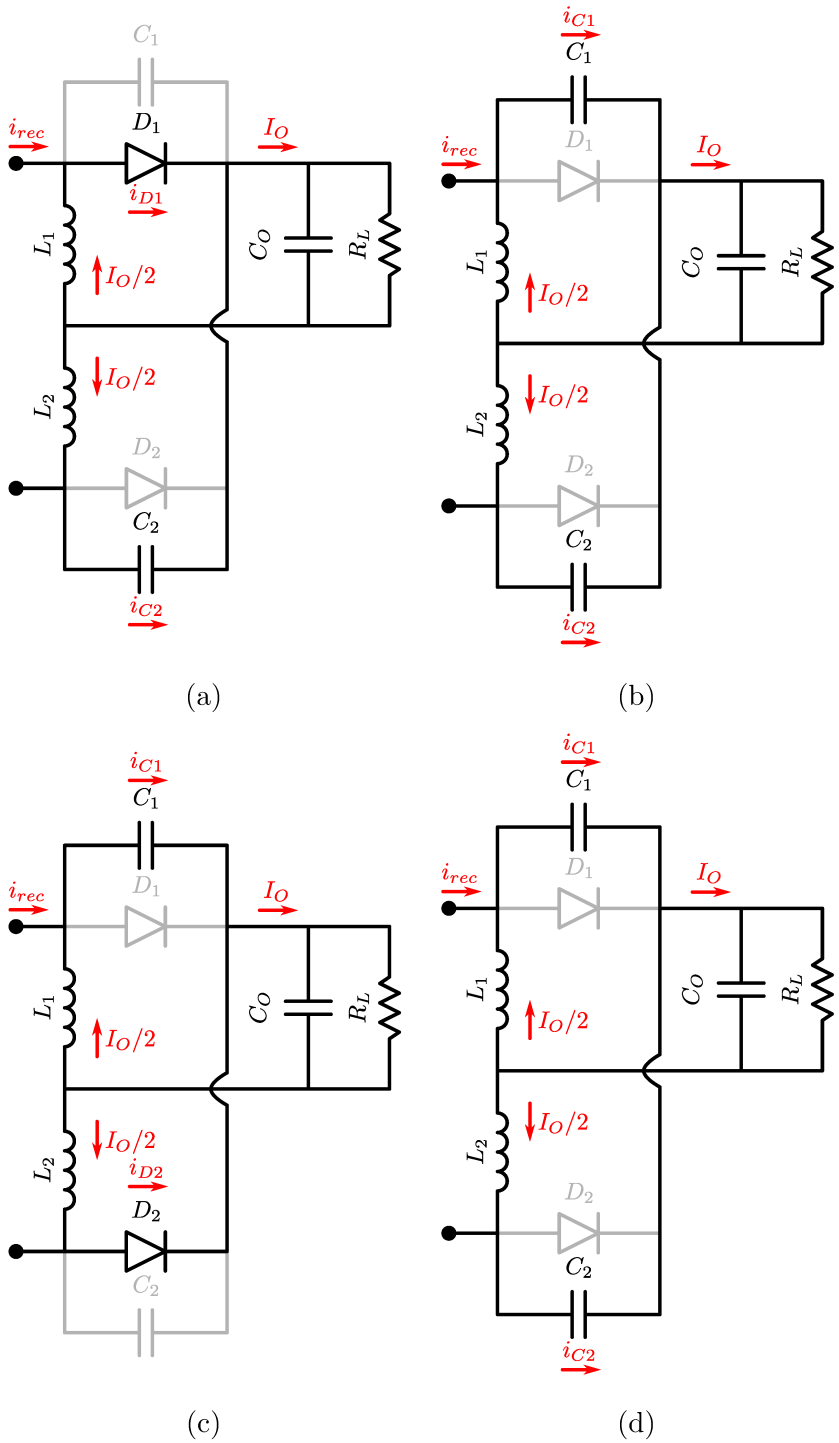


Figure 4.4: Operation of Class E full-wave rectifier. (a) $D_1$ and $C_2$ conducting, (b) $C_1$ and $C_2$ conducting, (c) $C_1$ and $D_2$ conducting, and (d) $C_1$ and $C_2$ conducting. Modified from [63]

Consequently, because of the lack of WPT applications using this highly efficient rectifier, a CPT system using the Class E full-wave rectifier is proposed in the next section.

## 4.2 CPT with Class E Resonant Full-Wave Rectifier

As discussed in Chapters 2 and 3, wireless power transfer circuits that operate in resonant mode are usually more efficient. For this reason, as shown in the block diagram of a general capacitive power transfer system in Figure 4.5, compensation circuits are necessary to provide resonant behaviour and allow more efficient power transfer from transmitter to receiver.

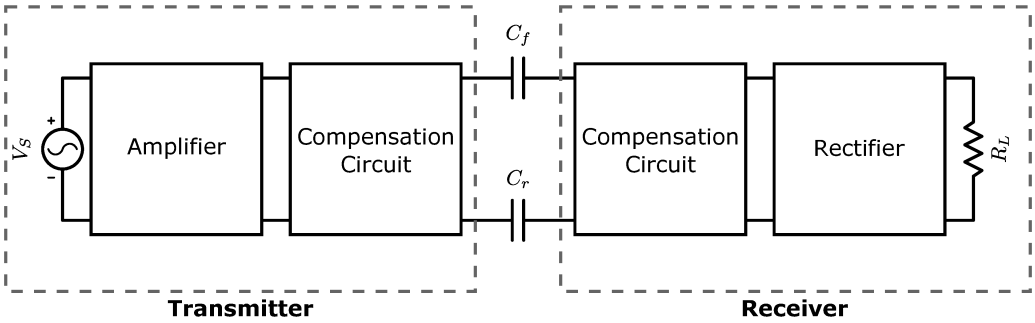


Figure 4.5: Block diagram of a general capacitive power transfer system

Since the forward and return coupling capacitors ($C_f$ and $C_r$) can be small, their large capacitive reactances need to be cancelled by compensation or tuning circuits in the transmitter and/or receiver [19], [65] using, for example, the procedure presented in Chapter 2. However, when designing the complete system, the rectifier may also have a reactive input impedance component, especially in high frequency systems. Consequently, the design of compensation circuits in CPT requires a system-level approach by also considering the effects of the rectifier. The amplifier may also be included in the analysis, but it is not within the scope of this thesis.

Given the advantages of the Class E full-wave rectifier presented in the previous section, an application of this rectifier topology with a CPT system

is proposed [33], along with compensation circuits on transmitter and receiver sides. Figure 4.6 displays the proposed circuit.

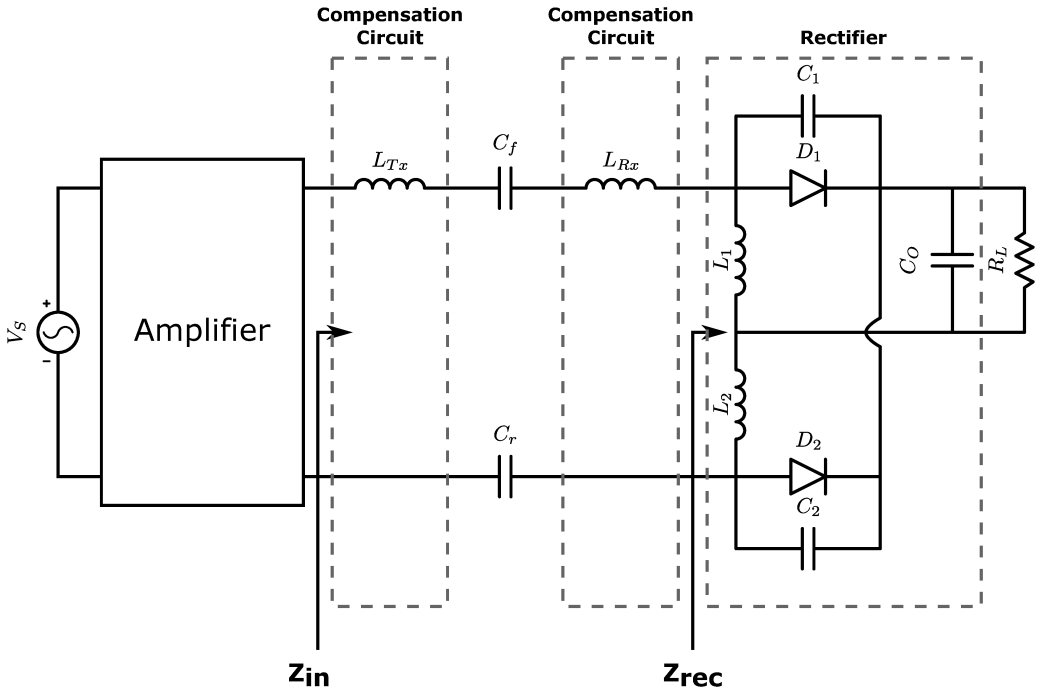


Figure 4.6: Circuit of the proposed CPT system, including a Class E full-wave rectifier and compensation circuits

### 4.2.1 Compensation Circuit Design

In order to design the compensation inductors ($L_{Tx}$ and $L_{Rx}$) for the proposed CPT system, it is necessary to find the input impedance $Z_{in}$ of the circuit. By knowing the input impedance of the Class E full-wave rectifier ($Z_{rec}$) given by [63], $Z_{in}$ is:

$$Z_{in} = j\omega L_{Tx} + \frac{1}{j\omega C_f} + j\omega L_{Rx} + \frac{1}{j\omega C_r} + Z_{rec} \tag{4.1}$$

From a practical perspective, it is generally more beneficial when the series compensation inductor in the transmitter ($L_{Tx}$) is applied to cancel the reactances from the coupling plates $C_f$ and $C_r$ [19]. Therefore, at the frequency of resonance $\omega_0$:

$$L_{Tx} = \frac{1}{{\omega_0}^2}\left(\frac{1}{C_f} + \frac{1}{C_r}\right). \tag{4.2}$$

Thus, the receiver tuning inductor ($L_{Rx}$) can be used to cancel the imaginary part of the impedance $Z_{rec}$. For the particular case of the Class E full-wave rectifier, its input impedance is negative [63], resulting in:

$$L_{Rx} = \frac{-Im(Z_{rec})}{\omega_0}. \tag{4.3}$$

Equations (4.2) and (4.3) provide the necessary steps for designing compensation inductors, which are used to cancel the unwanted capacitive reactances in the system and to provide resonance at $\omega_0$. The values determined for the compensation inductors $L_{Tx}$ and $L_{Rx}$ are optimized to a particular value of coupling capacitors ($C_f$ and $C_r$) and load resistance ($R_L$).

### 4.2.2 Experimental Setup

The experimental setup is shown in Figure 4.7, corresponding to implementation of the system presented in Figure 4.6 with parameters listed in Table 4.1.

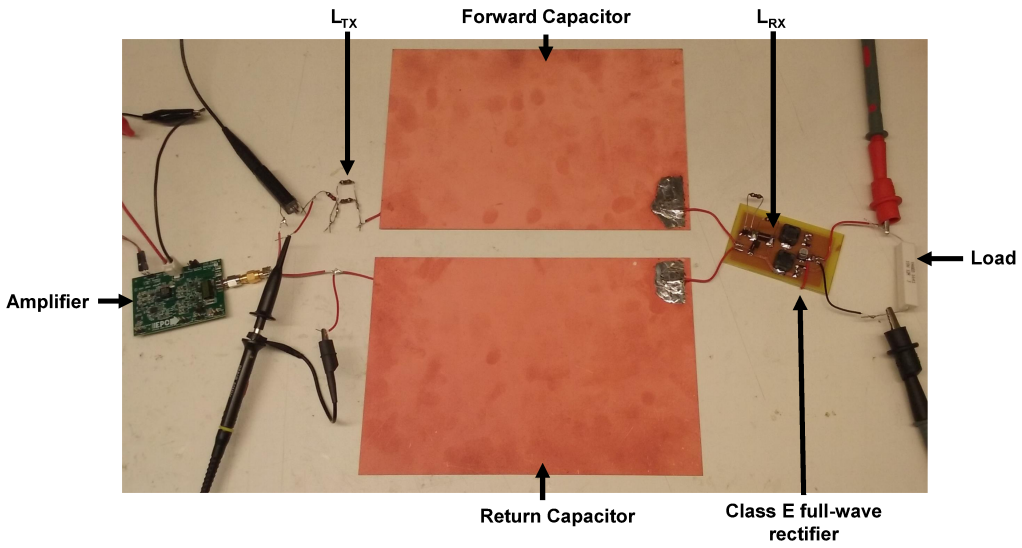


Figure 4.7: Experimental setup for measurement of proposed capacitive power transfer system with inductively compensated Class E full-wave rectifier

Table 4.1: Component values used to evaluate CPT system with Class E full-wave rectifier

| | |
|---|---|
| $L_{Tx}$ | 270 nH |
| $L_{Rx}$ | 491 nH |
| $C_f = C_r$ | 4.068 nF |
| $L_1 = L_2$ | 39 $\mu$H |
| $C_1 = C_2$ | 940 pF + 100 pF |
| $C_O$ | 47 $\mu$F + 100 nF |
| $f_0$ | 6.78 MHz |

The CPT system is designed for operation at the AirFuel standard frequency of 6.78 MHz. The power is provided by an EPC9507 Class D amplifier, which is set to provide a constant voltage of 5.8 $V_{rms}$ for all the tested scenarios. The forward ($C_f$) and return capacitors ($C_r$) are constructed using dimensions of 22.86 cm x 15.24 cm, with a spacing of 0.79 mm, corresponding to the metallic sides of an FR4 substrate. The actual capacitance values of $C_f$ and $C_r$ are measured with a Rohde & Schwarz ZVL13 VNA.

The rectifier was designed following standard procedures described in [63], [67]. Instead of the conventional diode duty cyle of 0.5, a value of 0.37 was chosen to provide an increased voltage transfer ratio. DFLS240L Schottky diodes are used in the rectifier circuit due to their significantly low forward voltage drop, with its parasitic capacitance being approximately 100 pF. The compensation inductors $L_{Tx}$ and $L_{Rx}$ were designed based on Equations (4.2) and (4.3) for an optimal load of 12 $\Omega$.

Input power and phase measurements are made by measuring RMS voltages and currents with an Agilent DSO-X 3034A oscilloscope and a Tektronix CT-2 current probe. Output DC power measurements at the load are made with an Agilent U1253B multimeter. Efficiency is calculated by the ratio of output DC power over the input real power, with losses in the amplifier not being considered.

### 4.2.3 Results

Figure 4.8 displays the simulated efficiencies of the designed CPT system using a Class E full-wave rectifier compared to the same system using a conventional full-bridge rectifier instead. In the case of the full-bridge circuit, the compensation inductor $L_{Rx}$ was not applied because this is the common approach for this rectifier, since its input impedance cannot be derived analytically [63], which prevents the straightforward use of compensation circuits. From this plot, it can be seen that the designed circuit using the proposed approach is generally 3 % to 5 % more efficient than the conventional approach, except for loads much larger than the 12 Ω nominal load, which cause efficiency degradation on Class E rectifiers [67].

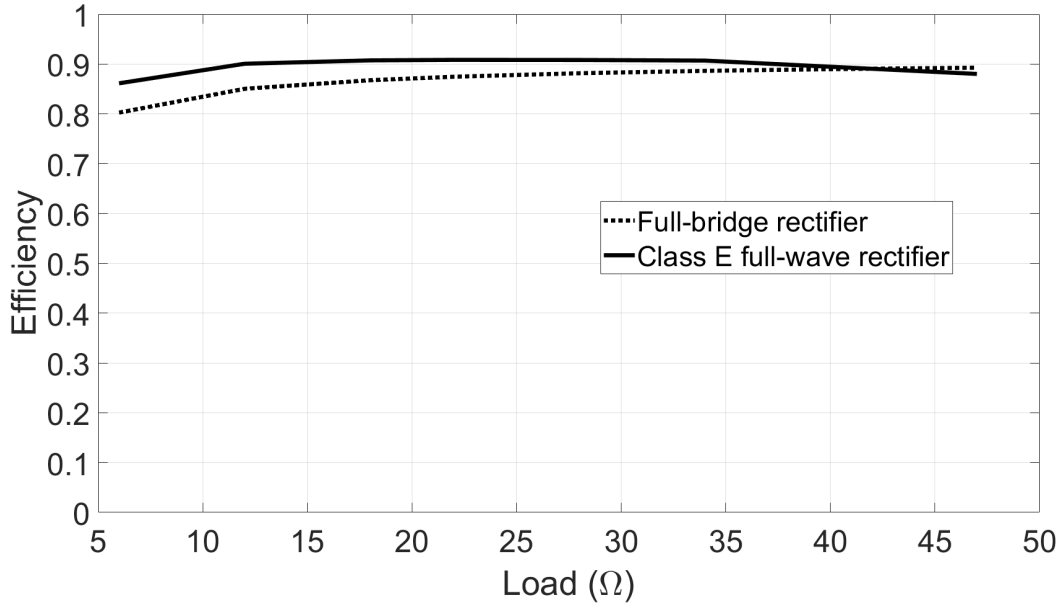


Figure 4.8: Simulated efficiency of CPT systems with full-bridge and Class E full-wave rectifiers

The measured efficiency and output power for the proposed CPT system are shown in Figure 4.9, displaying good agreement with simulated values. An efficiency of 89.98 % was measured for the nominal load of 12 Ω, corresponding to an input power of 2.431 W and an output power of 2.187 W. A peak efficiency of 92.88 % was obtained for the 18 Ω load due to proximity to the nominal load, but having decreased losses as the output power was lower.

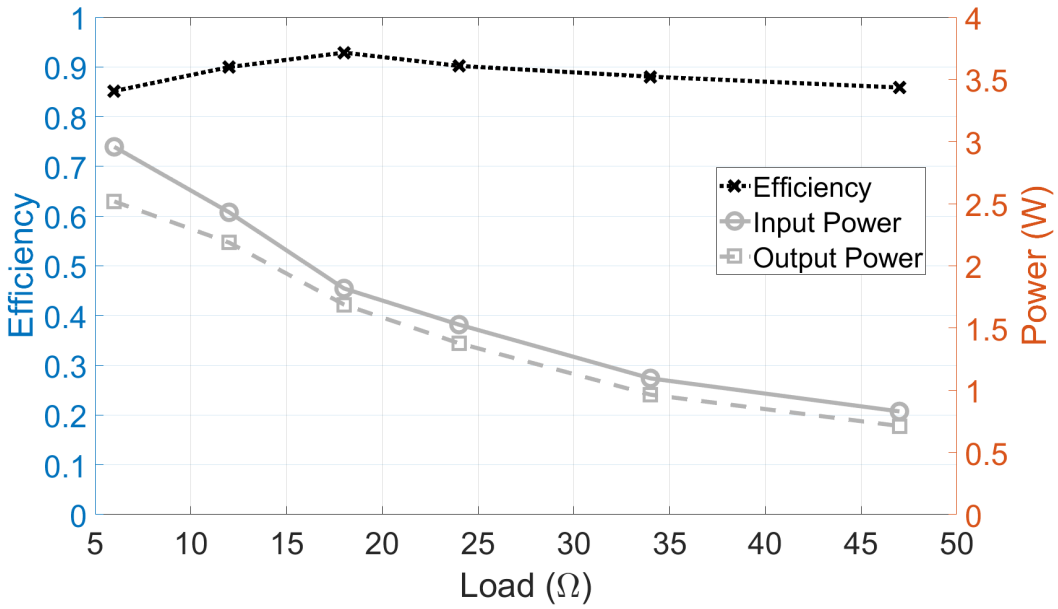


Figure 4.9: Measured efficiency and output power for CPT system with Class E full-wave rectifer

Finally, Figure 4.10 depicts the measured and simulated phase of $Z_{in}$. For a load of 12 Ω, the proposed compensation circuits are able to properly cancel the reactances introduced by the coupling capacitances and rectifier. Therefore, voltage and current are almost in phase for this case. Since $L_{Tx}$ and $L_{Rx}$ are designed for the particular load of 12 Ω and coupling capacitors of 4.068 nF, it is necessary to work close to this exact point of operation for best performance.

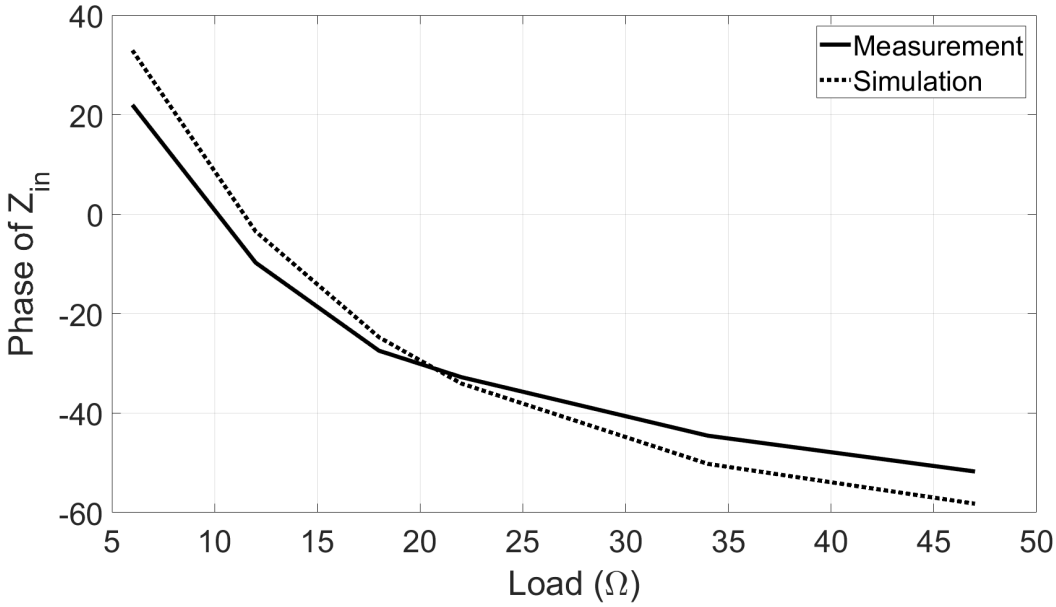


Figure 4.10: Measured and simulated phase of $Z_{in}$

## 4.3 Chapter Summary

This chapter analyzed the use of rectifiers to perform ac to dc power conversion in a capacitive power transfer system operating at the frequency of 6.78 MHz.

Initially, it was established that regular rectifiers, such as the full-bridge configuration, show efficiency degradation in MHz frequencies due to the diode's parasitic capacitance. Therefore, the Class E rectifiers were studied because of their high efficiency in these frequencies, as well as the ability to analytically model their input impedance.

Then, an application of the Class E full-wave rectifier topology in a capacitive power transfer system is proposed. Equations are derived to design the inductors required to compensate for the coupling capacitances and the rectifier's reactive impedance. Results show that the proposed system is up to 5 % more efficient than the conventional application of a full-bridge rectifier in the same scenario. It is shown that the reactive impedances are properly cancelled and the highest efficiencies are obtained for loads close to the nominal design value of 12 Ω.

# Chapter 5

# Conclusion

This thesis presented studies in near-field wireless power transfer systems, as well as coherent circuit module design with respect to the particularities of a WPT mechanism.

## 5.1 Summary

The most common near-field WPT topologies were analyzed based on $|S_{21}|_{max}$ and their corresponding frequency $f_0$ or $f_{max}$. The non-resonant inductive topology may be simple to deploy, but exhibits high efficiency degradation as $k$ decreases. Conversely, resonant inductive configurations are more robust regarding $k$, leading to increased distance range and possible freedom of receiver device placement. Additionally, four-coil inductive topology may lead to slight efficiency degradation in exchange for a great extension in WPT distance. Finally, resonant capacitive systems are more resistant regarding changes in distance than IPT.

The minimized loading effect introduced in the four-coil IPT topology, along with construction characteristics of high Q open-ended resonators, inspired the implementation of a novel WPT topology using capacitively coupled open-ended helical resonators. A peak $|S_{21}|$ of -2.32 dB was measured at 6.01 MHz, while the corresponding simulation resulted in a peak $|S_{21}|$ of -1.42 dB at 6.88 MHz, and lumped circuit calculations resulted in a peak of -0.2877 dB at 6.86 MHz. The effect of Tx-Rx distance, misalignment, and resonator-plate spacing were also investigated by measurements and simulations. The

proposed WPT topology has high tolerance to misalignment and distance, without presenting significant shifts in resonant frequency. While the same trends were identified both in measurements and simulations, reasons for discrepancies between them were listed, mainly regarding simplifications in simulation procedures and manual construction inaccuracies. Considering safety regulations in Canada, it was found that the current configuration presents a significant electric field strength that has to be addressed in future research.

Finally, an application of the efficient class E full-wave rectifier in a CPT system is proposed. At an output power level of 2.187 W, an overall system efficiency of 89.98 % was achieved. Moreover, the reactance introduced by the capacitive plates was corrected by providing a design procedure for the compensation circuits, which also addressed the particular characteristics of the rectifier.

## 5.2 Future Work

Based on the results of this thesis, the suggestion for future research includes:

- Study of miniaturization techniques to reduce the size of resonators, leading to a more compact system suitable for portable electronic devices.
- Analysis of shielding techniques to prevent unsafe field strengths when operating in higher power levels.
- Since the magnetic field strength is well below the regulated limits, magnetic field coupling can be also applied. For the proposed structure, the Tx to Rx coupling mechanism relies solely on capacitive coupling. However, using a combination of capacitive and inductive coupling can be useful to diminish possible unsafe electric field intensities, while still operating at higher power levels.
- Instead of using transformers to prevent spurious coupling to measurement equipment and nearby materials, there are other approaches available in the literature. For example, it is possible to study the effectiveness

of ferrite loaded cables or absorbing materials to provided improved isolation. If successful, these methods could make the measurement results closer to simulation and calculated values.

- Finally, when considering the use of the capacitively coupled OEHR system in higher power systems, it is necessary to integrate it with an efficient rectifer. An application of Class E rectifiers can be made specifically to the proposed WPT system, requiring appropriate design of compensation circuits.

# References


[1] M. Treffers, "Wireless Power Market in 2017," *Wireless Power Consortium*, 2018. 1

[2] J. Jonnes, *Empires Of Light: Edison, Tesla, Westinghouse, And The Race To Electrify The World*. Random House Trade Paperbacks, 2004. 2

[3] W. J. Baker, *A History of the Marconi Company*. Methuen & Co Ltd, 1970. 2

[4] W. C. Brown, "The History of Power Transmission by Radio Waves," *IEEE Transactions on Microwave Theory and Techniques*, vol. 32, no. 9, 1230-1242, Sep. 1984. 2

[5] S. Y. R. Hui, W. Zhong, and C. K. Lee, "A Critical Review of Recent Progress in Mid-Range Wireless Power Transfer," *IEEE Transactions on Power Electronics*, vol. 29, no. 9, pp. 4500–4511, Sep. 2014. 2, 5, 18

[6] R. M. Dickinson, "Evaluation of a microwave high-power reception-conversion array for wireless power transmission," Nov. 1975. 3

[7] S. Y. Hui, "Planar Wireless Charging Technology for Portable Electronic Products and Qi," *Proceedings of the IEEE*, vol. 101, no. 6, pp. 1290–1301, Jun. 2013. 3, 6

[8] F. Carobolante, P. Menegoli, F. A. Marino, and N. S. Jeong, "A Novel Charger Architecture for Resonant Wireless Power Transfer," *IEEE Journal of Emerging and Selected Topics in Power Electronics*, vol. 6, no. 2, pp. 571–580, Feb. 2018. 3, 6

[9] D. J. Graham, J. A. Neasham, and B. S. Sharif, "Investigation of Methods for Data Communication and Power Delivery Through Metals," *IEEE Transactions on Industrial Electronics*, vol. 58, no. 10, pp. 4972–4980, Oct. 2011. 4

[10] A. S. Rekhi, B. T. Khuri-Yakub, and A. Arbabian, "Wireless Power Transfer to Millimeter-Sized Nodes Using Airborne Ultrasound," *IEEE Transactions on Ultrasonics, Ferroelectrics, and Frequency Control*, vol. 64, no. 10, pp. 1526–1541, Oct. 2017. 4

[11] V. F.-G. Tseng, S. S. Bedair, and N. Lazarus, "Acoustic Power Transfer and Communication With a Wireless Sensor Embedded Within Metal," *IEEE Sensors Journal*, vol. 18, no. 13, pp. 5550–5558, Jul. 2018. 4

[12] C. A. Balanis, *Antenna Theory: Analysis and Design*, 4th ed. 2016. 5, 6

[13] W. L. Stutzman and G. A. Thiele, *Antenna Theory and Design*, 3rd ed. 2013. 5, 6

[14] H. J. Visser, *Antenna Theory and Applications*, 1st ed. 2012. 5–7

[15] B. L. Cannon, J. F. Hoburg, D. D. Stancil, and S. C. Goldstein, "Magnetic Resonant Coupling As a Potential Means for Wireless Power Transfer to Multiple Small Receivers," *IEEE Transactions on Power Electronics*, vol. 24, no. 7, pp. 1819–1825, Jul. 2009. 5, 44

[16] M. Kiani, U.-M. Jow, and M. Ghovanloo, "Design and Optimization of a 3-Coil Inductive Link for Efficient Wireless Power Transmission," *IEEE Transactions on Biomedical Circuits and Systems*, vol. 5, no. 6, pp. 579–591, Dec. 2011. 5

[17] W. Zhong, C. K. Lee, and S. Y. R. Hui, "General Analysis on the Use of Tesla's Resonators in Domino Forms for Wireless Power Transfer," *IEEE Transactions on Industrial Electronics*, vol. 60, no. 1, pp. 261–270, Jan. 2013. 5

[18] F. Lu, H. Zhang, and C. Mi, "A Review on the Recent Development of Capacitive Wireless Power Transfer Technology," *Energies*, vol. 10, no. 11, 2017. 6, 34, 75

[19] C. Liu, A. P. Hu, G. A. Covic, and N.-K. C. Nair, "Comparative Study of CCPT Systems With Two Different Inductor Tuning Positions," *IEEE Transactions on Power Electronics*, vol. 27, no. 1, pp. 294–306, Jan. 2012. 6, 34, 80, 81

[20] H. Zhang, F. Lu, H. Hofmann, W. Liu, and C. C. Mi, "Six-Plate Capacitive Coupler to Reduce Electric Field Emission in Large Air-Gap Capacitive Power Transfer," *IEEE Transactions on Power Electronics*, vol. 33, no. 1, pp. 665–675, Jan. 2018. 6, 75

[21] N. Shinohara, "Power without wires," *IEEE Microwave Magazine*, vol. 12, no. 7, S64–S73, Dec. 2011. 6

[22] N. Shinohara and H. Matsumoto, "Experimental study of large rectenna array for microwave energy transmission," *IEEE Transactions on Microwave Theory and Techniques*, vol. 46, no. 3, pp. 261–268, Mar. 1998. 6

[23] N. Shinohara and N. Kamiyoshikawa, "Study of flat beam in near-field for beam-type wireless power transfer via microwaves," in *2017 11th European Conference on Antennas and Propagation (EUCAP)*, Paris, France, Mar. 2017. 6

[24] A. P. Sample, D. J. Yeager, P. S. Powledge, A. V. Mamishev, and J. R. Smith, "Design of an RFID-Based Battery-Free Programmable Sensing Platform," *IEEE Transactions on Instrumentation and Measurement*, vol. 57, no. 11, pp. 2608–2615, Nov. 2008. 7

[25] R. Mirzavand, M. M. Honari, B. Laribi, B. Khorshidi, M. Sadrzadeh, and P. Mousavi, "An Unpowered Sensor Node for Real-Time Water Quality Assessment (Humic Acid Detection)," *Electronics*, vol. 7, no. 10, p. 231, Oct. 2018. 7

[26] J. Fakidis, S. Videv, S. Kucera, H. Claussen, and H. Haas, "Indoor Optical Wireless Power Transfer to Small Cells at Nighttime," *Journal of Lightwave Technology*, vol. 34, no. 13, pp. 3236–3258, Jul. 2016. 7

[27] A. P. Sample, D. T. Meyer, and J. R. Smith, "Analysis, Experimental Results, and Range Adaptation of Magnetically Coupled Resonators for Wireless Power Transfer," *IEEE Transactions on Industrial Electronics*, vol. 58, no. 2, pp. 544–554, Mar. 2011. 11, 13, 14, 23, 25, 27, 43

[28] H. Saghlatoon, R. Mirzavand, M. M. Honari, and P. Mousavi, "Investigation on Passive Booster for Improving Magnetic Coupling of Metal Mounted Proximity Range HF RFIDs," *IEEE Transactions on Microwave Theory and Techniques*, vol. 65, no. 9, pp. 3401–3408, Sep. 2017. 11, 57

[29] A. Kurs, A. Karalis, R. Moffatt, J. D. Joannopoulos, P. Fisher, and M. Soljačić, "Wireless Power Transfer via Strongly Coupled Magnetic Resonances," *Science*, vol. 317, no. 5834, 83-86, Jul. 2007. 18, 41, 42, 44, 49

[30] Y. H. Sohn, B. H. Choi, E. S. Lee, G. C. Lim, G.-H. Cho, and C. T. Rim, "General Unified Analyses of Two-Capacitor Inductive Power Transfer Systems: Equivalence of Current-Source SS and SP Compensations," *IEEE Transactions on Power Electronics*, vol. 30, no. 11, pp. 6030–6045, Nov. 2015. 19, 20

[31] C. M. de Miranda and S. F. Pichorim, "A Self-Resonant Two-Coil Wireless Power Transfer System Using Open Bifilar Coils," *IEEE Transactions on Circuits and Systems II: Express Briefs*, vol. 64, no. 6, pp. 615–619, Jun. 2017. 20, 42

[32] Z. Dang, "Magnetic Resonance Coupled Wireless Power Transfer Systems," Master of Science Thesis, University of Alabama, 2013. 20, 22, 27

[33] F. C. Domingos, S. V. de C. de Freitas, and P. Mousavi, "Capacitive Power Transfer based on Compensation Circuit for Class E Resonant Full-Wave Rectifier," in *2018 IEEE MTT-S Wireless Power Transfer Conference (WPTC)*, Montreal, QC, Canada, Jun. 2018. 34, 81

[34] R. D. Fernandes, J. N. Matos, and N. B. Carvalho, "Resonant Electrical Coupling: Circuit Model and First Experimental Results," *IEEE Transactions on Microwave Theory and Techniques*, vol. 63, no. 9, pp. 2983–2990, Aug. 2015. 34

[35] L. Huang, A. P. Hu, A. K. Swain, and Y. Su, "Z-Impedance Compensation for Wireless Power Transfer Based on Electric Field," *IEEE Transactions on Power Electronics*, vol. 31, no. 11, pp. 7556–7563, Nov. 2016. 35, 40

[36] AVX Corporation, "RF/Microwave MLC's, SQ Series Ultra Low ESR MLC," *Component Datasheet*, 2017. 42

[37] C. W. Van Neste *et al.*, "Single-contact transmission for the quasi-wireless delivery of power over large surfaces," *Wireless Power Transfer, Cambridge University Press*, vol. 1, no. 2, pp. 75–82, Sep. 2014. 43–45

[38] C. M. de Miranda and S. F. Pichorim, "Self-resonant frequencies, standing waves, and impedance behavior of air-core helical solenoidal coil," in *2015 International Conference on Electromagnetics in Advanced Applications (ICEAA)*, Turin, Italy, Sep. 2015. 43, 51

[39] ——, "Self-resonant frequencies of air-core single-layer solenoid coils calculated by a simple method," *Electrical Engineering*, vol. 97, no. 1, pp. 57–64, Mar. 2015. 43, 44

[40] B. Breitkreutz and H. Henke, "Calculation of Self-Resonant Spiral Coils for Wireless Power Transfer Systems With a Transmission Line Approach," *IEEE Transactions on Magnetics*, vol. 49, no. 9, pp. 5035–5042, Sep. 2013. 43

[41] J. Pierce, "Theory of the Beam-Type Traveling-Wave Tube," *Proceedings of the IRE*, vol. 35, no. 2, pp. 111–123, Feb. 1947. 44

[42] S. Sensiper, "Electromagnetic wave propagation on helical conductors," Doctorate (D. Sc) Thesis, Massachusetts Institute of Technology, 1951. 44

[43] K. L. Corum and J. F. Corum, "RF coils, helical resonators and voltage magnification by coherent spatial modes," in *5th TELSIKS*, Nis, Yugoslavia, Sep. 2001. 44

[44] B. McGuyer, "Paul Drude's Prediction of Nonreciprocal Mutual Inductance for Tesla Transformers," *Public Library of Science (PLOS One)*, vol. 9, no. 12, Dec. 2014. 44, 57

[45] S. V. de C. de Freitas, A. Maunder, F. C. Domingos, and P. Mousavi, "Method and system for wireless and single-conductor power and data transmission," in *2016 IEEE Wireless Power Transfer Conference (WPTC)*, Aveiro, Portugal, May 2016. 44, 46

[46] S. V. de C. de Freitas, F. C. Domingos, R. Mirzanvand, A. Maunder, P. Naseri, and P. Mousavi, "A Novel Method for Data and Power Transmission Through Metallic Structures," *IEEE Transactions on Industrial Electronics*, vol. 64, no. 5, 4027-4036, May 2017. 44, 46

[47] F. C. Domingos, S. V. de C. de Freitas, and P. Mousavi, "Overview of Single Conductor Power Transfer with Open-Ended Helical Resonators," in *18th International Symposium on Antenna Technology and Applied Electromagnetics (ANTEM)*, Waterloo, ON, Canada, Aug. 2018. 44, 45

[48] T. Zarifi, K. Moez, and P. Mousavi, "Impedance matching network for ground eliminated open-ended resonant coil structure in distributed wireless power transmission systems," *IET Science, Measurement & Technology*, vol. 11, no. 7, pp. 856–860, Oct. 2017. 45, 55

[49] S. V. de C. de Freitas, F. C. Domingos, R. Mirzavand, and P. Mousavi, "Contactless Power Transfer Using Capacitive Resonant Single-Conductor Structure," in *2018 IEEE MTT-S Wireless Power Transfer Conference (WPTC)*, Montreal, QC, Canada, Jun. 2018. 48

[50] C. W. Van Neste *et al.*, "Quarter wavelength resonators for use in wireless capacitive power transfer," in *2017 IEEE PELS Workshop on Emerging Technologies: Wireless Power Transfer (WoW)*, Chongqing, China, May 2017. 50

[51] R. A. Moffatt, "Wireless transfer of electric power," Bachelor of Science in Physics Thesis, Massachusetts Institute of Technology, 2009. 55

[52] O. Staub, J. Zürcher, and A. Skrivervik, "Some considerations on the correct measurement of the gain and bandwidth of electrically small antennas," *Microwave and Optical Technology Letters*, vol. 17, no. 3, pp. 156–160, Feb. 1998. 56

[53] M. Rao and K. Sarabandi, "A Tunable, High-Gain, Very Low-Profile Composite Monopole Antenna for Low-Frequency Applications," *IEEE Transactions on Antennas and Propagation*, vol. 66, no. 7, pp. 3286–3294, Jul. 2018. 56

[54] J. T. Bernhard, J. J. Adams, M. D. Anderson, and J. M. Martin, "Measuring electrically small antennas: Details and implications," in *2009 IEEE International Workshop on Antenna Technology*, Santa Monica, CA, USA, Mar. 2009. 56

[55] L. F. Shatz and C. W. Christensen, "Numerical Inductance Calculations Based on First Principles," *Public Library of Science (PLOS One)*, vol. 9, no. 11, Nov. 2014. 56

[56] H. A. Wheeler, "Simple Inductance Formulas for Radio Coils," *Proceedings of the Institute of Radio Engineers*, vol. 16, no. 10, pp. 1398–1400, Oct. 1928. 56

[57] H. Nishiyama and M. Nakamura, "Form and capacitance of parallel-plate capacitors," *IEEE Transactions on Components, Packaging, and Manufacturing Technology: Part A*, vol. 17, no. 3, pp. 477–484, Sep. 1994. 57

[58] D. M. Pozar, *Microwave Engineering*, 4th ed. 2012. 58

[59] R. G. Medhurst, "H.F. Resistance and Self-capacitance of Single-Layer Solenoids," *Wireless Engineer*, vol. 24, no. 9, pp. 35–43,80–92, Feb. 1947. 58

[60] Health Canada, "Limits of Human Exposure to Radiofrequency Electromagnetic Energy in the Frequency Range from 3 kHz to 300 GHz," 2015. 70

[61] U. L. Rohde and M. Rudolph, *RF/microwave circuit design for wireless applications*, 2nd ed. 2013. 74

[62] J. Hansen and K. Chang, "Diode modeling for rectenna design," in *2011 IEEE International Symposium on Antennas and Propagation (APSURSI)*, Spokane, WA, USA, Jul. 2011. 74

[63] M. Liu, M. Fu, and C. Ma, "Low-Harmonic-Contents and High-Efficiency Class E Full-Wave Current-Driven Rectifier for Megahertz Wireless Power Transfer Systems," *IEEE Transactions on Power Electronics*, vol. 32, no. 2, pp. 1198–1209, Feb. 2017. 74–79, 81–84

[64] M. Fu, Z. Tang, M. Liu, C. Ma, and X. Zhu, "Full-bridge rectifier input reactance compensation in Megahertz wireless power transfer systems," in *2015 IEEE PELS Workshop on Emerging Technologies: Wireless Power (2015 WoW)*, Daejeon, South Korea, Jun. 2015. 75

[65] M. P. Theodoridis, "Effective Capacitive Power Transfer," *IEEE Transactions on Power Electronics*, vol. 27, no. 12, pp. 4906–4913, Dec. 2012. 76, 80

[66] M. K. Kazimierczuk, "Analysis of class E zero-voltage-switching rectifier," *IEEE Transactions on Circuits and Systems*, vol. 37, no. 6, pp. 747–755, Jun. 1990. 76, 77

[67] A. Reatti, M. Kazimierczuk, and R. Redl, "Class E full-wave low dv/dt rectifier," *IEEE Transactions on Circuits and Systems I: Fundamental Theory and Applications*, vol. 40, no. 2, pp. 73–85, Feb. 1993. 76–78, 83, 84